Ultrafast Dynamics of Metallo-dielectric Core-shell Particles

Ultrafast Dynamics of Metallo-dielectric Core-shell Particles X. Shan

Ph. D Thesis Utrecht University, March 2008
ISBN: 978-90-393-4771-3

Ultrafast Dynamics of Metallo-dielectric Core-shell Particles

Ultrasnelle Dynamica van Metallo-diëlektrische Kern-schil-deeltjes

(met een samenvatting in het Nederlands)

Proefschrift

ter verkrijging van de graad van doctor aan de Universiteit Utrecht op gezag van de rector magnificus, prof.dr. J.C. Stoof, ingevolge het besluit van het college voor promoties in het openbaar te verdedigen op dinsdag 25 maart 2008 des ochtends te 10.30 uur

door

Xinyan Shan

geboren op 14 mei 1979 te Taian, Shandong, China

Ultrafast Dynamics of Metallo-dielectric Core-shell Particles X. Shan

Promotor: Prof. dr. J. I. Dijkhuis

Contents

Chapter 1

Introduction

1.1 Metallo-dielectric materials

The interaction between light and matter is an important issue in physics. The propagation of light in dielectric materials is a classical topic treated in textbooks [1], and is governed by the refractive index. Reflection, absorption, and transmission of a smooth surface can be described by Fresnel formulas with complex index of refraction. In a metal, free electrons yield completely different optical responses than that of dielectric materials. The optically induced coherent oscillating charge distribution at the metal surface gives rise to strong surface electromagnetic fields, known as surface plasmons. Historically[2], plasma waves were predicted theoretically by Bohm and Pines [3] in the fifties as the electromagnetic eigen modes in a homogeneous metal. Subsequently, Melnyk and Harrison [4] predicted the possibility of resonant excitation of plasmons in thin metal films by electromagnetic waves. Such resonances were observed experimentally for the first time in 1970 [5].

In the last decades, the rapid development of nanotechnology allowed people to fabricate materials with sizes smaller than or comparable to the light wavelength, which opened a new area for studies of light-matter interaction. For example, by arranging a periodically modulated index of refraction in dielectrics at the scale of the wavelength of light, one creates, so-called photonic crystals, with unusual optical properties [6][7]. Here, multiple in-

terference of light on a periodic lattice leads to a photonic stop band and anomalous dispersion [8]. Photonic crystals can be found in nature, such as the Morpho butterfly's wings [9][10]. Vlasov and co-workers have succeeded in creating an inverted silicon opal starting from the self-assembly of a colloidal suspension of silica microspheres into an ordered template [11]. The signature of a photonic band gap in the telecom range (1.5 μm) was confirmed by optical spectroscopy in two directions through the silicon lattice. In the research on photonic crystals, metals were avoided because of their inherent ohmic losses. However, metals have large dielectric constants which a potential advantage when one needs a large optical contrast.

By making metal structures with a scale comparably with the wavelength of light, the surface plasmon resonance caused by optical induced charge oscillations can be enhanced and its frequency controlled. Nano-scale metal holes, grooves, and particles have been fabricated. Ebbesen and his co-workers [12] discovered an unexpectedly high optical transmission through a photonic array of sub-wavelength holes in a metal film of 200-nm thickness. In 2002, Lezec and his co-workers discovered a highly directional emission from a single sub-wavelength metal film aperture surrounded by surface corrugations on the scale of the wavelength of light [13], pointing to the formation of electromagnetic surface plasmon resonances. The direction, width, and wavelength at which the beam occurs can be controlled by the geometrical surface parameters of the structure. Further, strong coupling between localized particle plasmons and optical waveguide modes results in the formation of a full one-dimensional photonic band gap in resonant plasmon-waveguide structures [14]. For a metal particle which is much smaller than the wavelength of light, the surface plasmon resonance frequency is size and shape dependent [15][16].

Recently, progress in the synthesis of metallo-dielectric colloids allows one to fabricate core-shell metallo-dielectric particles with a size of the wavelength of visible light [17]. The situation of spherical metallic nanoshells is even more complicated, because it contains two types of surface plasmons: one localized on the internal surface and one localized on the external surface of the shell. Hybridization of plasmon modes was reported in very complex multishell particles composed of a silica core and consecutive shells of gold and silica [18]. The hybridization of the plasmon states is the result of a strong coupling between the inner and outer metal shells and appeared to be very sensitive to the thickness of the separating dielectric layer. The effect provides an efficient

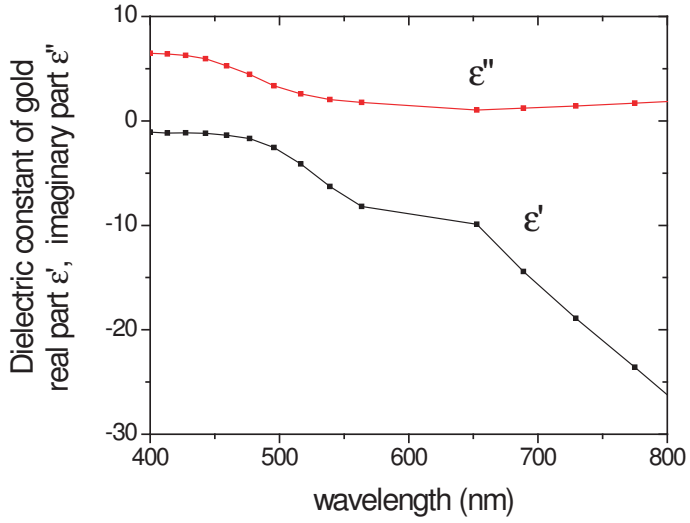

Figure 1.1: Dispersion of the real, ϵ', and the imaginary ϵ'', parts of the dielectric constant of gold.

tool for photonic band gap engineering in metallo-dielectric photonic crystals.

1.2 Surface plasmon in metals

The optical response of a material is characterized by a frequency dependent complex dielectric constant $\epsilon(\omega)$. In a metal, the dielectric constant $\epsilon(\omega)$ is given by [19]

$$\epsilon(\omega) = \epsilon_b(\omega) + i \, \frac{ne^2}{m\omega(\gamma_0 - i\omega)} \, , \tag{1.1}$$

with γ_0 the damping constant, n the number of free electrons per unit volume, and $\epsilon_b(\omega)$ contributions of all other dipoles.

For higher frequencies, such as visible light, $\omega \gg \gamma_0$, $\epsilon(\omega)$ is real and Eq.(1.1) becomes

$$\epsilon(\omega) \simeq \epsilon_b(\omega) - \frac{\omega_p^2}{\omega^2}\epsilon_0 \, . \tag{1.2}$$

Here $\omega_p = \sqrt{\frac{ne^2}{m\epsilon_0}}$ is the plasma frequency of the conduction electrons, at which the free electrons can resonate with the electric field and propagate along a metal surface.

When $\omega \ll \omega_p$, light can only penetrate into the metal for a very short distance and thus is strongly reflected. When ω is of the order of ω_p or larger, light can be absorbed or transmitted into the metal. The wavelength-dependent dielectric constant of gold [20] is shown in Fig. 1.1 and will be used for the calculations in this thesis.

1.3 Ultrafast dynamics of metals

The ultrafast dynamics following optical excitation of metallic materials has been studied in the last decades. It was established that ultrafast optical signals induced by femtosecond optical excitation are caused by rapid heating and relaxation of the electron gas in the metal. The dynamics of optically excited metals, can be described in a four-step-process, the excitation of hot electrons, the equilibration of electrons via electron-electron collisions, the equilibration of electron gas and the lattice via electron-phonon coupling, and finally the cooling of the lattice via heat diffusion. The heated electron gas affects both the real and the imaginary part of the dielectric constant of the metal and causes a wavelength-dependent transient change in both the reflection and absorption spectra of the metal. Therefore, the ultrafast dynamics can be measured optically.

The ultrafast dynamics of bulk gold has been derived from time-resolved measurements [21][22]. Further, gold nano-structures such as metal films [23] and ensembles of metallic nanoparticles [24] have been studied in time-resolved experiments. The diffusive electron motion and cooling by electron-phonon coupling can be well described by the two-temperature model [25]. An electron-phonon coupling constant of $1\sim 4 \times 10^{16}$ $\mathrm{Wm^{-3}K^{-1}}$ has been derived [27].

1.4 Optical induced acoustic vibrations

Acoustic vibrations generated by absorption of ultra-short laser pulses have been demonstrated in many nanosized metallic structures. The hot electrons excited by the optical pump pulse thermalize with the lattice depositing

most of the energy into the lattice. The rapid heating of the lattice causes an impulsive thermal stress in the metal which results in an impulsive expansion and coherent excitation of acoustic vibrations. The confinement of electrons and phonons in nanometer-sized objects causes the physical properties to intrinsically depart from those of bulk solids. Raman scattering experiments [28] [29] [30] and pump-probe spectroscopy [31] [32] have been undertaken to analyze phonons in the frequency-domain and the time-domain, respectively, in nanosized metallic structures.

For metallic particles with a diameter from a few nanometers to tens of nanometers, the breathing vibrational mode has been demonstrated in silver [31], gold [33][34], and gallium [34]. Other types of vibrational modes were found in single nanoparticle experiments with 45-nm diameter gold particles [35]. In most of these experiments, the measured frequency of coherently excited breathing vibrations was in a good agreement with the calculated values. Further, acoustic vibrations were observed in many other geometrical particle shapes. In the beginning of this century, Perner and co-workers investigated the vibrational dynamics of ∼40-nm wide and ∼100-nm long ellipsoidal silver nanoparticles. They observed that the period of the modulation depends on polarization of the probe relative to the particle axis [16]. Hartland and his co-workers investigated vibrational modes of gold nanorods also by laser pulse excitation and found that the period depends linearly on the length of the rod [34][39]. The detection of coherent breathing vibrations of a nanometer-thick gold shell with a sub-micron SiO_2 core arranged in a photonic crystal, was performed by D. Mazurenko et al. [36][37]. Nanoscale gold triangles of different sizes and thicknesses on silicon and glass substrates were analyzed, again with impulsively excited acoustic dynamics [38]. Acoustic vibrations were observed in many more nanostructures [39-45]. Generally, the vibrational periods, depend on the size, shape, and elastic constants of the material. Time-resolved spectroscopy appears to be an excellent tool to examine the material properties of nanometer-sized objects.

1.5 Outline of this thesis

In this thesis, we study the ultrafast dynamics of metallo-dielectric core-shell particles, consisting of a submicron silica-core, tens of nanometer thick gold-shell, and a thin silica cap shell. We measured and interpret the linear and nonlinear optical properties of densely packed core shell particles, using

ultrafast pump-probe experiments.

In chapter 2, we start the research on gold-shell particles by analyzing the linear optical properties in the visible range, both in ordered and disordered arrays and both in reflection and transmission. The interference between the surface plasmon resonance of individual spheres and the periodic arrangement of particles results in a very complex multi-peak spectrum. Calculations of the so-called photonic Karringa-Kohn-Rostocker method, serve to identify surface plasmons and delocalization effects. Highly directional diffraction patterns were observed with hexagonal or cubic symmetry in the photonic crystal structure, corresponding to Fraünhofer diffraction of a collection of ordered small crystallites. Transmission spectra are measured on disordered samples grown on a transparent substrate. Here, a transmission window was observed for all samples which can be interpreted as coherent transport of plasmons. In addition, some special points were discovered on the ordered sample, which give rise to giant reflectivity at the plasmon resonance peak.

In chapter 3, we describe two ultrafast pump-probe experimental setups relying on femtosecond lasers at different repetition rates. One is a standard pump-probe setup with a mechanical delay line and a lock-in amplifier for data acquisition. The other is a so-called Asynchronous Optical Sampling (ASOPS) setup with high repetition rate that does not need a scanning mechanical delay line.

In chapter 4, we analyze the ultrafast response of a 3-D gold-shell photonic crystal employing femtosecond optical excitation. We analyze the decay time and the shape of the response as they depend on both the probe wavelength and pump pulse intensity. The transient reflectivity strongly varies depending on the probe wavelength, which can be accounted for by a pump-induced broadening of the plasmon resonance of the gold-shell particles. The observed electron dynamics can be analyzed in the framework of the so-called "two-temperature model".

Acoustic vibrations of gold-shell particles following the optically induced ultrafast electronic response is discussed in chapter 5. We introduce a two-shell model developed on basis of Lamb theory, to calculate the vibrational mode frequencies. By employing pump-probe experiments, we excite the acoustic vibrations of the gold-shells and detect via modulations of the optical reflectivity. Spherical breathing modes and thickness modes of vibrations were identified in a 3-D ordered array of the particles. For a disordered array, elliptical modes were excited and observed. Finally, we demonstrate

a dependence of the vibrational period on the gold-shell size and also the excitation on crystal order.

In chapter 6, we demonstrate acoustic vibrations in elliptical gold-shell particles, deformed by ion beam irradiation. The observed periods show a dependence on the orientation of particles, corresponding to the longitudinal vibrations along the long and short axis. From fast oscillations observed in short time scale, we conclude that the thickness of gold shell is locally changed by ion beam irradiation.

In short, this thesis deals with the ultrafast dynamics of metallo-dielectric core-shell particles in detail, discusses the linear and nonlinear optical response, examines ordered and disordered arrays, identifies electronic and acoustic responses, and distinguishes spherical and elliptical vibrations and geometry.

Chapter 2

Linear optical properties of densely packed gold-shell particles

Abstract In this chapter, we analyze the linear optical properties of SiO_2/Au/SiO_2 core-shell particles, as they are influenced by their size and organization. In case of close-packed particle arrays that form a three-dimensional photonic crystal structure, a highly directional diffraction pattern was observed with hexagonal or cubic symmetry. The optical transmission of a "disordered" dense packing of particles suggest a plasmon transport effect.

2.1 Introduction

2.1.1 Metal structures

The study of the optical properties of small metal particles can be traced back to 150 years ago. Michael Faraday showed that the red color in stained glass is due to small-sized gold particles. Later the first theoretical framework to explain the interaction between light and matter was published by Gaustav Mie around 100 years ago[51].

Metal shows completely different optical properties from these of dielectric materials, because of the existence of free electrons. These may carry collective excitations, known as surface plasmons. In principle, they correspond to an optically induced coherently oscillating charge distribution at the metal surface and give rise to strong surface electromagnetic fields. By making metal structures with a size scale comparable with wavelength of light, the surface plasmon resonance can be enhanced and its frequency controlled. As early as 1902, Wood has discovered anomalously sharp minima and maxima in the reflection spectra of metallic gratings [46]. After about 60 years, people could theoretically understand this phenomenon [47]. Simply speaking, the anomalies are caused by the presence of the two resonances: (i) the diffraction from ordered grooves of the surface (proposed by Rayleigh) [48]; (ii) the plasmon resonance of the metal surface. These resonances may interfere with each other and produce a Fano-like profile of the reflectivity spectrum [49][50].

At the end of the twentieth century, the interest in metallic structures was renewed and boosted by the rapid development of nano-technology. Nanoscale holes, grooves, and particles can be fabricated with sizes smaller than or comparable to the wavelength of light. Ebbesen and his co-workers [12] discovered an unexpectedly high optical transmission through an array of subwavelength holes in a metal film of 200-nm thickness. Efficiencies were found to be about 1000 times higher than that expected from the bare area of the sub-wavelength holes. The transmission maxima are the result of resonant excitation of surface plasmons, which radiate into free space at both sides of surfaces of the metal film.

In 2002, Lezec and his co-workers discovered a highly directional emission from a single sub-wavelength metal film aperture surrounded by surface corrugations[13]. This so called beaming is due to the formation of electromagnetic surface resonances. The direction, width, and wavelength at which the beam occurs can be controlled by the geometrical surface parameters of the structure.

From the beginning of the 21st century, with the understanding of plasmons and the advanced techniques of fabrication, metal nanoparticles attract renewed interest because they bridge the gap between atoms and bulk solids and have novel properties. By controlling the size and shape of the metallic structures, the resonance frequency can deviate from the bulk metal value and give potential applications for sub-wavelength optical devices, nonlinear

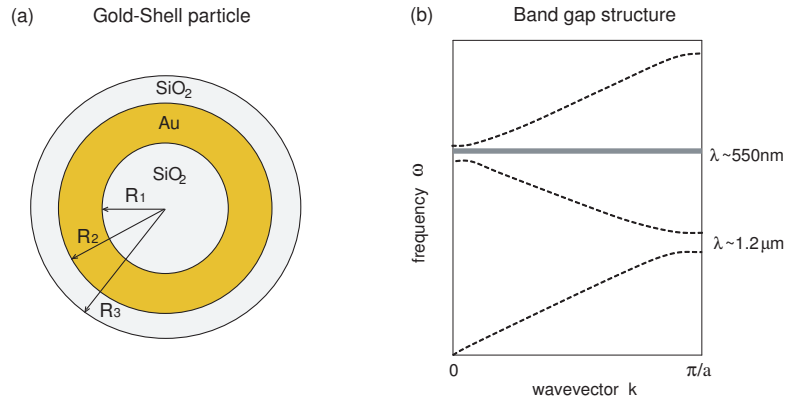

Figure 2.1: (a) Sketch of a gold-shell particle. (b) Sketch of the band gap structure (dotted lines) of a 3-D photonic crystal formed by gold-shell particles (R_1=228 nm, R_2=266 nm and R_3=267 nm) and the plasmon resonance frequency of gold (gray bar).

optics, biological labelling, and sensing.

For a spherical metal particle which is much smaller than the wavelength of light, the surface plasmon resonance frequency is weakly size dependent. For example, by increasing the size of gold particles from 15 nm to 40 nm, the absorption peak position of extinction spectra shifts from 540nm to 570nm[15]. On the other hand, when the diameter of the particle is comparable to the wavelength of light, the surface plasmon resonance shifts towards lower energies, becomes broader, and finally splits into a series of separate multipole modes. This phenomenon is caused by phase retardation[52][53].

Recently, the progress in the synthesis of metallo-dielectric composites allows one to fabricate core-shell metallo-dielectric particles with a size of the wavelength of visible light [17]. Fig. 2.1(a) shows a sketch of a gold-shell particle, the size of which can be fabricated with a radius around 200 nm. The situation of spherical metallic nanoshells is even more complicated, because it contains two types of surface plasmons: one localized on the internal surface and one localized on the external surface of the shell. In case of a sufficiently thin shell, those plasmons can be coupled into symmetrically and antisymmetrically hybridized modes as shown in Fig. 2.2(a) and (b). At close packing some of these plasmon modes can become delocalized, i.e. be coupled out to neighboring particles and transfer energy over long distances

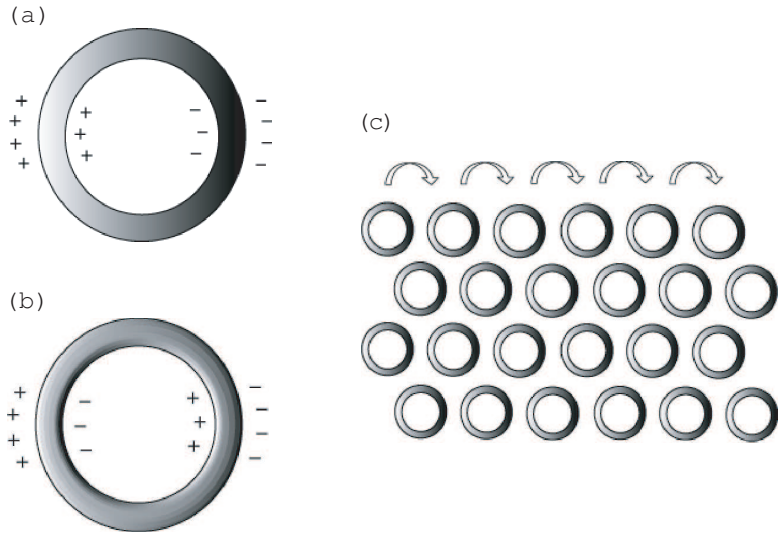

Figure 2.2: Sketch of internal and external surface plasmons on a metallic shell for (a) symmetrical and (b) antisymmetrical coupling, respectively. (c) sketch of coupling between an array of shell particles.

as schematically shown in Fig. 2.2(c). Recently, hybridization of plasmon modes was reported in very complex multishell particles composed of a silica core and consecutive shells of gold and silica [18].

By arranging gold-shell particles periodically, 2D or 3D lattice structures can be formed, which are called photonic crystals. Fig. 2.1(b) shows a sketch of a band gap structure of a 3-D photonic crystal formed by a periodic array of gold-shell particles with R_1=228 nm, R_2=266 nm and R_3=267 nm, leading to a plasmon resonance frequency of gold sitting the band gap at 550 nm. A complete photonic band gap is predicted in the infrared, at $\lambda \sim 1.2\mu m$, and a seconder-order band gap at around 600 nm [59]. In contrast with normal dielectric photonic crystals, the metal in this structure supports surface plasmons and allows coherent oscillations of free electrons to occur at optical frequencies in each individual particle. Therefore this sample is particularly interesting because the plasmon resonance is thought to be very close to this second-order band gap (see Fig. 2.1). The optical properties are influenced both by lattice diffraction and surface plasmon resonances. The former one leads to Bragg scattering and the formation of a band gap in the visible range. The latter one gives rise to absorption and emission into free

space of light.

In order to study the nonlinear optical properties of gold-shell particles, the subject of this thesis, it is imperative to first understand the linear optical properties. In this chapter, we analyze the reflection, transmission and diffraction properties of ordered or disordered densely packed submicron $SiO_2/Au/SiO_2$ core-shell particles. One sample was arranged in a 3D periodic lattice and forms a photonic crystal on a Si-substrate. The other samples have particles of different sizes but contain much more disorder and are only ordered on a much smaller scale. Because these particular samples are fabricated on glass substrates, transmission spectra can be measured. It will appear that the linear properties are very complicated and rich, because of the interplay between plasmon resonances and the photonic stop band related to multiple Bragg scattering.

2.2 Sample and experiment details

The metallic-dielectric spheres were fabricated by C. M. Graf and J. Penninkhof in the Debye Institute for Nanomaterials, Department of *Soft Condensed Matter*. The particles consist of a silica core covered by a gold shell and capped with a silica outer shell, as sketched in Fig. 2.1 (a). We use R_1, R_2, and R_3 to denote the radii of the different interfaces.

The gold-shell particles were formed in a multi-step reaction [17]. First spherical silica particles were grown in a stepwise seeded Stöber growth process, with diameters in the range between 300 nm and 500 nm. Subsequently, they were functionalized with 3-aminopropyl-trimethoxysilane to enable the attachment of pre-produced gold nanoclusters of 1-2nm in diameter. The gold shell was then grown in a $HAuCl_4/K_2CO_3$ solution. This results in reductive growth and coalescence of the deposited gold nanoclusters and the formation of a closed thin gold shell. The thickness of the gold-shell was controlled by choosing a ratio of the number of gold nanoclusters and the volume of the gold salt solution. An additional capping silica shell was grown via functionalization of the silica-core/gold-shell particles by polyvinyplayrrolidone [55], after which the colloids were transferred into ethanol to enable the growth of the outer silica shell again via a Stöber reaction. Subsequently, a droplet of the colloidal suspension was deposited on a silicon or a silica substrate, and carefully dried. Since the silica outer shell reduces the Van-der-Waals interparticle forces, the particles can self-assemble to form a periodic lattice

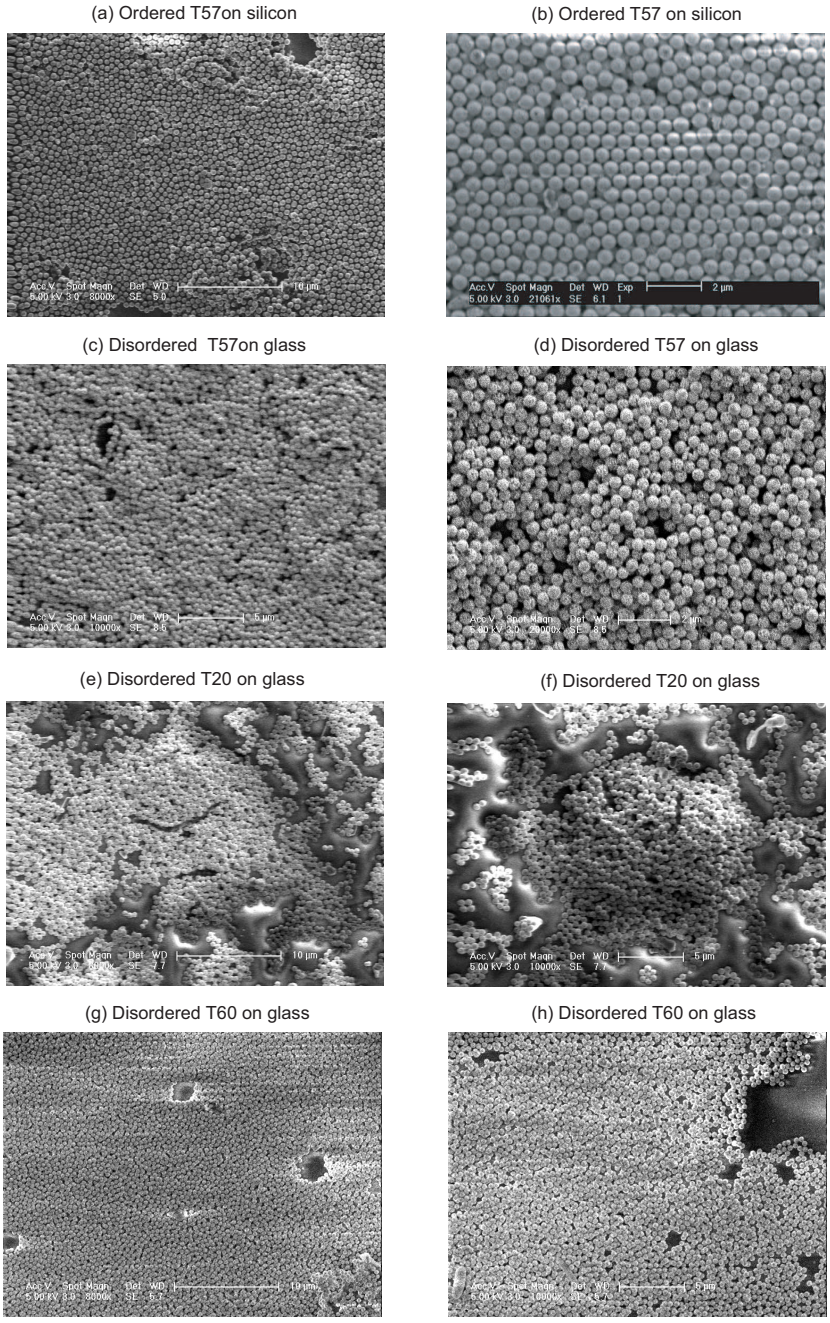

Figure 2.3: The scanning electron microscope (SEM) pictures of samples.

in the form of a close-packed array of particles. On the sample surface, the thickness of the obtained 3-D photonic crystal structures gradually varies from one monolayer to several monolayers. However, the degree of ordering of the particles is influenced by the substrate, temperature, and further conditions, that are unfortunately largely beyond control. We possess only one nicely ordered 3-D photonic crystal structure, while the others are strongly disordered.

Fig. 2.3 shows scanning electron microscope (SEM) pictures of the samples we used. Fig. 2.3(a) shows the close-packed highly ordered array of several monolayers of particle T57 on a silicon substrate, which has R_1=228 nm, R_2=266 nm, and R_3=276 nm. Fig. 2.3(b) is a zoomed-in part, where clearly close-packed structures over several microns are discernable. Fig. 2.3(c) and (d) show the same particles but on a glass substrate, which lead to a more rough and disordered structure. Apparently, here the 3-D photonic order is less prominent but ordering on the local scale is still visible.

Similarly Fig. 2.3(e) and (f) show the SEM pictures of T20 gold shell particles, with size R_1=205 nm, R_2=255 nm, and without a capping silica shell. In Fig. 2.3(g) and (h), the particle size is the smallest, R_1=156 nm, R_2=181 nm and R_3=221 nm, and called T60.

From SEM pictures, a size dispersion of particles of $\sim$5% was deduced. All the following experiments described in this chapter were carried out in T57, T20, and T60 samples.

The experimental setup is described in detail in Chapter 3. Stationary reflection spectra were obtained using a continuum white light source generated by self-phase modulation of amplified femtosecond pulses in sapphire. The white light was focused on to a 30-μm spot on the sample surface, with an incident angle θ varying from 6° to 30° from the normal. The reflected and diffracted light was collected by a lens, passed via a spatial filter, and focused into an optical fiber, which acts as the entrance of a spectrometer. With a charge-coupled device (CCD) cooled by liquid nitrogen, 1-nm resolution spectra can be recorded. The reflection measurements were compared to that of a bare silicon substrate, and have been calibrated using the independently measured silicon reflectivity spectrum. Alternatively, by placing a suitable screen in front of the lens, the reflected and diffracted patterns can be projected and then recorded by a photo camera. All experiments were carried out at room temperature.

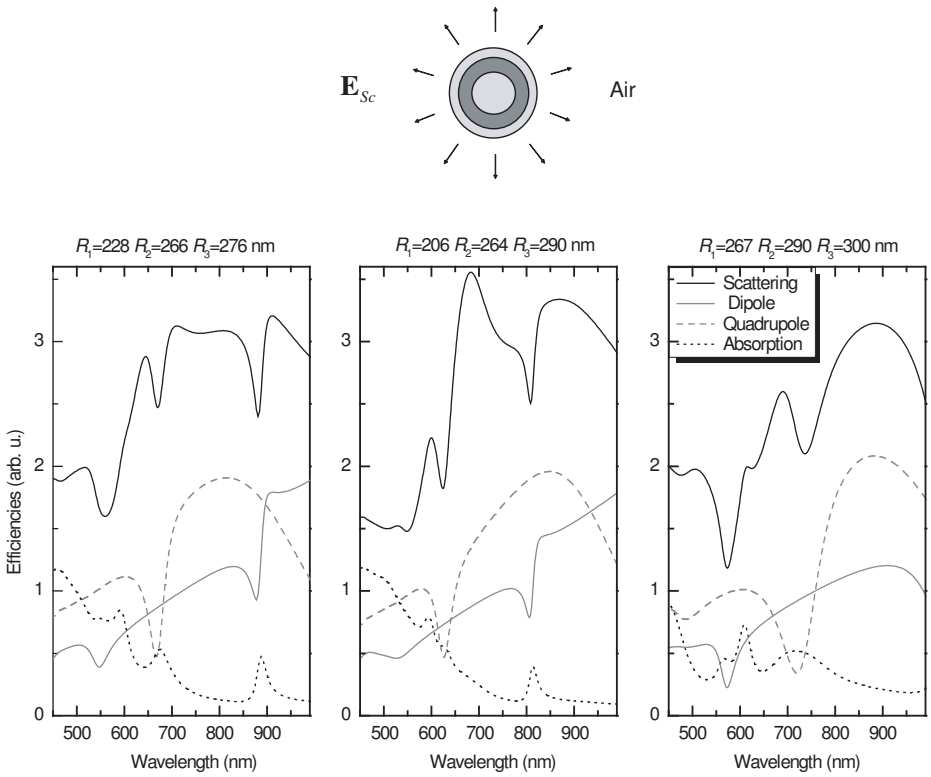

Figure 2.4: Calculated absorption (black dotted line), dipole (gray solid line), quadrupole (gray dashed line), and scattering (black solid line) efficiencies of a single gold-shell particle for different sizes.

2.3 Calculation results

The first attempt of computing the linear reflectivity spectra of an ideal 3-D photonic crystal of gold-shell particles on a silicon substrate has been described by D. Mazurenko in his thesis [36]. The band structure of an *infinite* photonic crystal was calculated by a model of A. Moroz, using a 3-D photonic variant of the Korringa-Kohn-Rostocker (KKR) method [57][58][59]. In this section, we rely on the work of Mazurenko and Moroz, present the calculation results, make a comparison, and conclude with a discussion. The computer code was developed by A. Moroz[59](see also http://www.wave-scattering.com).

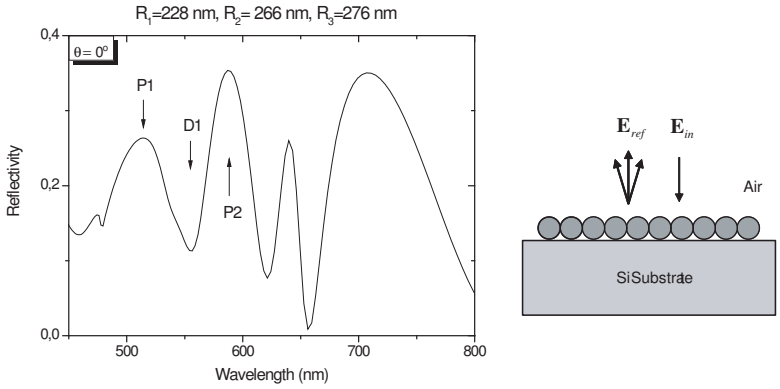

Figure 2.5: Calculated reflection spectrum of a single close-packed hexagonal layer of gold-shell particles on an infinite silicon substrate for T57: R_1=228 nm, R_2=266 nm, and R_3=276 nm.

2.3.1 Calculated results of a single particle, single layer, and multi-layer structure

The optical properties of a single spherical core-shell particle has been calculated taking into account a sufficient number of higher harmonics, using the Mie formalism with the extension by Aden and Kerker [56]. The experimental dielectric constants of gold displayed in Fig. 1.1 were used to model the gold shell dielectric properties [20], while the refractive index of silica was set at $n(SiO_2) = 1.45$. In Fig. 2.4, the absorption (black dotted line), dipole (gray solid line), quadrupole (gray dashed line), and scattering (black solid line) efficiencies of a single gold-shell particle for different sizes are displayed as calculated for three types of particles. The scattering efficiency is the sum of the three contributions. From Fig. 2.4, one may distinguish two dipole contributions in the visible light range (ie. at 560 nm and 900 nm for a T57 particle), which are due to the hybridization of the inner and outer surface plasmon resonance. The one around 560 nm is not very sensitive to the size of particles, while the other one in the near infrared light range shifts considerably with the size. We can also notice that for gold-shell particles the quadrupole resonance gives a stronger contribution than the dipole resonances.

The reflectivity spectrum of close-packed particles arranged in layers is calculated using the layered variant of the photonic KKR method (LKKR)[60].

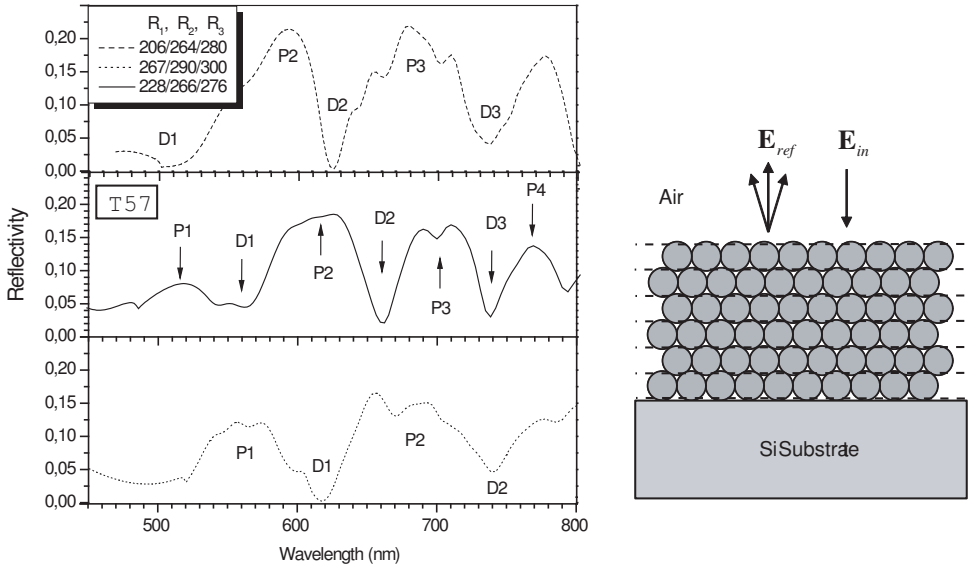

Figure 2.6: Calculated reflection spectrum along the (1 1 1) crystallographic axis of a photonic crystal composed of 12 fcc-ordered layers of gold-shell particles for different sizes.

In the frame work of LKKR method, the space is divided into three parts: (i) the substrate; (ii) the photonic crystal composed of a close-packed periodic array of identical multi-shell spheres; (iii) air. The substrate and the photonic crystal dimensions are taken infinite in the plane of the surface in the x and y directions, while the incident light propagates along the z-axis from air. Each layer in the photonic crystal is a hexagonal 2-D periodic array of particles. The solutions of the Maxwell equations in the substrate, air, and each of 2-D layers particles are carried out and connected by applying the boundary conditions to compute the reflection.

Fig. 2.5 shows the calculated reflectivity spectrum of a single layer of close-packed gold-shell particles T57 on an infinite silicon substrate at incident angle $\theta = 0$. The spectrum shows a quite complicated structure in the visible light range.

A multi-layer calculation is shown in Fig. 2.6 for the reflectivity spectrum of a (1 1 1)-oriented structure composed of 12 closed-packed layers of T57 particles on a silicon substrate again with incident angle $\theta = 0$.

2.3.2 Discussion

In the calculated result for the multi-layer structure of Fig. 2.6, one observes a quite complex structure depending on the size of particles. The multitude of peaks and dips in the visible range, are denoted by P1, P2, P3, and P4 for the peaks and D1, D2, and D3 for the dips, respectively. By varying the size parameters R_1, R_2, and R_3 and the number of layers, we can examine the sensitivity of peaks and dips when the geometrical parameters of the particle and lattice are varied. If a peak or dip in the spectrum depends on R_1 or R_2, it is related to plasmon resonances of the inner or outer gold shell surface, respectively. A R_3-dependence reflects effects of inter-particle coupling or long-range photonic interaction. The latter should produce an angle dependent reflectivity in the experiment. Finally, a dependence on the number of layers points to effects of the periodic crystal lattice and also should be accompanied with an angle dependence.

First, we compare and analyze the calculated results of a single layer and a multi-layer structure. We notice that increasing the number of layers, spectral changes take place mainly in the red region, which includes P3, D3, and P4. Other calculations show that 6 layers are already sufficient to approximate an infinite photonic crystal. Therefore scattering of light involves interference between lattice planes and penetration to depths of typically about 6 layers. In case of an ideal infinite 3-D photonic crystal, light is expected to be specularly reflected. At the blue side, the spectral positions of P1, D1, and P2 do not show any layer dependence, which suggest that they involve less penetration and perhaps are produced predominantly by scattering at the surface layer (compare Fig. 2.5 and Fig. 2.6).

Second, calculations show a R_3-dependence of the position of most of peaks and dips, which suggest that they are photonic or at least sensitive to inter-particle coupling.

Third, it appears that the size parameter R_1 governs the position of P1, D1, P2, and D2, which means that they are related to a plasmon resonance on the inner shell. The position of D1 is also controlled by R_2, and coincides with the dipole resonance of a single particle (see Fig. 2.4). It suggests that D1 originates from the hybridization of the dipole plasmon resonance of the inner and outer surfaces of the shell.

Forth, the position of D2, located at 660 nm for particle T57, and at 625 nm and 740 nm for the smaller particle and bigger particle, respectively, coincides with the quadruple resonance dip in single particle calculations (see

Peaks /dips	Position dependence	Plasmon resonance	Photonic (angle dependence)	Discussion
P1 520 nm	R_1, R_3	Dipole	Yes	Inner shell dipole resonance delocalized in the periodic crystal lattice. *Bragg scattering* contribution.
D1 560 nm	R_1, R_2, R_3	Dipole	Yes	Single particle hybridized dipole plasmon resonance absorption of gold shell coupling with lattice.
P2 600 nm	R_1, R_3	Dipole	Yes	Dipole plasmon resonance of gold shell inner cavity coupled to lattice band gap. *Band gap* contribution.
D2 660 nm	R_1	Quadruple	No	Quadruple resonance absorption of single particle gold shell inner cavity.
P3 700 nm	R_3 layers	Quadruple	Yes	Quadruple plasmon resonance of gold shell inner cavity coupling with lattice band gap. *Band gap* contribution, reflected in specular beam.
D3 740 nm	R_3 Layers	-	Yes	Interference of the periodic crystal lattice.
P4 770 nm	R_3 layers	-	Yes	Interference of the periodic crystal lattice.

Table 2.1: Classification of calculated reflection spectra of multi-layer ordered T57 structures .

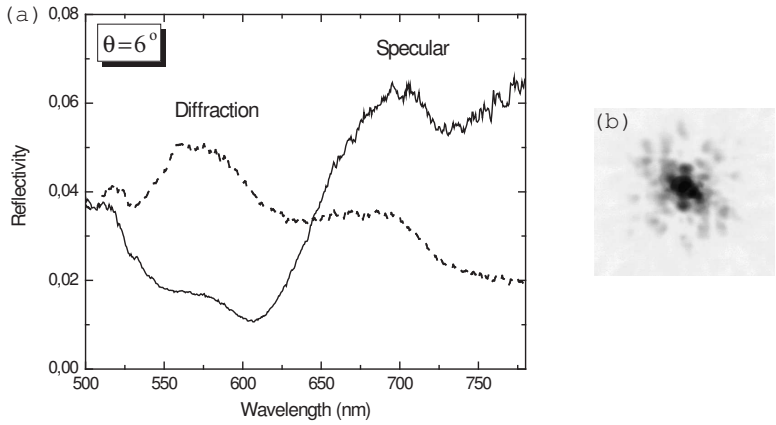

Figure 2.7: Linear reflection spectra of specularly reflected (solid line) and diffracted light (dotted line), respectively, from multi-layer of ordered T57 sample (R_1=228 nm, R_2=266 nm and R_3=276 nm). Incident angle $\theta = 6°$. Right side pictures shows the diffraction pattern from the measured point.

Fig. 2.4, gray dashed lines). It suggests that the dip corresponds to a local quadruple resonance of the inner shell surface with weak coupling to others.

Finally, in Table. 2.1, we summarize the calculated dependencies on the particle parameters and classify the spectral features.

2.4 Linear optical properties of *ordered* T57 sample

We now turn to the measurements on the ordered sample made of T57 particles on a silicon substrate, R_1=228 nm, R_2=266 nm, and R_3=276 nm. The linear optical properties turn out to be strongly dependent on the position of the sample surface, reflecting the fact that the number of layers and the local organization of particles is strongly varying over the sample surface. Fig. 2.7 shows a typical reflectivity spectrum (a) with incident angle of $\theta = 6°$, and diffraction pattern (b) both on one spot on the sample surface containing several layers of particles. The solid line in Fig. 2.7 (a) is the spectrum of the specularly reflected beam, and the dotted line is that spectrum of the diffracted beam. From Fig. 2.7, the specular beam and the diffracted light have quite different spectra. The red light of wavelength λ >650 nm mainly present in the specular beam, while the diffracted light is residing in the

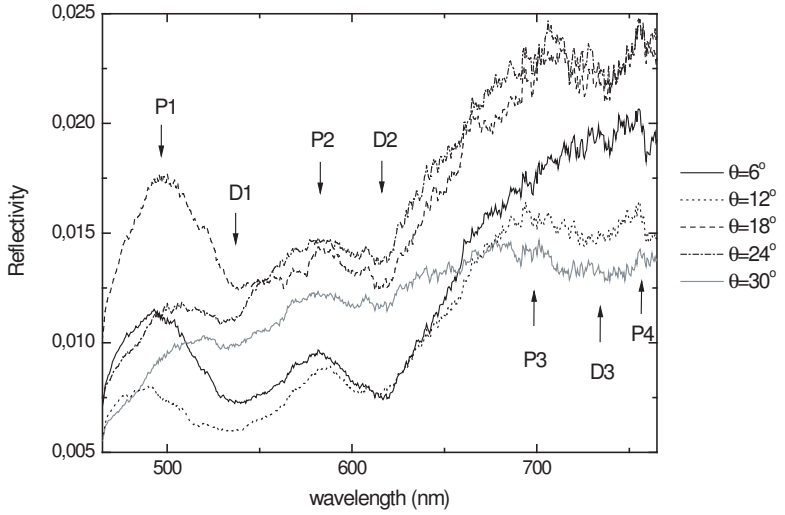

Figure 2.8: Angle dependent linear reflection spectra of multi-layer ordered T57 sample.

green. This seems natural considering the size of particles d ∼550 nm: the green light is easily scattered because it fits the dipole resonance of particles.

In Fig. 2.7(b), the diffraction pattern is distributed over a large angle while the specular reflection beam remains narrow and can be distinguished as the central intense spot. The angular distribution of the diffraction pattern is inhomogeneous and strongly dependent on the position on the sample. However, the spectra of the specular and diffracted beams are roughly constant. At the rear cover of this thesis, we offer color pictures of these diffraction patterns. All the pictures look green because the incident "white" light spectrum peaks in the green. As noted earlier, for an ideal, infinite 3-D photonic crystal sample, the reflected light should only consist of a specular beam. However we always observed quite complex diffraction patterns which we attribute to defects and roughness of the sample surface. We will discuss the diffraction patterns in some detail in Sec. 2.4.2.

2.4.1 Angular dependence

More detailed features of the linear spectrum appear in an angle-dependent measurement. We choose a typical thick spot on the sample surface, and

change the incident angle θ of the incoming beam from $\theta = 6°$ to $\theta = 30°$ in steps of 6°. In this experiment, all the spectra were taken at the same sample point, while the size of the focused white light spot is kept to 30-μm diameter. Both the specular beam and the diffracted light were collected simultaneously with an opening angle of 0.2 rad and displayed in Fig. 2.8. The spectra show several peaks in the visible light range and reasonably resemble the calculated result on a 12-layer fcc structure. By comparison with the calculation and measurements, we denote the peaks at 500nm, 580nm, 700nm and 760nm as P1, P2, P3 and P4, respectively, and dips at 530nm, 620nm, and 740nm, as D1, D2 and D3, respectively. The measured positions of the maxima and minima indeed slightly depend on the incident angle.

In an attempt to understand these complex spectra, we distinguish two types of contributions, one from the surface plasmons of the gold shell particles (Mie resonance), one from the periodic ordering of particles by Bragg scattering giving rise to band structures. These two contributions can become mixed and give rise to our quite complex measured spectra. The Bragg scattering and band-gap contributions, associated with multiple scattering and ordering of particles, must shift when varying the incident angle of light. For the surface plasmon resonance of single particles, the spectral peak position should be angle independent because of the spherical symmetry of isolated particles. With the help of the predictions from the calculations in the former section, the measurement results can be specified further. In Table. 2.2, we summarize the measured dependences of the linear reflectivity spectrum.

From Table. 2.2, we find that the observed spectra reasonably confirm the prediction from calculation at some peaks and dips, such as P1, D1, P2, and P3. The angular dependence relation were also correctly predicted at P1, D1, P2 and P3. However, some peaks and dips did not show clear agreement with the calculation. The observed dip D2 at 620 nm does not depend on incident angle, we considered it to be the calculated quadrupole plasmon resonance of the internal gold shell cavity, which should appear at 660 nm for our particle. The observed dip D3 at 730 nm is very close to the calculated dip at 740 nm, which depends on interference between layers and should show an angle dependence. However we did not observe this. The peak P4 probably coincides with the calculated peak P4 at 770 nm, which originates from the surface plasmon coupling with the lattice. Unfortunately, P4 is close to the spectral limit of our probe light which is generated by self-phase modulation in a sapphire crystal of the 800-nm pump light, and cut

Peaks /dips	Spectral position	Angle depend	Classification comparison	Nature
P1	490-525 nm	Yes	P1(520 nm)	Plasmon resonance delocalized with periodic lattice.
D1	520-540 nm	Yes	D1(560 nm)	Plasmon resonance absorption coupling with lattice ordering.
P2	580-590 nm	Yes	P2(600 nm)	Coupling between plasmon resonance and the crystal lattice band gap.
D2	620 nm	No	D2(660 nm)	Localized internal quadrupole plasmon resonance.
P3	680-720 nm	Yes	P3(700nm)	Surface plasmon resonance coupling with lattice band gap.
D3	730 nm	No	D3(740 nm)	Not sharp, interference of layers.
P4	>750 nm	Unclear	P4(770 nm)	Surface plasmon resonance coupling with lattice.

Table 2.2: Classification of linear reflection spectra structures of multi-layer ordered sample surface for T57.

off by a band filter around 800 nm. It is therefore not possible to detect any angle dependence of P4.

There are a lot of factors that may influence our experiment and let it deviate from the ideal situation. The 5%-size dispersion of particles is one. Second, the particles were fabricated in solution and were dried on a substrate. It may occur that the cap layer of silica cracks making it a non ideal dielectric shell. Third, the size of close-packed photonic crystals is not infinite. As one can see in the SEM picture from Fig. 2.3, the crystal size is limited in a few μm, which is smaller than our 30-μm white light focus size. Finally, the calculated spectrum was based at $\theta = 0°$ of incidence light, while the experiments were taken from $\theta = 6°$ to $\theta = 30°$. All of these reasons can influence the measured result for an ideal photonic crystal.

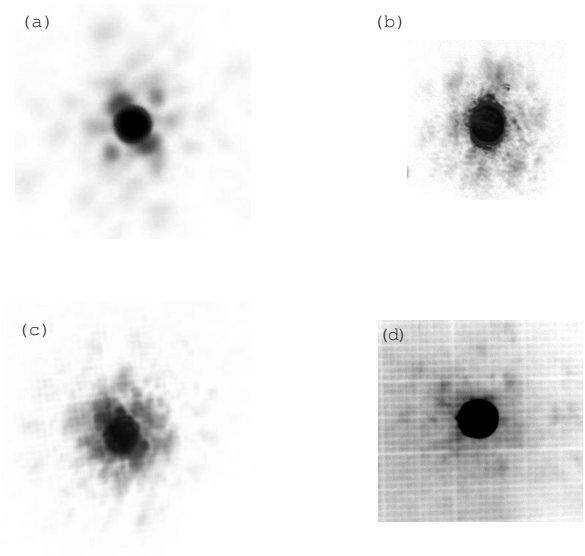

Figure 2.9: Diffraction pattern pictures of sample T57. (a), (b) and (c) were shoot from multi-layer ordered sample on silicon, reflection direction. (d) was shoot from multi-layer disordered sample on glass.

In conclusion, we can classify the structures of the reflection spectrum in the visible light range of ordered multi-layer gold-shell photonic crystal sample to a reasonable extend by comparison of the measurement results with the calculated results.

2.4.2 Diffraction patterns

Remarkable diffraction patterns in reflection were observed with hexagonal or square symmetry in reflection. By putting a paper sheet into the reflected beam, the diffraction patterns can be catched by a digital camera. In Fig. 2.9, we show some diffraction patterns of sample T57. (a), (b), and (c) were taken from thick parts on the ordered sample while (d) was taken from a disordered T57 sample on glass.

For an ideal infinite photonic crystal, one expects exclusively specular reflections simply because there are no small wave number contributions available in the structure. However, we observed diffraction patterns with a highly inhomogeneous distribution in space. This diffraction pattern signi-

fies that our sample is not ideal as can be seen in the pictures of Fig. 2.3(a) and (b). According to these pictures, we can consider our sample as a collection of small crystallites that is coherently illuminated by our 30-μm light spot. The shape and organization of the local crystals are likely to generate the diffraction pattern. From SEM pictures in Fig. 2.3(a) and (b), ordering of particle clusters can indeed be clearly observed in the *ordered* sample. The particles locally form close-packed highly ordered structures several monolayers thick on the silicon substrate to a size of up to 10 μm. At the sample surface one observes those crystallites. We assume the crystallites to act as tiny photonic crystals producing the linear spectra, already discussed in the former section. In our experiment, the incident white light beam was focused to a 30-μm spot, coherently illuminating these small crystallites. Thus, each crystal with its characteristic plasmonic and photonic response, produces a specularly reflected beam. All beams of the crystallites will interfere and produce a diffraction pattern in the far field that is characteristic for the local distribution of crystallite sizes and shapes in the focus of the probe beam.

In contrast, Fig. 2.9(d) shows the reflection pattern for a disordered T57 sample on glass. Compared to the ordered sample, the reflected light is less directional and symmetrical, which points to a smaller local crystal size and less ordering of the crystallites. From the SEM picture in Fig. 2.3 (c) and (d), the disordered sample indeed has a more rough surface and only few particles order close-packed. The local crystallites are clearly much smaller than in the ordered sample.

Fourier transformation

The diffraction pattern of a given symmetric structure can be calculated by a 2-D Fourier transformation. In our sample, the illuminated area contains many crystallites, and each crystallite is thought to act as a scattering light source around the 550-nm plasmon wavelength. We simplify each crystallite to be a 4-μm size hexagon, organized in various symmetries. The diffraction pattern can be computed by Fourier transformation of this spatial pattern with 550-nm wavelength as the parameter.

In Fig. 2.10, we present the calculated results of two types of structures. Fig. 2.10 (a) shows the input structure with hexagonal symmetry, and Fig. 2.10 (b) the corresponding output. The total size of the input image is taken as the illuminated spot size on the sample, 30-μm, which contains $\sim$7 crystallites along the diameter chain. The diffraction is a hexagonal

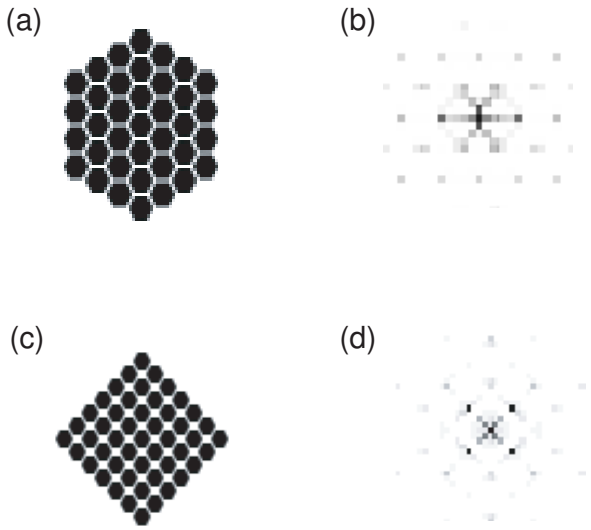

Figure 2.10: Fourier transformation of some sketch. (a) and (c) are inputs with hexagonal and square symmetry, (b) and (d) are the outputs.

pattern with diffraction angle 8° of the first order, and resembles our observed diffraction pattern of Fig. 2.9 (a) and (b). Fig. 2.10 (c) corresponds to square symmetry of hexagonal crystallites. The output at Fig. 2.10 (d) gives a square pattern with diffraction angle also 8° determined by the distance between crystallites and resembles the measured picture Fig. 2.9 (c), which suggests that the organization of the selected sample point for Fig. 2.9 (c) has a square symmetry.

2.4.3 Island and point of giant reflection

Island

There are few remarkable and special points discovered at points on the ordered sample. One is the response of a one-monolayer island. At the edge of the sample, single close-packed layers seem to be formed that assemble in small groups to form islands. The size of an island can be determined by moving the probe spot across the sample edge. When the laser spot hits an island, the reflection spectrum suddenly changes and gives an unusual spectrum until the other edge of the island is crossed. Micrometer sized

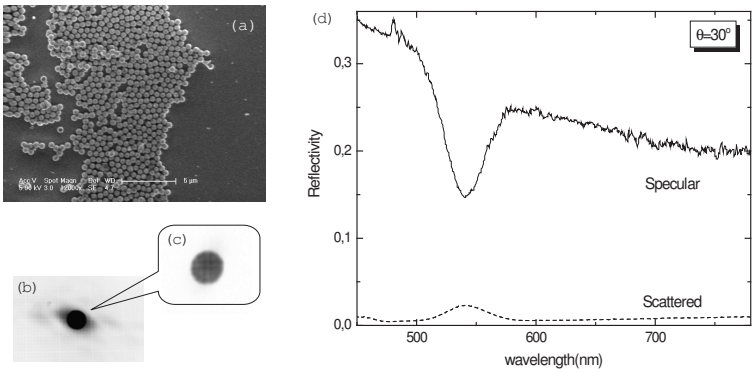

Figure 2.11: (a) SEM picture of an island point on ordered T57 sample. (b) the diffraction pattern of an island point and (c) is zoom in of specular beam. (d) the spectrum of the point same as (b) and (c) with incident angle $\theta = 30°$.

islands were found in this way, and under SEM we managed to take pictures of such islands.

In Fig. 2.11(a), a SEM picture shows a long island of about 8 μm in width, where particles order in a single close-packed layer. Fig. 2.11(b) shows the reflection and diffraction pattern at an incident angle $\theta = 30°$, and (c) is a zoomed-in picture of the specular beam. Here the island is smaller than the light focal spot of 30 μm, and the specular beam is bright and smooth. In Fig. 2.11(b), the diffraction spots are more intense in the left and right side to the specular circle. As we discussed in the former section, this is the result of interference and determined by the shape of the crystallites. In case of a long island, one expects to have a pattern resembling the diffraction of a slit. We should mention that the picture (a) and (b) are not taken at the same sample point, but the island shape and size are comparable. However, Fig. 2.11 (b), (c) and (d) are taken at a single sample point.

Fig. 2.11(d) shows the measured spectrum of the specular beam (solid line) and the diffracted light (dashed line) by the island. Remarkably different features are observed from that of the typical multi-layer sample point. The specularly reflected beam has a smooth spectral curve which is the reflection of the silicon substrate. Identical reflectivity spectra of silicon were measured by Philipp and Ehrenreich [61]. Beside that, a significant dip shows up at 540 nm, corresponding to the plasmon resonance of the gold shell. If we consider the incoming light shining on the sample, it coherently excites the

plasmon resonance in particles at the correct frequency. Part of the energy turns into heat and is absorbed by the particles, part is coupled out again as electromagnetic waves, and contributes to the reflected and the diffracted beam. Since the particles are close to each other and coherently driven, the entire island act as a light source at the plasma resonance wavelength. Due to its small size and shape, the diffraction angle should be rather large. The diffraction angle of the first order spot at left and right direction in Fig. 2.11(b) is 0.08 rad, therefore the width of the island can be calculated to be 6.75 μm by the formula $asin\theta = \lambda$, which is consistent with the measured island size. The measured spectrum of diffracted light clearly shows a peak at 540 nm, exactly where the plasmon resonance is located.

However, except for the dip at 540 nm, the spectrum of the small island with a single layer of particles does not resemble the calculated structure for a single layer. It is remarkable that the quadrupole resonance is missing while the dipolar one at 540 nm is clearly present. The sharp quadrupolar resonances in the calculation displayed in Fig. 2.6 are somehow severely suppressed in this island. Compared with the ideal infinite layer in the calculation, the size of the island is apparently too small to make the coupling between plasmon and lattice appreciable.

Point of giant reflection

Another unusual effect was observed in our experiment on the ordered sample T57, namely a *giant reflectivity* at 510 nm. Fig. 2.12 displays the spectrum, which is observed vs. incident angle, together with the corresponding diffraction pattern. The spectrum has a huge peak around 510 nm. Compared with the former calculation and measurement result, this peak should correspond to the Bragg scattering of the periodic lattice, that should indeed show an angle dependence. In Fig. 2.12 the peak position shifts from 500 nm to 510 nm for increasing incident angle, and decreases in height. In this experiment, both the specular beam and the diffracted light contain the high peak at 510 nm. The total reflectivity at the peak is up to 20%, which is much higher than on normal multi-layer sample points. At other wavelengths in the range from 550 to 750 nm, the reflectivity keeps at the same level and same spectral shape as we observed on our typical sample point (see Fig. 2.8). On the other hand, the diffraction pattern of this special point gives a remarkably regular structure as shown in the inset of Fig. 2.12.

This phenomenon only appears on some special, randomly distributed

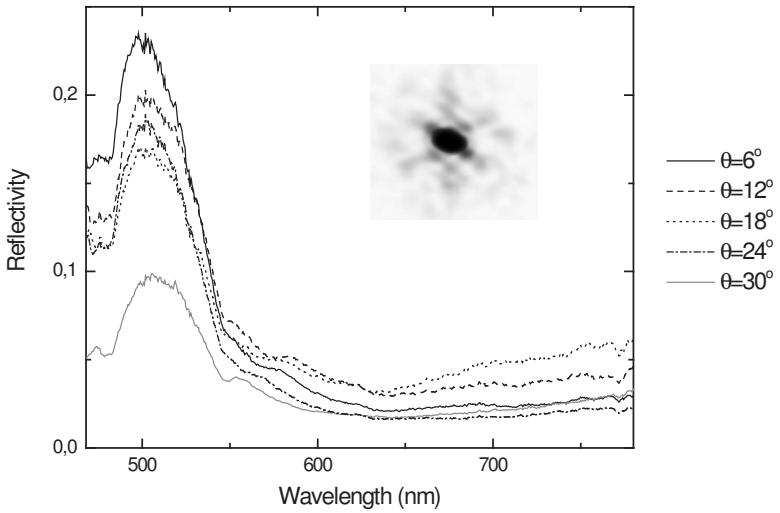

Figure 2.12: Spectrum of point of giant reflectivity of ordered T57 sample with various incident angles, and corresponding different pattern.

points at thick parts of the sample. They are stable in time and space, but only appear in very small areas of few micrometer size. We suspect this to be a mountain that has more layers than the surrounding area, in which resonant coupling and emission can occur. Probably, the diffraction patterns should be less disturbed by surrounding crystallites and only determined by the geometric shape of the mountain.

This giant reflection point is very difficult to catch in SEM pictures because the precise location on the sample is not know. However, we believe that the phenomena is an accidental resonance in the sample structure, controlled by the geometry, organization, and ordering of particles.

2.5 Size dependent spectra of *disordered* particles

In the previous section, we studied the linear reflectivity of an *ordered* gold-shell photonic crystal. Now we examine densely packed *disordered* samples and measure the spectra for various particle sizes. Fig. 2.3 (c)-(h) show SEM pictures of disordered samples, T57, T20, and T60. Since the sample has a glass substrate, transmission spectra are readily measurable. All

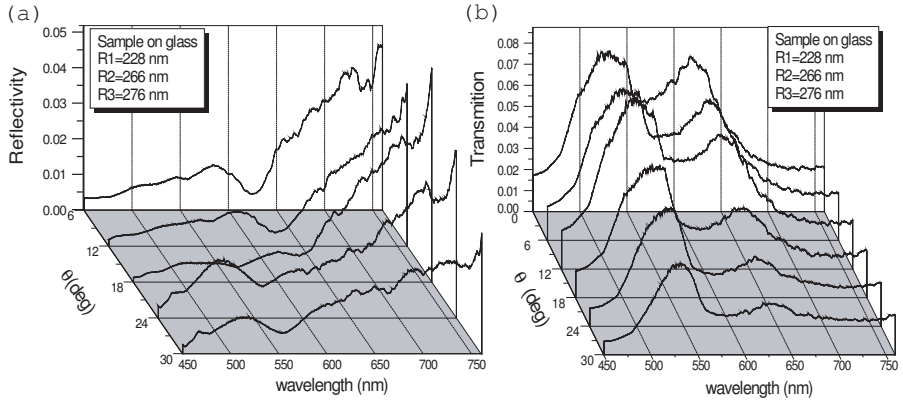

Figure 2.13: Angle dependent linear reflection (a) and transmission (b) spectra of disordered sample T57 on glass.

experiments were again carried out at room temperature, and all reflection and transmission spectra of each sample were measured at one point on the sample surface.

2.5.1 Particle T57

Fig. 2.13 shows the linear spectra of a disordered T57 sample (R_1=228 nm, R_2=266 nm, and R_3=276 nm). Fig. 2.13(a) shows the reflection spectra at various incident angles and Fig. 2.13(b) the transmission spectra. In reflection, the disordered sample gives a similar spectrum as the ordered one (see Fig. 2.8). The peaks and dips also exhibit the same angular dependence. From the SEM picture of Fig. 2.3 (c) and (d), we can identify small groups containing 5 to 10 close-packed particles. As discussed above, they act as tiny local crystallites and lead to an angular dependence of the spectra. From the SEM picture, the thickness of the sample can be estimated to be about 3-5 layers of particles.

A small dip appears at 670 nm with no angle dependence, which very well coincides with the internal quadrupole plasmon resonance in the gold shell cavity predicted by calculation both in a single-particle and multi-layer model. The transmission spectrum is shown in Fig. 2.13(b). It is remarkable that a 'transparency window' appears from 500 nm to 650 nm with two

peaks, at 530 nm and 620 nm, respectively, and a dip at 570 nm. All have angle-independent positions, while their intensity decreases with increasing angle.

The transmission, points to plasmon coupling between the particles and excitation of plasmon waves along chains of particles. When the incoming light has a wavelength close to the particle size, it is strongly coupled into surface plasmons, which rapidly transfer between particles as a plasmon wave, penetrate deeply into the sample, coupling out again as photons at the surface of both side of sample. If the sample is not thicker than the damping distance, transmission can be expected. Only a wavelength coinciding with the plasmon resonance and in regions of the crystal with strong inter-particle coupling, will be transmitted. In our experiment, we observed transmission peaks at 530 nm and 620 nm. Recalling the discussion of the diffraction spectrum of the *ordered* sample in section 2.4, we found that the diffracted light spectrum mainly resides in the short wavelength range, which is consistent with the present transmission result. Comparing this with the calculation of multi-layer ordered sample, they correspond to resonances of the inner part of the gold shell. The dip at 570 nm originates from the absorption peak of dipole plasmon resonance of the outer part of the gold shell. For wavelength longer than 670 nm, the quadruple plasmon resonance prevails, which is only weakly coupled to nearest particles, can not penetrate into the sample, and therefore is absorbed if not reflected specularly by the sample.

2.5.2 Particle T20

Now we examine changes in the spectra for particles with other geometrical parameters R_1=205 nm, R_2=255 nm. We recall that these T20 particles do not have the silica cap layer. As a result the gold shells may touch and change the plasmon resonance and couplings considerably. Unfortunately, we have no calculated results available for this type of particle.

Fig. 2.14 displays the measured spectra of the disordered sample T20 on a glass substrate, for various incident angles. Fig. 2.14(a) shows the reflectivity and (b) the transmission at the same point. It is remarkable that both reflection and transmission spectra are similar to those of sample T57, but show blue shift. The reflection dip at 550 nm exhibits no angle dependence. Therefore we consider it as the outer surface dipole plasmon resonance absorption of single particles. Since in sample T20, R_2=255 nm is very close to the outer shell size of sample T57, R_2=276 nm, it is not

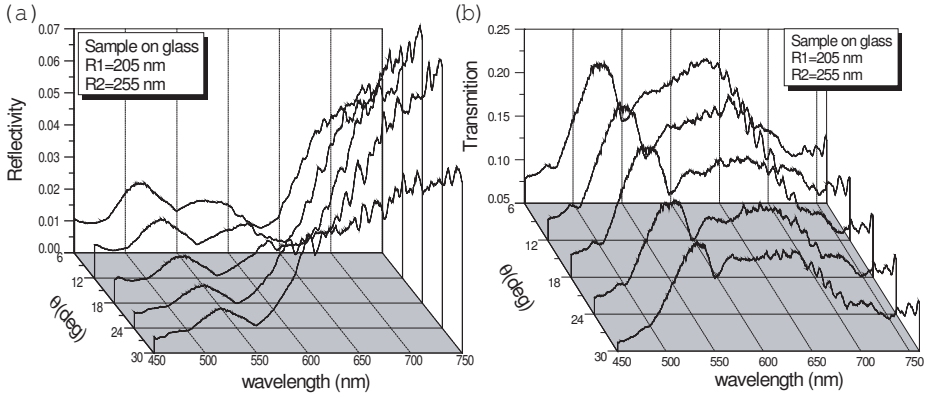

Figure 2.14: Angle dependent linear reflection (a) and transmission (b) spectra of disordered sample T20 on glass.

surprising that the resonance is close to the calculated dip at 560 nm of sample T57. The dip at 633 nm does exhibit an angle dependence on the intensity, but not on position. It shows a similar feature as the dip at 670 nm of sample T57, but shifted to the blue. We consider it as the quadrupole plasmon resonance of the gold shell.

In the measured transmission spectra of Fig. 2.14(b), a similar transmission window appears from 500 nm to 700 nm. It has two peaks at 525 nm, 630 nm and two dips in between, at 550 nm and 585 nm, respectively. The dip at 550 nm is angle independent. Compare this with the absorption dip at 570 nm in the T57 sample, we think this dip corresponds to the dipole resonance absorption of single particles, but shifted a bit to blue for this smaller particle T20. The small dip at 585 nm coincides with the reflection peak at that wavelength. The transmitted peak at 525 nm is close to the position of the reflection peak at 515 nm, we think it is the plasmon excited by incoming light that penetrates the structure via inter-particle coupling, and radiates out as light at both sides.

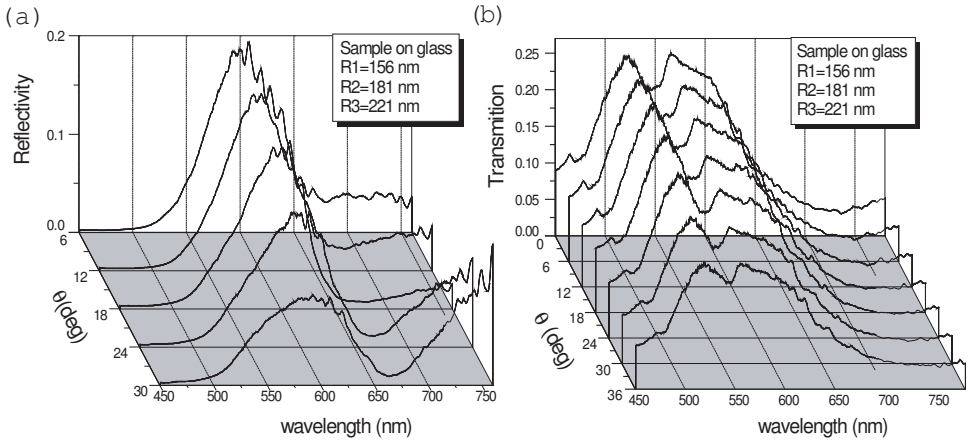

Figure 2.15: Angle dependent linear reflection (a) and transmission (b) spectra of disordered sample T60 on glass.

2.5.3 Particle T60

Fig. 2.15 displays the measured results of T60 particles on a glass substrate, with R_1=156 nm, R_2=181 nm, and R_3=221 nm. For this sample, the spectra are completely different. The multi-peak structure in the visible light range disappears, and only one big peak shows up at 595 nm which has an angle-dependent peak position, and shifts from 590 to 600 nm. For large angles, a second peak emerges around 750 nm. These peaks might be a result of the extinction dips (590 nm, and 750 nm) of this particle, which has been calculated by J. Penninkhof [54].

Again, a transmission window from 500 nm to 630 nm appears in this sample, as shown in Fig. 2.15(b). The dip at 545 nm corresponds to the plasmon resonance absorption.

2.6 Conclusions

In this chapter we examined the linear optical properties in the visible range of silica-core gold-shell particles, both in ordered and disordered arrays, in reflection and transmission. The observed linear reflection spectra show a very complex multi-peak structure, which can be favorably compared with the KKR calculations and identified as surface plasmons and delocalization

effects in a periodic 3-D fcc-ordered photonic crystals. We classified the plasmon resonances, single particle contributions, and photonic contributions in the spectrum. From 500 nm to 650 nm clear diffraction patterns are observed which are sensitive to crystallite size and their organization in space. These correspond to Fraunhofer diffraction of a collection of small crystallites. It is remarkable that a transmission window in the visible light range can be detected from 500 nm to 650 nm in disordered samples, which is depending on particle size. Considering the thickness of the sample, at least three layers of particles and integrated more than 100-nm thickness of gold, the transmission is remarkably higher than that of a continuous gold layer, in which visible light only penetrates about 10 nm. We explain this by plasmon generation and conduction and subsequent conversion at the sample surface to light. In addition, some special points were discovered on the ordered sample, which give giant reflectivity at the plasmon resonance peak.

Knowledge of the linear optical properties has prepared us to measure the nonlinear transient response, which is the subject of the next chapters.

Chapter 3

Ultrafast pump-probe experimental setups

Abstract In this chapter we describe two types of ultrafast pump-probe experimental setups relying on femtosecond lasers at different repetition rates. One is a standard pump-probe setup with a mechanical delay line and a lock-in amplifier for data acquisition. The other is a so-called Asynchronous Optical Sampling (ASOPS) setup operating at high repetition rate that needs no scanning mechanical delay line.

3.1 Introduction

In a measurement of the ultrafast dynamics of the optical properties of materials on the femtosecond time scale one has to deal with two issues: the optical pulse length and the time resolution of detectors. By mode locking and pulse compression techniques, laser pulses can be shortened down to a few femtoseconds. However, no electronic devices can reach that high speed and femtosecond time resolution. Therefore, the so-called pump-probe method is developed for ultrafast optical measurements. It makes use of two short laser pulses, one, normally very intense, acts as pump and followed by the other, a weak pulse, as probe. The pump pulse excites the material and

changes its optical properties. The probe pulse monitors the induced changes of the material upon traversing the pumped zone. By controlling the time delay between pump and probe pulses, high time resolution can be achieved up to femtosecond scale with a slow light detector.

There are two difficulties in applying the optical ultrafast pump-probe technique, one is time delay control, the other is the detection of weak signals. Motor controlled mechanical translation stages are widely used in pump-probe setups to set the time delay. The pump and probe pulses are split from an incoming pulse train generated by a femtosecond laser, and fly through different light paths. One of them is delayed by a mechanical translation stage to achieve adjustable and stable time control. The time resolution is limited by the width of pulses and the accuracy of the translation stage, which can both reach the femotosecond time scale. Recently, asynchronous optical sampling has been demonstrated using two synchronized mode-locked lasers, with fixed different repetition rates serving as pump and probe, respectively. This enables ultrafast time-domain spectroscopy without any mechanical delay line. In an optical pump-probe experiment, the temporal effects are normally very small. The amplitude of the signal is very weak and may often be less than the background noise level. Therefore, phase-sensitive and frequency-sensitive techniques are used to extract the signal and reject spurious noise signals.

In this chapter, we describe two ultrafast pump-probe experimental setups used in this thesis based on femtosecond lasers of different repetition rates. One is a standard pump-probe setup with 1-kHz repetition rate designed with a mechanical delay line and a lock-in amplifier for data acquisition and built in Utrecht. The other is an Asynchronous Optical Sampling (ASOPS) setup for high repetition rates built in the University of Konstanz [62].

3.2 Pump-probe setup with 1-kHz repetition rate

A pump-probe setup was designed to examine both the stationary reflection spectrum in the visible light range and transient changes of the reflectivity induced by an ultrashort optical excitation at 800 nm. In our experiments on strongly scattering samples consisting of colloidal particles, the sensitivity of the setup can reach 10^{-4}. A temporal delay window of 2 ns and a resolution of 1 ps were realized.

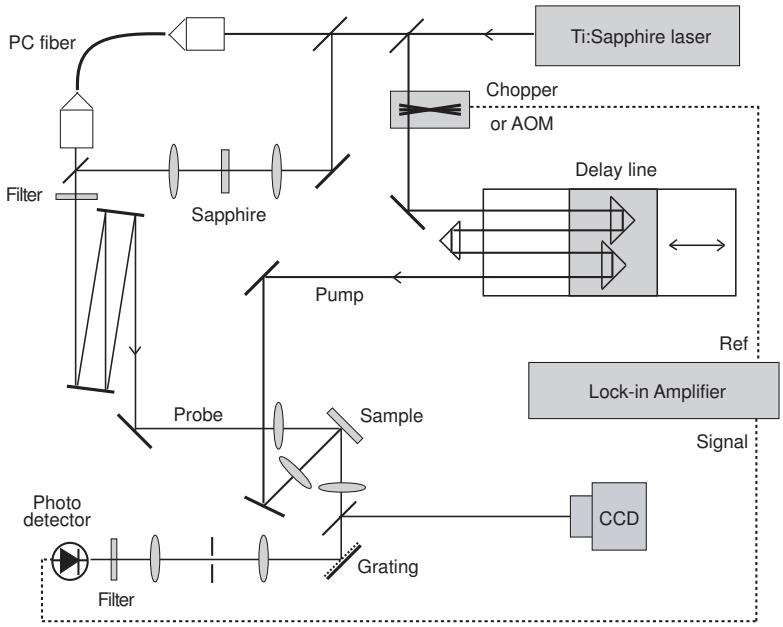

Figure 3.1: Sketch of the 1-kHz pump-probe setup.

3.2.1 Description of the setup

Fig. 3.1, shows a sketch of our 1-kHz pump-probe setup. It employs an amplified Ti-sapphire laser delivering 800-nm, 120-fs pulses, operating 0.5 mJ/pulse at a repetition rate of 1 kHz. By a beam splitter, the laser beam is split into two. The pump beam passes an optical delay line and is focused down to a 100-μm spot at the sample surface. The pump fluence on the sample surface can be controlled by an attenuator to obtain a fluence in the range of 0.1-10mJ/cm^2 per pulse. In order to achieve a large band width of the probe spectrum, the probe beam is focused on a sapphire slab or alternatively coupled into a photonic-crystal fiber to generate continuum white light. Subsequently, the white light beam was collimated and focused onto a 30-μm spot at the sample surface into the pumped zone. The reflected and scattered probe light from the sample was collected and collimated by a lens with a 0.2-rad opening angle, the so-called signal beam. The signal beam was dispersed by a grating and a bandwidth of 20-nm 'single color' light was selected and detected by a photodiode. The transient reflectivity can be

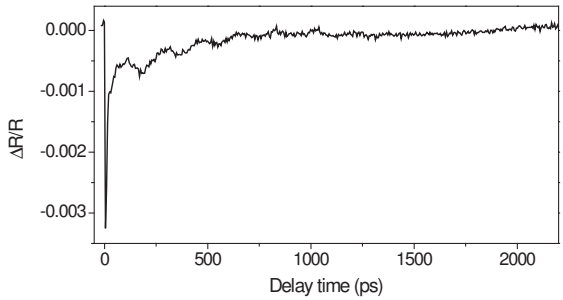

Figure 3.2: A typical experimental trace of transient reflectivity measured by 1-kHz pump-probe setup on disordered T60 sample. Probe at 560 nm, and pump at 800 nm, 4 mJ/cm^2.

measured by moving the mechanical translation stage with 10-μm precision. As shown in Fig. 3.1, the pump beam were turned over twice by two retro reflectors mounted on the optical delay line. As a result we achieve a 2.4-ns temporal measurement window with step sizes as small as 150 fs. The time resolution of the setup is determined by several factors: the precision of the delay line, the pulse duration of pump and probe, and the stability of the setup. The time resolution is limited by the probe pulse duration. During white-light generation, the probe pulses become chirped to a ∼3-ps pulse from 750 nm to 450 nm. Within 20-nm 'single color', however, the probe has a subpicosecond duration. Therefore, the time resolution of the setup can be estimated to be better than 1 ps.

By putting a beam splitter in the signal beam, the diffraction pattern can be recorded by a charge-coupled device (CCD). The linear spectrum can be measured inserting a spectrometer (Action Research, SpectraPro 300I) with a spectral resolution of 1 nm and equipped with a cooled CCD (Roper Scientific, model CCD-1340-EB/1).

In a pump-probe experiment, we used a lock-in amplifier to detect the weak signal from the photodiode. The pump light at 1-kHz repetition frequency was modulated by a mechanical chopper at 250 Hz. A low-frequency lock-in amplifier (Princeton Applied Research Model-5209) was used to detect the signal from the photodiode with reference frequency from the chopper (250 Hz). The data acquisition and the controlling of devices, including the CCD, the lock-in amplifier, and the delay line, were controlled by a computer

operating in a Labview environment [63].

Fig. 3.2 shows a typical experimental trace of the transient reflectivity measured by our 1-kHz pump-probe setup on a disordered T60 gold-shell sample. The signal exhibits a rapid drop in reflectivity of 3.3×10^{-3} due to the optical electronic response. Subsequently, a modulation of the reflectivity can be clearly distinguished with an amplitude of $\sim 3 \times 10^{-4}$ caused by acoustic vibration of particles. The noise level can be as small as $\sim 5 \times 10^{-5}$ without any software averaging.

3.2.2 Lock-In technique

Lock-In techniques are useful to detect very small AC signals, even when the small signal is obscured by noise sources many thousands of times larger [64]. It uses phase sensitive detection to extract a modulated component of the signal at a specified reference frequency and phase. Noise signals at frequencies other than the reference frequency are largely rejected. Suppose the reference signal is a square wave at frequency ω_R and is synchronous with the pump in the experiment. The response signal will contain $V_S \sin(\omega_R t+\theta_S)$ where V_S is the signal amplitude and θ_S the phase.

The lock-in amplifier multiplies the signal by the reference $V_R \sin(\omega_R t + \theta_R)$ using a mixer to obtain the output

$$\begin{aligned} V_1 &= V_S \sin(\omega_R t + \theta_S) V_R \sin(\omega_R t + \theta_R) && (3.1)\\ &= 1/2 V_S V_R \cos(\theta_R - \theta_S) + 1/2 V_S V_R \sin(2\omega_R t + \theta_R + \theta_S)\ . && (3.2) \end{aligned}$$

Since the two inputs to the mixer are at exactly the same frequency, the first term in the mixer output is a DC signal. The second term is at a frequency of $2\omega_R$ which is at a high frequency and is removed by a low pass filter. Therefore the output becomes

$$V_{1+filter} = 1/2 V_S V_R \cos(\theta_R - \theta_S)\ , \qquad (3.3)$$

which is proportional to the cosine of the phase difference between the input and the reference. Hence the term phase sensitive detection.

On the other hand, a second mixer is used with the reference input 90° out of phase, $V_R \sin(\omega_R t + \theta_R - \pi/2)$. The output of the second mixer is

$$\begin{aligned} V_2 &= 1/2 V_S V_R \cos(\theta_R - \theta_S - \pi/2) \\ &\quad + 1/2 V_S V_R \sin(2\omega_R t + \theta_R + \theta_S - \pi/2)\ . && (3.4) \end{aligned}$$

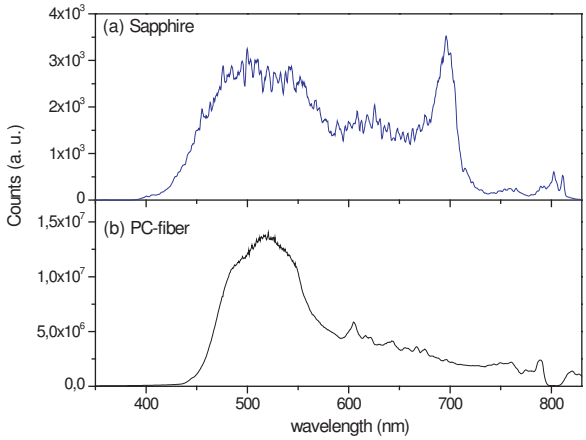

Figure 3.3: White light spectra generated by (a) sapphire plate and (b) photonic crystal fiber of 10 cm length, pumped with 800-nm 100-fs laser pulse.

After low pass filtering

$$\begin{aligned} V_{2+filter} &= 1/2 V_S V_R \cos(\theta_R - \theta_S - \pi/2) \\ &= 1/2 V_S V_R \sin(\theta_R - \theta_S) \ . \end{aligned} \tag{3.5}$$

Therefore, the amplitude of the input signal can be computed by

$$\mid V_S \mid \ = \ (2/V_R) \times \sqrt{V_{1+filter}^2 + V_{2+filter}^2} \ . \tag{3.6}$$

3.2.3 White light generation

In order to obtain a large band width of the probe spectrum, the probe beam is focused on a sapphire plate or alternatively coupled into a photonic crystal fiber to generate continuum white light via self-phase modulation. When an intense optical pulse enters a medium, the nonlinear change of the refractive index caused by the optical pulse itself changes its phase during propagation, and results in a spectral broadening.

In our experiment, we focus 100-fs, 800-nm pump light of 28 μJ/pulse by a 15-cm focal distance lens onto a 4-mm thick sapphire slab. Fig. 3.3 (a) shows the spectrum of the white light generated by the sapphire plate, ranging from 430 nm to 730 nm. An alternative method is using a photonic-crystal fiber (PC fiber) to generate white light [90][91]. Fig. 3.3 shows the

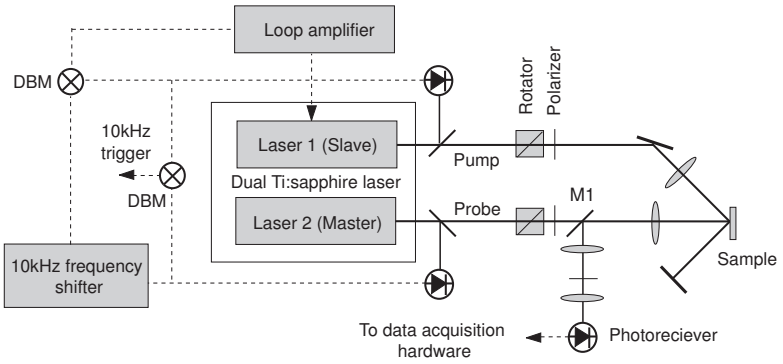

Figure 3.4: Sketch of the ASOPS setup. Solid lines are optical paths, dashed lines present electronic connection.

white light spectrum of a 10-cm PC fiber generated by coupling 0.2-μJ/pulse laser beam into the core of fiber by an objective of NA=40. The PC fiber contains a 1.7μm silica core surrounded by a photonic crystal structure. In this case, the white light spectrum ranges from 450 nm to 750 nm and peaks at 520 nm.

The white light generation broadens the bandwidth of the probe spectrum, and allows us to detect the optical response of our sample in the visible light range. Because of the dispersion of the sapphire (or silica), the duration of white light pulse is chirped to ∼5 ps, and leads to a time resolution of ∼1 ps for a 20-nm band width probe.

3.3 Asynchronous optical sampling (ASOPS)

The second setup is a pump-probe scheme with a low excitation fluence but with high repetition rate employing asynchronous optical sampling (ASOPS). This technique enables ultrafast time-domain spectroscopy without a mechanical delay line, and is developed in the University of Konstanz [62].

Fig. 3.4 shows a sketch of the ASOPS setup. It is a technique relying on two mode-locked Ti:Sapphire lasers at repetition rates of f_R =1 GHz, with a pulse duration of approximately 30 fs. The repetition frequency of laser 1 is detected by a photodiode and subsequently shifted by a frequency shifter with $\triangle f_R$=10 kHz. Using a double-balanced mixer (DBM) as a phase detector, the frequency-shifted repetition rate is fed back to a piezoelectric transducer that

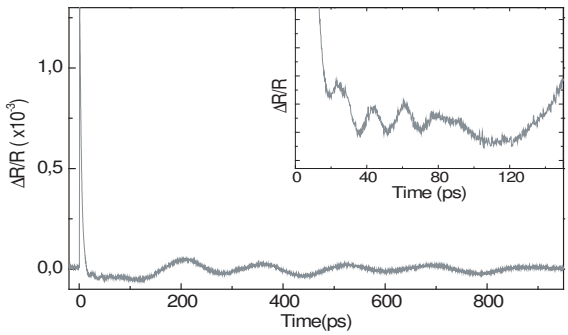

Figure 3.5: A typical experimental trace of transient reflectivity measured by ASOPS setup on disordered T60 sample. Probe at 780 nm, and pump at 830 nm, 40 μJ/cm^2. Inset shows a zoom in at short time scale.

supports a cavity mirror in laser 2 via a loop amplifier. Therefore, the two lasers are locked at a fixed difference repetition rate $\triangle f_R$=10 kHz. They serve as pump and probe lasers, respectively. As a result their relative time delay is continuously ramped between zero and $1/f_R$, which gives a 1-ns temporal measurement window with femotosecond time resolution. The pump and probe beams are focused down to 50-μm spots on the sample surface, overlap in space, with incident angle of $\theta = 45^\circ$ and $\theta \sim 0^\circ$. Pump and probe beams can be interchanged. With a rotator and a polarizer inserted in the pump and probe beam, the polarization and power can be freely adjusted. The pump fluence is variable in the range of $5 - 20\mu$J/cm^2. The wavelength of the two mode-locked Ti:Sapphire lasers can be independently tuned from 750 nm to 850 nm. The reflected probe beam is collected by the same focusing lens, reflected by a mirror (M1), and detected by a photoreciever. The signal is converted by an analog-to-digital converter in a PCI board and recorded by a computer, triggered by the synchronization electronics. Therefore, thousands of experimental traces can be acquired in a few minutes, and changes of the reflectivity as small as 10^{-7} can be detected after signal averaging.

Fig. 3.5 shows a typical experimental trace of transient reflectivity measured by ASOPS setup on a disordered T60 gold-shell sample. A slow modulation of the reflectivity can be detected with an amplitude of $\sim 4 \times 10^{-5}$, and a fast oscillation is clearly observed with an amplitude of $\sim 1.2 \times 10^{-5}$. The noise level can be as small as $\sim 3 \times 10^{-6}$.

Chapter 4

Ultrafast transient reflectivity of gold-shell photonic crystal

Abstract In this chapter, we examine the ultrafast transient response of a 3-D photonic crystal of silica-core gold-shell colloidal particles following femtosecond optical excitation. We analyze the decay time and the shape of the response as they depend on both the probe wavelength and pump pulse intensity. The transient reflectivity spectrum strongly varies, which can be accounted for by a pump-induced broadening of the plasmon resonance of the gold-shell particles. The observed dynamics is analyzed in the framework of the so-called "two-temperature model". From the observed pump power dependence, an electron-phonon coupling constant of 1.0×10^{16} W/(m^3K) is deduced. The electron gas temperature is estimated to reach ∼1800 K by fitting the experimental results.

4.1 Introduction

The electronic response of metals on a sub-picosecond scale have been studied in metal films [23] and ensembles of metallic nanoparticles [24] in recent decades. It was established that ultrafast reflectivity signals induced by femtosecond optical excitation are caused by rapid heating of the electron gas in the metal. The heated electron gas affects both the real and the imaginary part of the dielectric constant of the metal and causes a wavelength-dependent transient change in both the reflection and absorption spectra of the metal.

Dielectric spheres coated with metallic shells give a promise for non-linear optics [76][77][78] because the metallic shell possesses plasmon resonances that may enhance the local electric field [54]. It was proposed that intense optical excitation may shift the spectral position of the plasmon resonance [78]. Subpicosecond non-linear responses from metallic nanoshells were demonstrated for the first time by Averitt and co-wokers [79] for particles composed of a 40-nm Au_2S core surrounded by an ultra-thin Au layer. In addition, it has been established that the spectral position of the plasmon resonance in metallic nanoshells depends on the core-shell ratio of radii that makes their optical properties controllable by choosing suitable geometrical parameters [76][80].

In chapter 2, we have analyzed the linear optical properties of a dense packing of submicron gold-shell particles. The close-packed organization of particles forms a 3-D photonic crystal and shows a complex spectral structure in the visible light range, largely governed by plasmon resonances. This makes the structure promising for enhancing the nonlinear optical response. In this chapter, we examine the ultrafast nonlinear response of the ordered 3-D photonic crystal gold-shell sample by femtosecond optical excitation and compare the transient reflectivity spectrum with the calculations. The decay of the electronic response signal appears to depend on the pump intensity and is analyzed by the two-temperature model.

4.2 Nature of the ultrafast dynamics in gold

Before starting the investigation of ultrafast nonlinear optical properties in gold-shell particles, we need to identify what processes are induced by the pump pulse. There are two types of materials present in our gold-shell parti-

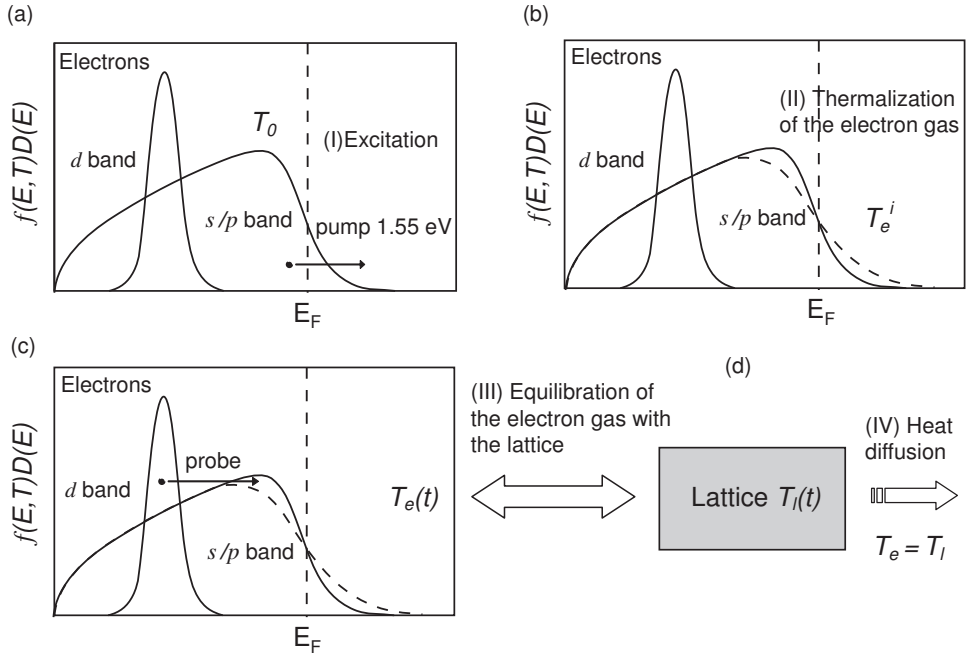

Figure 4.1: Schematic view of the ultrafast dynamics in gold. E_F is the Fermi energy and $f(E,T)D(E)$ is a number density, i.e. Fermi-Dirac distribution multiplied by the density of the states. 5d and 6s are the electron bands of Au.

cles: silica and gold, of which only gold can absorb the pump light at 800 nm. The conduction electrons in the metal are excited by the laser pump pulse (100 fs), and decay in a few picoseconds [32], which is too fast to deform the particle. Therefore, the dynamical changes of the optical properties are commonly governed by the transient modulation of the dielectric constant of the free electron gas by ultrashort optical pulses [69]. At later times, the lattice is starting to play a role, leading to elasto-optic contributions to the dielectric constant. To model the full dynamics one commonly resorts to a four-step- process. In Fig. 4.1, we show the schematics of the four steps for the case of gold.

(I) Excitation

Initially, the electron gas is in thermal equilibrium and has a Fermi-Dirac distribution. Fig. 4.1(a) schematically shows the electron number density of gold [81], $f(E,T)D(E)$. Here, $f(E,T)$ is the Fermi-Dirac distribution $f(E,T) = 1/\big(\exp((E-E_F)/kT)-1\big)$ with Fermi energy E_F, and $D(E)$ the density of the states. When the pump pulse arrives, part of the energy is absorbed by electrons creating hot electrons: the electrons reach a non-Fermi-Dirac distribution of some hot electrons and leaving the main part cold [70]. In our particular case, the photon energy of the pump light ($\hbar\omega$=1.5 eV) is below the plasma frequency of gold, below the interband transition threshold of the *d*-band to the Fermi level (2.47 eV [27]), and below the minimum *d*-*p* transition (∼2.3 eV [82]). The photons predominantly excite electrons in the *s*/*p*-band via intraband transition, within the duration of pump pulse (100 fs), too fast to be resolved in our experiments.

(II) Thermalization of the electron gas

As shown by the dashed line in Fig. 4.1(b), the hot electrons rapidly equilibrate with the remaining free electrons [70] and rebuilt a Fermi-Dirac distribution well within the first picosecond. This changes the occupation numbers of the electronic states near the Fermi level and the deviation of the dielectric constant from equilibrium will reach its maximum value. Of course, the thermalized hot electron gas has gained a higher temperature T_e^i, which may be far from equilibrium with the "cold" lattice.

(III) Equilibration of the electron gas with the lattice

This process is shown in Fig. 4.1(c), where the hot free electron gas looses its energy to the lattice via electron-phonon interaction which is determined by the electron-phonon coupling constant, G_{e-p}. During this process, the electron temperature $T_e(t)$ decreases leading to a recovery of the electronic dielectric constant to the equilibrium value, the temperature of the lattice T_e, $T_l > T_0$ (ambient temperature).

(IV) Heat diffusion

Finally, the lattice in equilibrium with the electrons ($T_e = T_l$) cools down via heat transfer to the surrounding temperature bath (see Fig. 4.1(d)). In

this process, the lattice temperature equilibrates to the ambient temperature. The rate of this process depends on the size of the excited volume, and the heat conductivity of the sample. Typically it is in nanosecond range and thus much slower than the former steps.

4.3 Observation of ultrafast response

4.3.1 Experimental details

The experiments are focused on the photonic crystal sample T57 grown on a flat silicon substrate. The particles consist of a 228-nm radius silica core, a 38-nm thickness gold shell, and an 10-nm thickness outer silica shell. The SEM picture of the sample is shown in Ch. 2, Fig. 2.4 (a) and (b). A detailed description of the linear optical properties of the sample can also be found in Ch. 2.

The ultrafast response of the photonic crystal sample was examined by the 1-kHz repetition-rate pump probe setup shown in Fig. 3.1 of Ch. 3. The incident angle of the probe beam is 45° and the pump-beam direction is perpendicular to the sample surface. The transient changes of the probe reflectivity were measured from a thick highly ordered part of the photonic crystal. The studied sample areas were carefully selected by checking that the diffraction pattern coincides reasonably well with the diffraction pattern shown in Fig. 2.8 that should correspond to a thick ordered part of the sample. The reflected probe light was dispersed by a grating followed by a pinhole to select a 20-nm band width, and subsequently detected by a photodiode. The intensity of the pump beam can be adjusted from 0.16 mJ/cm^2 to 8 mJ/cm^2 by changing the attenuators in the beam. Under these illumination intensities, no degradation takes place and the dynamics of the transient reflectivity spectra appeared to remain stable and reproducible for at least several hours.

The probe signal detected by the photodiode is read out by a lock-in amplifier. When the optical delay line is tuned to zero delay between pump and probe ($t = 0$), the lock-in amplifier gives a signal that measures the nonlinear response. For each selected point on the sample surface, probe wavelength, and pump power, we have maximized the spatial overlap of pump and probe beam by maximizing the nonlinear signal. The pump power was measured with a power meter in front of calibrated attenuators that serve to

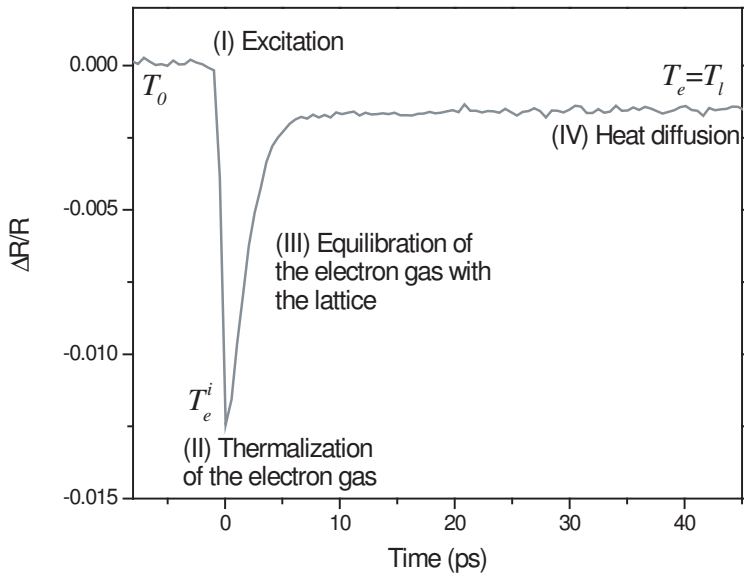

Figure 4.2: Transient reflectivity signal of a gold-shell photonic crystal at 560 nm. Pump fluence is 1.21 mJ/cm^2 laser pulse at 800nm.

determine the pump fluence on the sample. The selected wavelength of the probe light is gauged by a spectrometer.

4.3.2 Ultrafast response

Fig. 5.10 shows a typical ultrafast response signal of the transient reflectivity of the gold-shell photonic crystal at 560-nm probe wavelength following 800-nm excitation. The pump fluence is 1.21 mJ/cm^2 per pulse. The pump pulse arrives at $t = 0$. The transient reflectivity $\triangle R/R$ falls within 1 ps, corresponding to the excitation of hot electrons (process I). The measured reaction time is limited by the temporal resolution of the setup, i. c. the chirp of the probe. Within this time, the excited electrons equilibrate with each other and attain a Fermi-Dirac distribution at a high electron temperature (process II). Here the amplitude of change in the dielectric constant reaches its maximum value and leads to the largest $\triangle R/R$ detected. Subsequently the heated electrons equilibrate with the lattice (process III). Therefore the amplitude of $\triangle R/R$ rapidly decays in a few picoseconds, and reaches a level

corresponding to an equilibrated temperature of electrons and lattice ($T_e = T_l$). Finally, the reflectivity slowly recovers by heat diffusion (process IV) on a nanosecond time scale, which is out of the temporal window of our present experiment.

4.4 Electron temperature dependence of the optical properties of gold

The dielectric constant of gold $\varepsilon = \varepsilon' + i\varepsilon''$ induced by a temperature rise of the electron gas can be calculated by considering the interband transition and intraband (Drude) contribution of the free electrons.

$$\varepsilon = \varepsilon_{IB} + \varepsilon_D \tag{4.1}$$

For the intraband contribution ε_D we consider a free electron gas in gold and calculate the dielectric constant using the Drude model [26]. The imaginary part and real part are given by

$$\varepsilon''_D(\omega) = \frac{\omega_p^2 \tau(T_e)}{\omega(1+\omega^2\tau(T_e)^2)} \text{ and} \tag{4.2}$$

$$\varepsilon'_D(\omega) = 1 - \varepsilon''_D(\omega)\omega^2\tau(T_e)^2 \ , \tag{4.3}$$

respectively, with ω_p the plasma frequency ($\sim$8.3 eV for gold), and $\tau(T_e)$ the collision time of free electrons in gold.

For metals such as gold where interband transitions occur in the same spectral region as the plasmon band, this contribution appears to be the most important part for inducing changes in surface plasmon resonances with electron temperature [83][36]. The imaginary part of the dielectric constant due to the interband absorption was found to be [74][80]

$$\varepsilon''_{IB}(\omega, T_e) = \frac{8\pi^2 e^2 \hbar^2}{3m_0^2\omega^2} |M_{p-d}|^2 \int D(E,\omega)[1 - f(E,T_e)]dE, \tag{4.4}$$

where m_0 is the free electron mass, e the charge of the electron, ω the frequency of light M_{p-d} the transition matrix element. $D(E,\omega)$ is the so-called energy-distributed joint density of states given by

$$D(E,\omega) \propto \frac{\Theta\big[v_d\hbar\big(\omega - \omega_{d-p}\big) - E\big]}{\sqrt{v_d\hbar\big(\omega - \omega_{d-p}\big) - E}}. \tag{4.5}$$

Here Θ is the Heaviside step function and $v_d = m_p/(m_p + m_d)$, with m_p and m_d the effective masses for the p and d bands, respectively [74]. For gold $\hbar\omega_{d-p} = 2.38$ eV and $v_d = 0.86$.

The real part of the dielectric constant can be obtained from the Kramers-Krönig relations [84]

$$\varepsilon'_{IB}(\omega, T_e) = \frac{2}{\pi}\mathcal{P}\int_0^\infty \frac{\omega'\varepsilon''_{IB}(\omega', T_e)}{\omega'^2 - \omega^2}d\omega', \tag{4.6}$$

where $\mathcal{P}$ denotes the Cauchy principal value of the integral.

The change in the dielectric constant of gold for an electron temperature rise from T_0 (293 K) to T_e, due to the inter- and intraband contributions was calculated by O. L. Muskens. The experimental dielectric constants of gold at room temperature is displayed in Ch.1, Fig. 1.1 and was used for the calculation [20]. Fig. 4.3 (a) shows the calculated imaginary and real part of the dielectric constant of gold from the UV to the visible light range for T_e =293 K up to 3200K. Fig. 4.3 (b) displays the deviation of the dielectric constant from the value of T_0, $\triangle\varepsilon = \varepsilon(T_e) - \varepsilon(T_0)$, vs. wavelength for this range of T_e. The amplitude of reflectivity of a flat gold surface can be calculated from the dielectric constant by $R = |(n-1)/(n+1)|$, where the n is the complex refractive index and $n = \sqrt{\varepsilon}$ [72], and is shown in Fig. 4.3(c). The relative deviation of the reflectivity $\triangle R/R$ vs. wavelength is displayed in Fig. 4.3 (d) for T_e varied from 293 K to 3200 K. We observe a positive change around 500 nm and an abrupt switch to negative values at 600 nm.

Further, the $\triangle R/R$ at selected wavelengths can now be plotted vs. T_e. In Fig. 4.3 (d) we indicate straight lines at 560 nm, 600 nm, 640 nm, and 700 nm, in the negative peak around 600 nm, and for these plotted in Fig. 4.3 (e) $\triangle R/R$ vs. T_e. We note that our calculation gives the same result as the work of J. Hohlfeld [27].

The electron temperature T_e is not measured directly in a pump-probe experiment. However, one still can relate the pump fluence P to the electron temperature. When a pump pulse hits the gold surface, the absorbed energy E_{absorb} is determined by the absorbance and is proportional to the pump fluence P. The heated electron gas temperature T_e^i can be calculated from the electronic heat capacity $C_e = 1/3\pi^2 D_f k_B^2 T_e = \gamma T_e$, where k_B is the Boltzmann constant, D_f the electronic density of states at the Fermi level [72]. Since $P \propto E_{absorb} = V \times \gamma/2((T_e^i)^2 - T_0^2)$, $T_e^i \propto \sqrt{P}$, where V is the excited volume of gold. In Fig. 4.3 (f) we plot $\triangle R/R$ vs. $(T_e^i)^2 - T_0^2$ for T_e^i

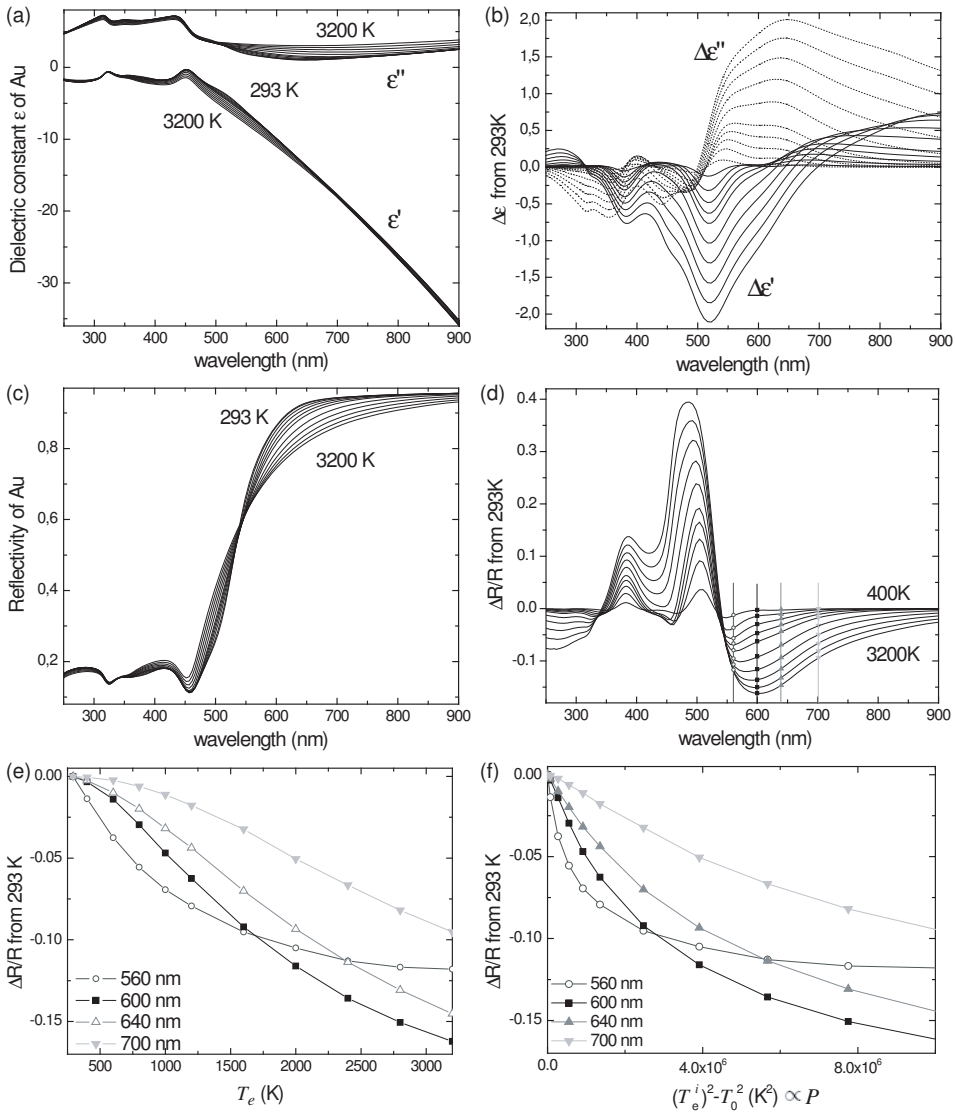

Figure 4.3: (a) Calculated dielectric constant ε of gold vs. wavelength for T_e varying from 293 K up to 3200 K [20]. (b) shows the deviation of the dielectric constant $\triangle\varepsilon$ vs. wavelength from room temperature T_e =293 K. (c) Calculated reflectivity spectra of gold and (d) deviation of reflectivity spectrum $\triangle R$ from T_e =293 K up to 3200K. (e) and (f) $\triangle R/R$ for selected wavelengths (560 nm, 600 nm, 640 nm, and 700nm) vs. T_e and vs. $(T_e^i)^2 - T_0^2 \propto P$ (pump fluence), respectively.

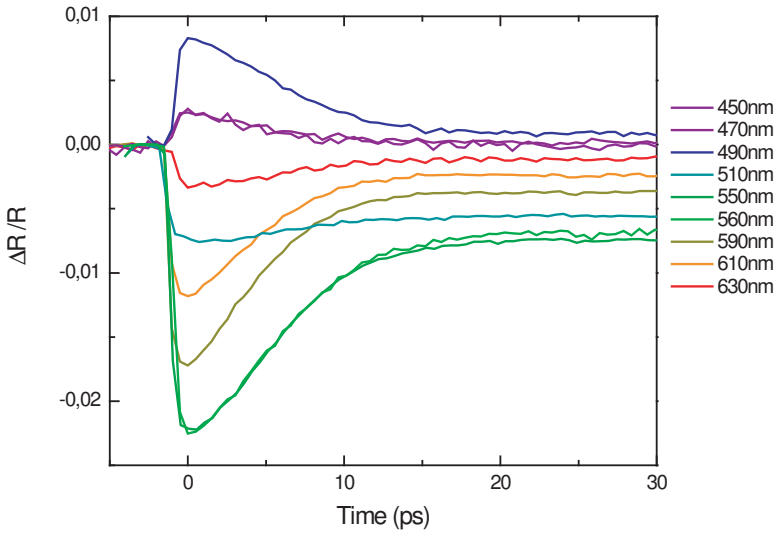

Figure 4.4: Transient reflectivity at different wavelength from 450 nm to 630 nm measured on one sample point with pump intensity of 4.2 mJ/cm^2.

from 293 K up to 3200 K, which is to be compared in the next section with the measured $\triangle R/R$ vs. pump pulse intensity.

4.5 Probe wavelength dependence of ultrafast response

We have measured the electronic response following a pump pulse vs. probe wavelength. Fig. 4.4 shows the transient reflectivity measured at one sample point vs. probe wavelength. We see in Fig. 4.5 (a) that the electronic response, defined as the peak height for a zero time delay, $\triangle R/R(t = 0)$ changes amplitude and sign vs. probe wavelength. We measured two sample points, one with pump of 4.2 mJ/cm^2 (solid triangles) and one with 3.8 mJ/cm^2 (open squares), vs. the probe wavelength. We note that both points give similar features. The electronic response shows a positive peak at 490 nm, rapidly drops to negative values, reaches the largest negative signal at 560 nm, and finally slowly recovers from 560 nm to 750 nm.

It is remarkable that the measured electronic response vs. probe wave-

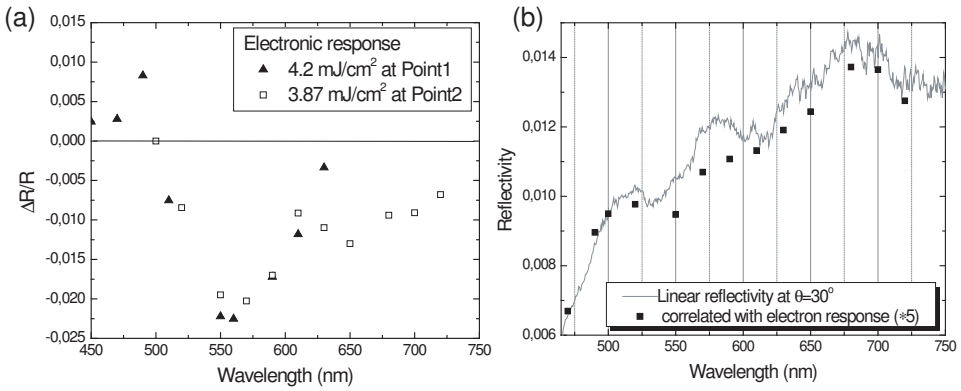

Figure 4.5: (a) Signal amplitude of electronic response $\triangle R/R$ depending on the probe wavelength measured on two sample points, at 4.2 mJ/cm^2 (solid triangles) and 3.8 mJ/cm^2 (blank squares) pump pulse, respectively. (b) Linear reflectivity spectrum of the gold-shell photonic crystal sample at incident angle $\theta = 30°$ (solid line), and corresponding spectrum with electron response (full squares).

length shows similar feature as the calculated $\triangle R/R$ for bulk gold in the previous section (see Fig. 4.3(d)), but shifted 40 nm to the blue. In case of bulk gold, Fig. 4.3(d), the crossing point $\triangle R/R = 0$ is located at 540 nm, while the photonic crystal shows a crossing at 500 nm. We argue that the electronic response in the gold-shell photonic crystal is determined by gold since it is the only material containing free electron gas in the sample. However it is shifted by the photonic structure, in which surface plasmons and the periodic lattice lead to a multi-peak spectrum in the visible light range, that strongly deviates from that of bulk gold.

In the measured linear reflectivity of a gold-shell photonic crystal, the transient reflectivity electronic response is inserted, for comparison in Fig. 4.5 (b). Here, we present a linear reflectivity spectrum of our gold-shell photonic crystal sample at an incident angle $\theta = 30°$ (gray line), and indicate the transient reflectivity contribution of the hot electrons. For reasons of presentation, the electronic response is magnified by a factor of 5. From Fig. 4.5 (b), some broadening of the peak at 500 nm can be identified. Since the peak at 500 nm can be classified as the plasmon resonance delocalized by the periodic lattice (see Ch. 2), we think that the ultrafast change of the dielectric constant of gold, broadens the peak.

The measured negative electronic response around 560 nm in Fig. 4.5 (a)

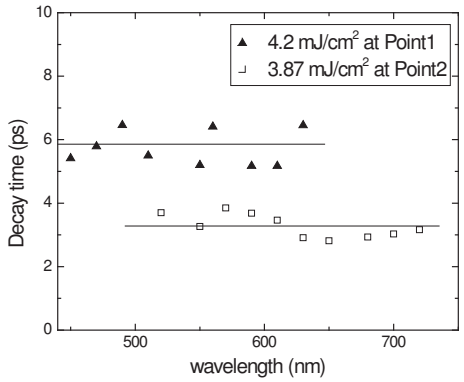

Figure 4.6: Fitted exponential decay time of the two sample points, with pump 4.2 mJ/cm^2 (solid triangles) and 3.8 mJ/cm^2 (open squares), respectively.

can be traced back to the multiple-scattering of photons in the photonic crystal. When the electron gas is heated by the pump pulse, it causes an increase of the imaginary part of the dielectric constant of gold, which will lead to larger absorbance and shorter integrated light paths in the sample. Therefore the band-gap contribution typical for a periodic lattice, will decrease and cause less reflectivity, i.e. a negative sign in $\triangle R/R$. If we recall the discussion in Ch. 2, the band gap of the sample is supposed to extend from 500 nm to 650 nm, exactly in the range where the negative signal appears in the ultrafast experiment.

The decay time of the electronic response can be quantified by fitting the measured results by an exponential decay function $\triangle R/R = A + B\exp(-t/\tau)$. In Fig. 4.6, the fitted decay times are plotted against probe wavelength. We note that at each experimental point pumped with a constant fluence, the decay time roughly keeps constant, and the decay time depends on pump intensity. It signifies that the decay time is not determined by the probe wavelength, but is governed by the pump intensity, i.e. on the temperature of the hot electron gas.

4.6 Two-temperature model

The cooling of the heated electron gas and the thermalization with the lattice, can be described by the two-temperature model [36][23]. This model assumes

that both electrons and phonons are in internal thermal equilibrium but not in mutual equilibrium. In this case, these subsystems can be characterized by an electron temperature T_e and a lattice temperature T_l, respectively. The relaxation dynamics of these temperatures follows form the heat exchange equation,

$$C_e \frac{\partial T_e}{\partial t} = \bigtriangledown \cdot (\kappa \bigtriangledown T_e) - G_{e-p}(T_e - T_l) + h(r,t) \quad (4.7)$$

$$C_l \frac{\partial T_l}{\partial t} = -G_{e-p}(T_l - T_e), \quad (4.8)$$

where $C_e = 1/3\pi^2 D_f k_B^2 T_e = \gamma T_e$ [72] and C_l are the electronic and lattice heat capacities, respectively, and G_{e-p} represents the electron-phonon coupling constant. Further, κ is the thermal conductivity of the electrons, k_B the Boltzmann constant, D_f the electronic density of states at the Fermi level, and $h(r,t)$ the electron heating source term. Since the duration of the pump pulse is much shorter than the electron-phonon interaction, $h(r,t)$ can readily be considered as a δ-function. For gold γ=67 $\mathrm{Jm^{-3}K^{-2}}$, C_l=2.5×10^6 $\mathrm{Jm^{-3}K^{-1}}$ [71][73][74].

The two-temperature model assumes that electron-electron thermalization occurs on a much faster time scale than equilibration with the lattice which indeed is the case at high degrees of excitation $\triangle T_e > T_e$. In our experiment the excitation is variable from 20 $\mu\mathrm{J/cm^2}$ to just below the damage threshold $\sim$ 10 $\mathrm{mJ/cm^2}$ and the two-temperature model is quite suitable for our case. Further, we assume that hot electrons, by virtue of their high Fermi velocities tend to quickly spatially homogenize the hot electron distribution over the shell and omit the diffusion term in Eq. (4.7). We arrive now at two coupled non-linear differential equations,

$$\gamma T_e \frac{\partial T_e}{\partial t} = -G_{e-p}(T_e - T_l) \text{ and} \quad (4.9)$$

$$C_l \frac{\partial T_l}{\partial t} = -G_{e-p}(T_l - T_e). \quad (4.10)$$

When the temperature change in the electron gas is small (i.e., at low pump power), $\triangle T_e \ll T_0$, where T_0 is the initial temperature and $\triangle T_e$ the temperature increase induced by the pump laser, the relaxation is uni-exponential with a decay time $\tau = \gamma T_0 / G_{e-p}$. As long as $\triangle T_e \gg T_l$, the decay is a linear-function of t, $T_e(t) = T_e^i - (G_{e-p}/\gamma)t$.

The final equilibrium temperature, T_∞, can be calculated from the energy balance between the electron gas and the lattice. In case of $\triangle T_e \gg T_\infty$,

$$T_\infty - T_0 = \frac{\gamma}{2C_l}\big(\triangle T_e^i\big)^2, \tag{4.11}$$

where T_0 is the temperature of the electron gas and the lattice before the excitation ($t < 0$), and $\triangle T_e^i$ is the initial temperature increase of the electron gas from T_0 after excitation.

In order to solve Eq. (4.9), we neglect the small variation of T_l compared with the large variation of T_e, ($\partial T_l/\partial t \ll \partial T_e/\partial t$), because $C_e \ll C_l$. Therefore Eq. (4.11) can be omitted. Assuming in the approximation $T_l \approx T_\infty$, Eq. (4.9) is simplified to

$$\gamma T_e \frac{\partial T_e}{\partial t} = -G_{e-p}(T_e - T_\infty). \tag{4.12}$$

The solution of this equation is

$$T_e(t) = T_\infty W\left[\chi \exp\left(\chi - \frac{G_{e-p}}{\gamma T_\infty} t\right)\right] + T_\infty, \tag{4.13}$$

where $W(t)$ is the Lambert function and $\chi = ((T_e^i) - T_\infty)/T_\infty$.

4.7 Power dependent measurements of ultrafast response

In our experiments, we study the cooling of the hot electron gas by recording the ultrafast response of the gold-shell photonic crystal vs. incident fluence. We keep the probe wavelength fixed to 560 nm, at which wavelength we obtain the largest signal. In Fig.4.7 (a), we show the measured transient reflectivity at 560 nm for pump fluences from 0.16 mJ/cm^2 up to 7.22 mJ/cm^2. All scans were carried out at a same sample point. We notice in Fig. 4.7(b) that the amplitude of $\mid \triangle R/R \mid$ linearly increases with the pump fluence.

The absorbed energy E_{absorb} is proportional to the pump fluence P, and the absorption of the gold-shell photonic crystal sample. Therefore, P is proportional with $(T_e^i)^2 - T_0^2$, described in Sect. 4.4, where T_e^i is the initial electron temperature induced by the pump pulse and T_0 is the ambient temperature. Since gold is the only material containing free electron gas in the gold-shell particles, the ultrafast transient reflectivity is ultimately due

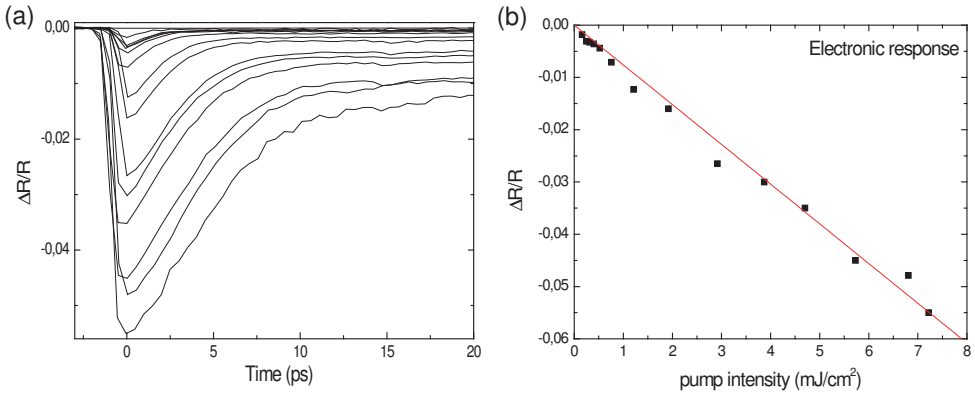

Figure 4.7: (a) Measured transient reflectivity at 560 nm with different pump intensity. (b) The electronic signal magnitude $\triangle R/R$ versus the pump intensity.

to transient change of the dielectric constant of gold caused by the pump pulses. Therefore, we expect that the ultrafast transient reflectivity of our sample should show similar features as bulk gold vs. electron temperature. In the calculated result of bulk gold of $\triangle R/R$ vs. $(T_e^i)^2 - T_0^2$, shown in Fig. 4.3 (f), we observe an approximately linear curve dependence for 600 nm at T_e <1800 K. From this, we estimate the high-temperature limit in our experiment to be 1800 K. We choose to compare a wavelength of 600 nm for bulk gold with a wavelength of 560-nm probe in the experiment on our photonic crystal, because both are located on top of the negative electronic response (see Fig. 4.5 (b) and Fig. 4.3 (d)).

The decay of the transient reflectivity $\triangle R/R$ can now be simulated by the cooling process of the electron gas in the two-temperature model in the range for T_e from 300 up to 1800 K. In the two-temperature model, the electron temperature is calculated vs. time, $T_e(t)$, that we can connect to $\triangle R(t)$. Since we found a linear relation between the transient reflectivity and pump fluence, $\triangle R/R \propto P$, and we know $P \propto (T_e^i)^2 - T_0^2$, we can conclude that during the cooling process, the measured transient reflectivity $\triangle R(t)/R$ is proportional with $T_e(t)^2 - T_0^2$, therefore

$$\triangle R(t)/R \quad \propto \quad T_e(t)^2 \ . \tag{4.14}$$

In Fig.4.8, we plot the normalized measured transient reflectivity at 560 nm (black lines) and the calculation of $T_e(t)^2$ of two-temperature model with

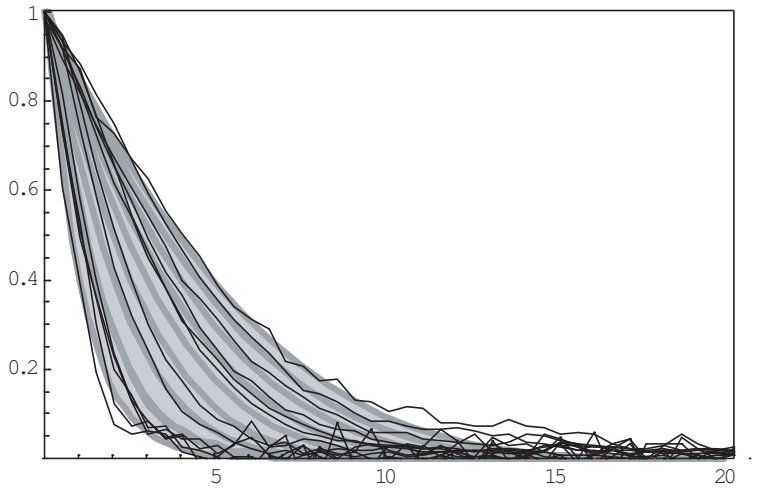

Figure 4.8: Normalized measured transient reflectivity at 560 nm (black lines) and the normalized calculation of $T_e(t)^2$ of two-temperature model with initial temperature varying of T_e^i (gray thick curves) from 20 K to 1800 K.

initial temperature rise (gray thick curves) for temperatures varying from 20 K to 1800 K. It is satisfying that the measured result is well accounted for by the bandwidth of the calculation for the temperature range we deduced. A electron-phonon coupling constant of $G_{e-p} = (1.0 \pm 0.1) \times 10^{16}$ W/m^3K was found in the calculation, which is smaller than the reported bulk gold value ($G_{e-p} = 2.95 \times 10^{16}$ W/(m^3K)) by Groeneveld et al. [74], and a $G_{e-p} = 2.2 \times 10^{16}$ W/(m^3K) by Averitt and his coworkers for Au-shell/Au_2S-core particles in tens of nanometer size [79]. In other studies on the ultrafast dynamics of gold films in the last decades, the electron-phonon coupling constant was found to vary in the range of $1 \sim 4 \times 10^{16}$ W/(m^3K), depending on the thickness of the gold film and fabrication methods used [27].

At this point we analyze the power dependence of the non-uniexponential electron cooling in the two-temperature model by two different methods, i.e. (i) the decay rate directly after the excitation pulse, and (ii) the fitted exponential decay rate.

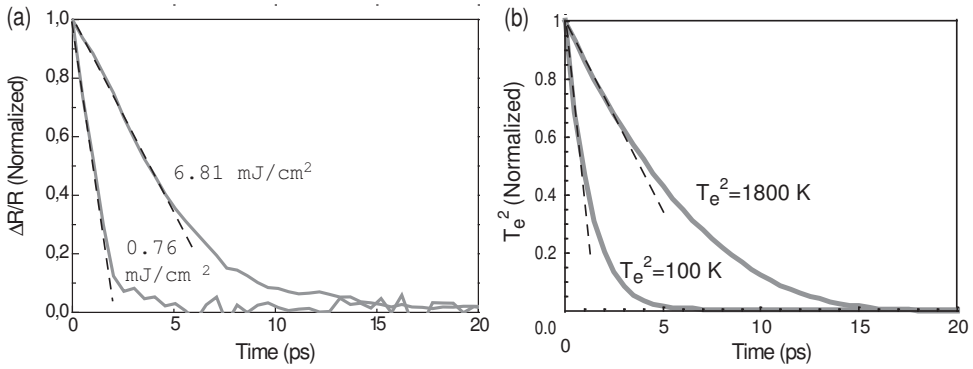

Figure 4.9: Fitting by linear decay. (a) is experimental results (gray lines) fitting with linear decay (dashed line), measured with pump intensity of 0.76 mJ/cm^2 and 6.8 mJ/cm^2, respectively. (b) is calculated results of two-temperature model (gray curves) fitting with linear decay (dashed curves), with initial change of electron temperature of 100 K and 1800 K, respectively.

(i) Initial decay rate

Fig. 4.9 (a) displays the fitting result for the measurements at a pump intensity of 0.76 mJ/cm^2 and 6.8 mJ/cm^2, as examples, and Fig. 4.9 (b) shows the fitting for the calculated curves of the two-temperature model with for an initial change of electron temperature of 100 K and 1800 K, respectively. We determine the initial slope (ps^{-1}) for all the measured results, and compared those with the partial derivative of the calculated traces of the two-temperature model $\partial T_e(t)^2/\partial t$ at a certain given initial electron temperature T_e^i. Fig. 4.10 shows the result. Here we have again taken $\triangle T_e^i \propto \sqrt{P}$ to make the direct comparison between experiment and theory possible.

In Fig. 4.10, the data (dots) nicely correlate with the calculation when the partial derivative of $\partial T_e(t)^2/\partial t$ is taken at t=0.6 ps instead of t=0. This is reasonable because the time resolution of the setup is ∼0.6 ps (see Ch. 2) and equally broadens the width of the electronic response peak. From Fig. 4.10, a highest increase of electron temperature $\triangle T_e^i = 1870$ K can be deduced, which nicely coincides with the upper limit that we obtained from the analysis of $\triangle R/R$ vs. P.

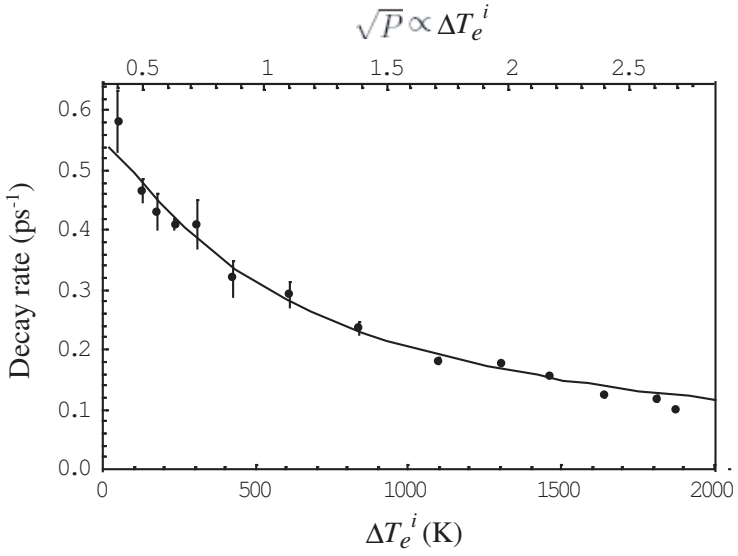

Figure 4.10: Partial derivative $\partial T_e(t)^2/\partial t$ at t=0.6 ps vs. initial change of electron temperature $\triangle T_e^i$ (black curve), and the measured initial slope of experimental traces vs. $\sqrt{P}$ (data dots).

(ii) Exponential decay

Alternatively, we approximate $\triangle R(t)$ by an exponential decay, which allows us to define a 'characteristic' cooling time for the electrons. The decay time of electrons can be estimated by fitting the normalized experimental results by an exponential decay

$$\left(\frac{\triangle R}{R}\right)_{normalized} = \exp(-t/\tau) \tag{4.15}$$

Fig. 4.11 (a) shows some examples of the exponential decay fit of the measurements at 0.76-mJ/cm^2 and 6.8-mJ/cm^2 pump intensity, respectively. Fig. 4.11 (b) shows the fitting of calculated curves for an initial electron temperature rise of 100 K and 1800 K. At low pump power and low electron temperature, they can be nicely fitted by a single-exponential decay. For high pump power (up to 6.8 mJ/cm^2) and high initial electron temperatures (i.e. 1800 K), a small deviation is seen both in the measurement and the calculation. Therefore we suspect that the decay time fitted from single-exponential decay is still comparable in high temperature situation.

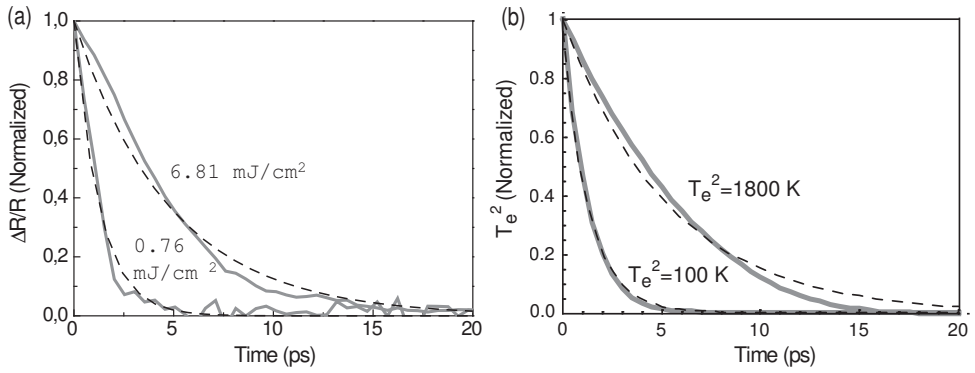

Figure 4.11: Fits by exponential decay. (a) gray lines experimental results, dashed curves fits with exponential decay, measured with pump intensity of 0.76 mJ/cm^2 and 6.8 mJ/cm^2, respectively. (b) is calculated results of two-temperature model (full curves) fitting with exponential decay (dashed curves), with initial electron temperature of 100 K and 1800 K, respectively.

Fig. 4.12 displays the comparison of the fitted decay times of experimental and calculated results. The exponential decay time of the calculated results shows a linear relation vs. the initial increase of electron temperature $\triangle T_e^i$, plotted as the black line in Fig. 4.12. Again, the fit results are plotted as data dots in Fig. 4.12 vs. $\sqrt{P}$, and reasonably correlates with the calculated times vs. T_e^i. A highest electron temperature increase of $\triangle T_e^i = 1700$ K is found by this method, which is in reasonable accord with the 1850-K temperature deduced by the former method.

The electron temperature rise due to optical excitation can also be estimated by the optical absorption of gold, which is ∼5% for 800-nm wavelength pump. If we consider a 38-nm thick gold film, which is equal to the thickness of the gold-shell, a temperature rise of ∼1400 K can be calculated for 7.2-mJ/cm^2 pump fluence, smaller than the ∼1800 K we find from our photonic crystal. This suggests a higher absorption of pump light for the photonic crystal than for the gold film. This can be caused by the plasmon resonance absorption and multiple scattering. In case of the gold film, the absorption of 800-nm pump is mainly due to the excitation of the 6s-band electrons via the intraband contribution. In case of the gold-shell photonic crystal, the size of the submicron particles and the periodic ordering permit novel plasmon resonances in the visible light range, which may increase the absorption.

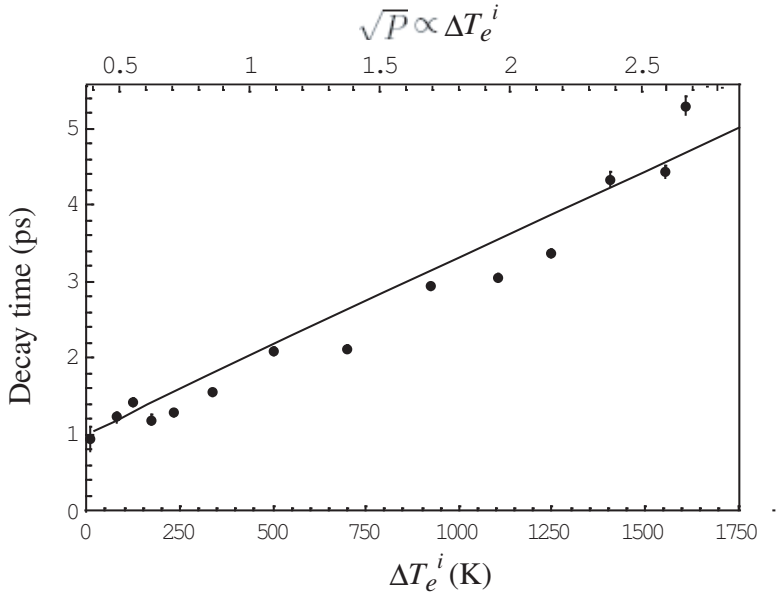

Figure 4.12: Fitted decay time for experimental results (data dots) versus $\sqrt{P}$ (P pump power), and calculated decay time vs. initial change of electron temperature $\triangle T_e^i$ (black curve).

4.8 Conclusion

In this chapter, we analyzed the ultrafast nonlinear response of the transient reflectivity of an ordered 3-D photonic crystal gold-shell sample following excitation of a 800-nm, 120-fs laser pulse. The transient reflectivity spectrum of bulk gold is calculated by a dielectric constant deviation induced by an increase of the electron temperature. In the photonic crystal the hot electron effect has a 40-nm shift of the maximum transient reflectivity signal from the bulk gold value. This is related to the plasmon resonance of the gold-shell particles and the translational symmetry of the sample. In the band-gap region from 500 nm to 650 nm, the transient reflectivity decreases, which is consistent with an increased damping of the light during the multiple scattering processes in the presence of a hot electron gas.

The recovery of the reflectivity has been studied by pump-power dependent measurements. The observed dynamics can be consistently accounted for in the framework of the "two-temperature model". An electron-phonon

coupling constant of $(1.0 \pm 0.1) \times 10^{16}$ W/(m^3K) is deduced for colloidal gold-shell particles. The electron gas temperature reached, is determined to be as high as ∼1800 K. This temperature is higher than the calculated temperature of a gold film excited by similar fluence because the plasmon in the photonic crystal leads to increased absorption.

Chapter 5

Acoustic vibrations of spherical submicron gold-shells

Abstract In this chapter, we demonstrate and discuss the acoustic vibrations in submicron spherical gold-shell particles. The vibrational mode frequencies can be calculated by a two-shell model developed on basis of Lamb's theory. By employing pump-probe experiments, we excite the acoustic vibrations of the gold-shells and detect via modulations of the optical reflectivity. Spherical breathing modes and thickness modes of vibrations were identified in a 3-D ordered array of the particles. For a disordered array, elliptical modes were excited and observed. Finally, we demonstrate a dependence of the vibrational period on the gold-shell size.

5.1 Introduction

In the previous chapter, the dynamic response of silica-core gold-shell photonic crystal has been analyzed during the first tens of picoseconds following femtosecond excitation. The changes of the dielectric constant of gold in-

duced by hot electrons govern the transient reflectivity on a picosecond time scale. These hot electrons thermalize with the lattice within 10 ps and all energy initially deposited into the particles by laser excitation ends up in the lattice. The rapid heating of the lattice causes an impulsive thermal stress in the metal and expansion which results in the coherent excitation of acoustic vibrations.

Recently, vibrations of nanosized metallic structures generated by absorption of ultrashort laser pulses have attracted much interest. The confinement of electrons and phonons causes the physical properties of nanometer-sized objects to intrinsically depart from those of bulk solids [53]. One of the ambitions of nanoscience is to exploit such deviations to tailor novel properties of nanoparticles through their sizes and shapes. Therefore, Raman scattering experiments [28] [29] [30] and pump-probe spectroscopy [31] [32] have been undertaken in nanosized metallic structures to analyze phonons both in the frequency-domain and the time-domain, respectively.

The breathing vibrational mode of solid metallic particles with a diameter from a few nanometers to tens of nanometers, has been demonstrated in silver [31], gold [33][34], and gallium [34]. Other types of vibrational modes (i.e. second harmonic of the fundamental breathing modes, non-spherically symmetric modes) were found in single nanoparticle experiments with 45-nm diameter gold particles [35]. In most of these experiments, the measured frequency of coherently excited breathing vibrations was in a good agreement with the calculated values. Further, silver ellipsoids [16], gold nanorods [34], gold triangles [38], and bimetallic core-shell particles [26][30] were used to demonstrate a shape-dependence of vibrational frequencies. The first detection of coherent breathing vibrational mode of nanometer-thick gold shells around a 250-nm radius SiO_2 core arranged in a photonic crystal, was performed by D. Mazurenko et al. [36]. Here the particle was treated as a hollow sphere leading to a good agreement with Lamb theory calculation and measurements [37]. Acoustic vibrations of 10-nm size Au nanoshells around a Au_2S-core were analyzed later in a liquid [86]. Similar breathing mode of the shell and a size dependence were demonstrated.

In this chapter, we analyze the acoustic vibrational modes in spherical gold-shell particles. Depending on the sample and measuring technique, we excite and detect different modes in a particle, and discuss the dependences on size and ordering of the particles.

5.2 Theory

Acoustic or vibrational modes of spheres or spherical shells are described by classical mechanics. By solving the wave equations with proper boundary conditions, eigen modes can be identified and their vibrational frequencies determined. In 1882, Lamb analyzed the acoustic vibrations of a free elastic sphere and also a free-standing thin hollow sphere for the first time [67]. He found explicit analytical solutions for the eigen functions. In this section, we calculate the eigen modes of a free gold-shell particle based on Lamb theory [37], and extend the calculation to the case of a free two-shell model with a phenomenological interface boundary condition [68].

5.2.1 Lamb theory

The wave equation for elastic and isotropic media has the form [87]

$$\frac{\partial^2 \mathbf{u}}{\partial t^2} = (c_l^2 - c_t^2)\nabla(\nabla \cdot \mathbf{u}) + c_t^2 \nabla^2 \mathbf{u} \ , \tag{5.1}$$

where t is time and $\mathbf{u}$ the lattice displacement. Further c_l and c_t are the longitudinal and transverse sound velocities, respectively. For periodic oscillations $\mathbf{u} \sim \exp(-i\Omega t)$, where Ω is the angular frequency, Eq. (5.1) reduces to

$$(c_l^2 - c_t^2)\nabla(\nabla \cdot \mathbf{u}) + c_t^2 \nabla^2 \mathbf{u} + \Omega^2 \mathbf{u} = 0 \ . \tag{5.2}$$

For spherically symmetric particles, the solution of Eq. (5.2) can be expressed in spherical coordinates (r, θ, φ).

$$\begin{aligned} u_r &= \frac{\partial \Upsilon_{lm}(h_l r)}{\partial r} + \left\{ \frac{\partial^2 [r\Upsilon_{lm}(h_t r)]}{\partial^2 r} - r\nabla^2 \Upsilon_{lm}(h_t r) \right\} , \\ u_\theta &= \frac{1}{r}\frac{\partial \Upsilon_{lm}(h_l r)}{\partial \theta} + \frac{1}{\sin\theta}\frac{\partial \Upsilon_{lm}(h_t r)}{\partial \varphi} + \frac{l}{r}\frac{\partial^2 [r\Upsilon_{lm}(h_t r)]}{\partial r \partial \theta} \ , \\ u_\varphi &= \frac{1}{r\sin\theta}\frac{\partial \Upsilon_{lm}(h_l r)}{\partial \varphi} + \frac{\partial \Upsilon_{lm}(h_t r)}{\partial \theta} + \frac{l}{r\sin\theta}\frac{\partial^2 [r\Upsilon_{lm}(h_t r)]}{\partial r \partial \varphi} \ . \end{aligned} \tag{5.3}$$

Here, u_r, u_θ and u_φ are the radial and the angular displacements, respectively, $h_l = \Omega/c_l$, $h_t = \Omega/c_t$, and Υ_{lm} is the spherical distribution function,

$$\begin{aligned} \Upsilon_{lm}(kr) = \left(A_l \sqrt{\frac{\pi}{2kr}} J_{l+1/2}(kr) + B_l \sqrt{\frac{\pi}{2kr}} Y_{l+1/2}(kr) \right) \\ \times P_{lm}(\cos\theta) e^{im\varphi - i\Omega t}, \end{aligned} \tag{5.4}$$

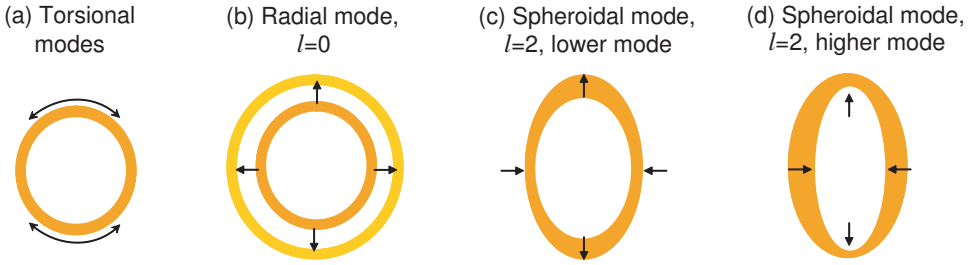

Figure 5.1: Sketch of vibrational modes of a hollow spherical shell.

A_l and B_l are constants to be determined from the boundary conditions, $J_n(kr)$ and $Y_n(kr)$ are the n-th order Bessel functions of the first and the second kind, respectively, and $P_{lm}(\cos\theta)$ is the Legendre function with the angular numbers l and m. We note that n and m are integers and $-l \leq m \leq l$. For $l = 0$ modes, displacements are purely radial.

By applying the boundary condition at the interfaces for radial displacements u_r and radial components of the stress tensor σ_{rr} [99]

$$\sigma_{rr} = \rho\Big[c_l^2 \frac{\partial u}{\partial r} + (c_l^2 - 2c_t^2)\frac{2u}{r}\Big], \tag{5.5}$$

the eigenfrequencies and normalized displacements can be computed for a solid sphere and hollow sphere [88].

If we consider a spherical shell with internal and external radii, R_1 and R_2, respectively, the eigenfrequencies can be obtained by applying free boundary conditions at both sides of the shell. Lamb found the eigenfrequencies in case of a very thin shell, $(R_2 - R_1) \ll R_{1,2} \approx R_s$.

The motion of a spherical shell was analyzed by D. Mazurenko [37]. The modes can be divided into two classes, namely torsional and spheroidal ones. In Fig. 5.1 we sketch the vibrational modes of a shell. The torsional modes are fully tangential (see Fig. 5.1 (a)) and rise in frequency with increasing angular number l. The eigenfrequencies of torsional modes are given by the expression

$$\Omega_l = c_t R_s^{-1}\sqrt{(l-1)(l+2)}, \tag{5.6}$$

We notice that the lowest mode appears for $l = 2$.

The solutions for spheroidal modes are different for the cases $l = 0$ and $l > 0$. In case of $l = 0$, the fundamental eigen mode is a purely radial mode

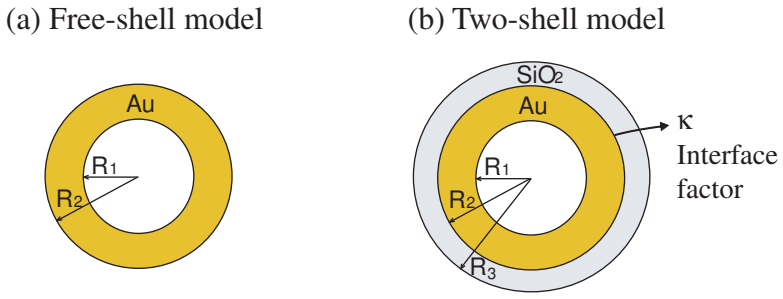

Figure 5.2: Two-shell model and factor κ dependence.

as shown in Fig. 5.1 (b), so called "breathing" mode. The frequency of the breathing mode is

$$\Omega_0 = 2c_t R_s^{-1}\sqrt{\xi}, \tag{5.7}$$

where $\xi = 3 - 2(c_t/c_l)^2$.

In case of $l \geq 1$ the motion of the shell have both radial and transverse components. For each l, these modes have two branches with frequencies given by

$$\Omega_{l\pm} = c_t R_s^{-1}\sqrt{\frac{\varsigma}{2} \pm \frac{1}{2}\sqrt{\varsigma^2 - 16\xi(l^2+l-2)}}\,, \tag{5.8}$$

where $\varsigma = (l^2+l+4)\xi + l^2 + l - 2$. For $l = 1$ the high frequency root of Eq. (5.8) is $c_t R_s^{-1}\sqrt{6\xi}$ while the lower one is zero, corresponding to a pure translation of the shell. For $l \geq 2$ both branches have a non-trivial solution. Fig. 5.1 (c) and (d) show the motions of the lower and higher modes of $l = 2$. Here, elongation or contraction at the equator or the pole take place, and the motions resemble "elliptical" modes. In hollow spherical shells, the calculation shows that the lowest vibrational mode of the shell is the lower $l = 2$ mode.

5.2.2 Two-shell model

Until now we considered a single free shell. However, in case of our gold-shell particle, the particle consists of a silica core, a gold shell, and a silica cap shell. We assume that the contact between the core and the gold shell to be negligible, because upon drying the core shrinks about 5% [17] and the gold shell does not. Therefore, we extend the theory to a "two-shell" model. Fig. 5.2 shows the sketch pertinent for the free-shell model (a) and for the

two-shell model (b), where a silica shell capping the gold shell is added. The radii of the three spherical interfaces are R_1, R_2, and R_3, respectively. Instead of a solid connection at the interface, we introduce a phenomenological 'interface factor κ', which may range from 1 to infinite. This factor κ describes the degree of contact at the interface between gold and silica. The radial displacements at the two sides of the interface, $u_{r,Au}$ and u_{r,SiO_2} are connected as

$$\begin{cases} u_{r,Au} = \kappa u_{r,SiO_2} & \text{if driven from the gold side,} \\ u_{r,SiO_2} = \kappa u_{r,Au} & \text{if driven from the silica side.} \end{cases} \tag{5.9}$$

The interface factor κ operates as an variable attenuator of displacement from the gold to the silica side and vice versa. As described in Ch. 2, the gold-shell particles were fabricated in a liquid and subsequently dried on a substrate. The polymer connection between gold and silica shell may partly loose by drying and create a new and unknown boundary condition. The interface factor κ, is the factor quantifying this boundary condition. In case of $\kappa = 1$, the gold and silica are well connected and give an identical displacement at the interface. In case of $\kappa \to \infty$, the gold and silica are independent free shells without any connection. When $\kappa > 1$, the side, which is driven by the optical pump, takes more amplitude than the other side.

In the two-shell model, we only take into account the outer silica shell and neglect the presence of the inner silica core. If we consider the process of exciting acoustic vibrations in the particle by an ultrafast laser pulse, the gold absorbs energy and is rapidly heated, leading to expansion. Since the thermal expansion coefficient of gold is much larger than that of silica, the contact between gold and the inner core is bound to be weak, apart from the already mentioned shrinkage of silica in drying process. Therefore, we expect the two-shell model to be a reasonable model for our situation.

5.2.3 Calculation results

By taking a free boundary condition of the inner and outer surface of the two-shell particle, eigenfrequencies can be calculated numerically for a given κ. Further, the displacement along the radii u_r can be calculated by Eq. (5.3) with the eigenmodes. The computer program for these numerical calculation were written by X. Zhang [68]. In the calculations, we used the longitudinal and transverse sound velocities for gold of $c_l = 3240m/s$ and $c_t = 1200m/s$, respectively, and for silica $c_l = 5970m/s$ and $c_t = 3760m/s$, respectively [37].

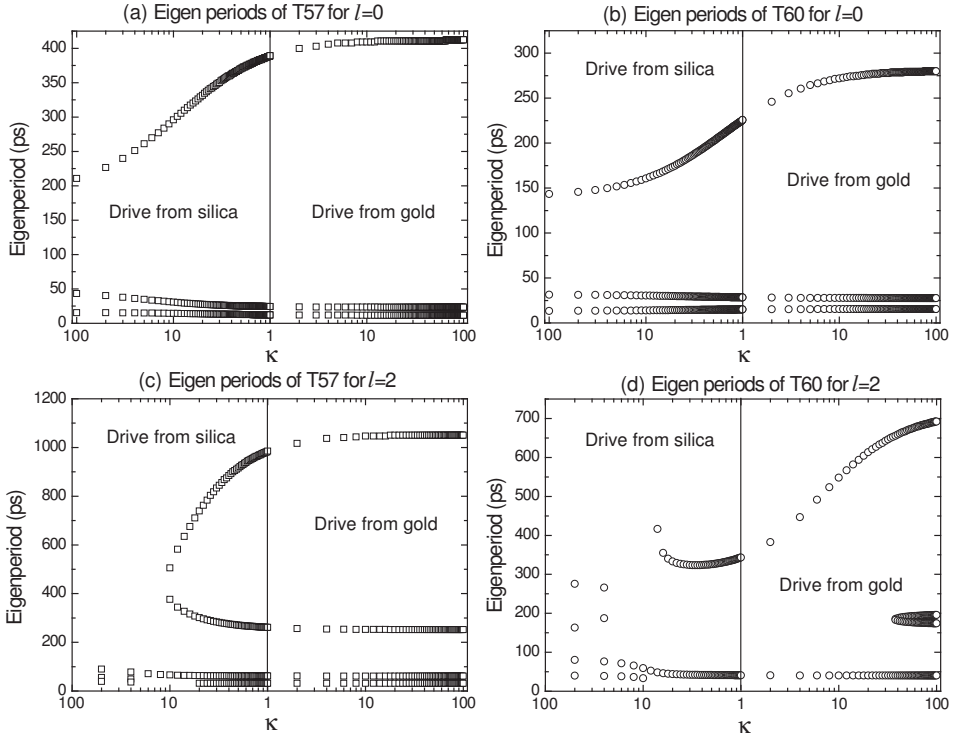

Figure 5.3: Calculated periods of eigenmodes vs. interface factor κ varying from 0.1 to 100. (a) and (b) show $l = 0$ results for particle T57 and T60. (c) and (d) $l = 2$ results.

Eigenfrequencies in the two-shell model

In our calculation, we only focus on the $l = 0$ and $l = 2$ modes. The heating induced by optical excitation results in expansion and stimulate modes that do not maintain a constant volume, i. e. do not excite pure torsional modes ($l = 1$). Of all vibrational modes of the particle, the most important ones are expected to be the $l = 0$ and the $l = 2$ modes because they possess higher symmetry and lower energy and tend to be excited by plasmon resonance in the gold-shell particle in a symmetric environment.

Fig. 5.3 displays the calculated periods of eigenmodes versus interface factor κ varying from 1 to 100, driven from the gold or the silica side, for the two particles both at $l = 0$ and $l = 2$. Fig. 5.3 (a) and (b) show the calculated results of $l = 0$ for particle T57 ($R_1 = 228$ nm, $R_2 = 266$ nm, $R_3 = 276$ nm)

and T60 ($R_1 = 156$ nm, $R_2 = 181$ nm, $R_3 = 221$ nm), respectively. Fig. 5.3 (c) and (d) show the calculated results of $l = 2$. For each plot in the Fig. 5.3, we present the calculated results at the left for $\kappa = 100 - 1$ driven from the silica side, and at the right for $\kappa = 1 - 100$ driven from the gold side, corresponding to a free silica shell via well connected shells to a free gold shell. For our experiments, we drive from the gold side, and the modes driven from silica side will not be excited in the experiments.

In Fig. 5.3 (a) and (b), we can see that the three solutions continuously change from the situation of an almost free silica shell ($\kappa = 100$, drive from silica) to a well connected two-shell ($\kappa = 1$), and to an almost free gold shell ($\kappa = 100$, drive from gold). The results for $\kappa = 100$ driven from the gold side are 411 ps and 23 ps for the first two solutions, which are very close to the calculated results of free-shell Lamb theory, 413 ps and 23 ps, and correspond to the fundamental $n = 0$ and first higher harmonic $n = 1$ mode, respectively.

In Fig. 5.3 (c), we present the calculated results of a T57 particle for the $l = 2$ mode. With increasing κ, the system creates new eigenmodes from $\kappa = 10$ driven from silica side, which contains two branches, continuously evolving into the free gold-shell modes, settling on the periods of 1050 ps and 252 ps for κ =100 driven from gold side. They are again very close to the free-shell Lamb theory results of $l = 2$, 1065 ps and 252 ps.

The calculation result of particle T60 for $l = 2$ is more complicated, shown in Fig. 5.3 (c). If we increase the interface factor κ from 100 (free silica shell), again at $\kappa = 10$ driven from silica side, new eigenmodes develop in the system, but only one of the branches shows up, and the other one is suppressed. In the gold, at $\kappa = 40$, a second branch appears, splits into two, and reaches 196 ps and 174 ps at $\kappa = 100$. The slowest mode reaches 692 ps. Compared with the free-shell Lamb theory calculation results for T60 at $l = 2$, 722 ps and 172 ps, we are again quite close to the free-shell gold-shell for $\kappa = 100$. This particle (T60) contains a thinner gold shell (25 nm) and a thicker silica shell (40 nm), which makes the outer shell become heavier and not a significant factor to the eigenmodes frequencies. As to the splitting of the mode around 180 ps for $\kappa > 40$ at the gold side, we notice a resonance of the two-shell system for the gold shell and silica shell, because it coincides with the period of the modes in the silica shell for $\kappa > 70$ (in the left side of Fig. 5.3 (d)).

In Table 5.1 we summarize the relevant eigenmodes calculated by the

Particles	Mode (n, l)	Calculated periods (ps)			
		Lamb theory Free shell ($\kappa = \infty$)	Two shell model		
			(κ= 1)	(κ= 10)	(κ= 100)
T57 R_1=228 nm R_2=266 nm R_3=276 nm	(0,0)	413	388	409	411
	(1,0)	23	24	24	23
	(0,2)	1065	984	1047	1050
	(0,2)	252	261	253	252
T60 R_1=156 nm R_2=181 nm R_3=221 nm	(0,0)	281	225	272	280
	(1,0)	15.4	28.4	27.7	27.6
	(2,0)	-	15.0	15.4	15.4
	(0,2)	722	343	548	692
	(0,2)	172	-	-	196, 174

Table 5.1: Comparison of free-shell Lamb theory and double-shell model for particle T57 and T60.

free-shell Lamb theory and the two-shell model.

Displacements

For a given mode, the displacement u_r can be calculated by Eq.(5.3), and helps us to visualize the motion of the particle. We only present displacements for $l = 0$ modes. In case of $l = 2$, the displacements are more difficult to display because those are a combination of radial and tangential motions. For $l = 0$, the displacement, of course, is exclusively along the radial direction. The interface factor was set to be κ=1 in this calculation (well connected shells), to achieve a clear display of the displacements at both sides of the interface.

The calculated results are shown in Fig. 5.4 for the particle T57. Fig. 5.4 (a) shows the normalized displacements at each radial position for the (0,0) mode. We denote the gold region as the gray area and silica as light gray. The displacement is maximum at the inner surface of the gold shell (notice the negative sign at the displacement axis), and decreases along the radial direction. We note that the displacement keeps one sign, which corresponds to a movement towards one and the same direction both in gold and in silica.

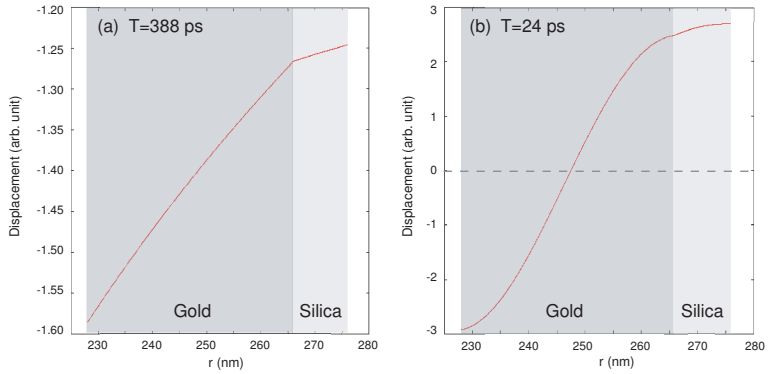

Figure 5.4: Calculated normalized displacement along the two-shell of particle T57. (a) Lowest radial mode (0,0) with eigenfrequency of 2.54 GHz (T=388 ps). (b) The first higher harmonic mode (1,0) with eigenfrequency of 41.7 GHz (T=24 ps). A zero point appears make it a thickness vibrational mode.

Therefore the particle coherently vibrates with a 388-ps period breathing mode.

Fig. 5.4 (b) shows the displacement for the (1,0) mode, the first higher harmonic mode for $l = 0$. The calculated eigenfrequency of this mode is 41.7 GHz, corresponding to a period of 24 ps. We notice one zero point of the displacement in this mode. Further, the displacement of the inner and outer surface have opposite directions so that this mode corresponds to a thickness vibration.

Similar computations were carried out for particle T60, and are shown in Fig. 5.5. Here, Fig. 5.5 (a) represents the normalized displacement for the (0,0) mode, which can be identified again as the breathing mode. The first higher harmonic mode (1,0), depicted in Fig. 5.5 (b), again shows one zero point, but in this case very close to the gold-shell interface. Finally, Fig. 5.5 (c) gives the displacement for the mode (2,0), the second higher harmonic mode for $l = 0$ with two zero points, one in gold, one in silica. This mode corresponds to coherent thickness vibrations of each shell, that are resonant for this particle because of a fortuitous mass balance at each side of the interface. For the particle T60, the mode (1,0) is not expected to be measured because the outer surface of gold does not vibrate and the circumstance in our experiments that the optical response is mainly sensitive to changes at the outer part of the gold shell.

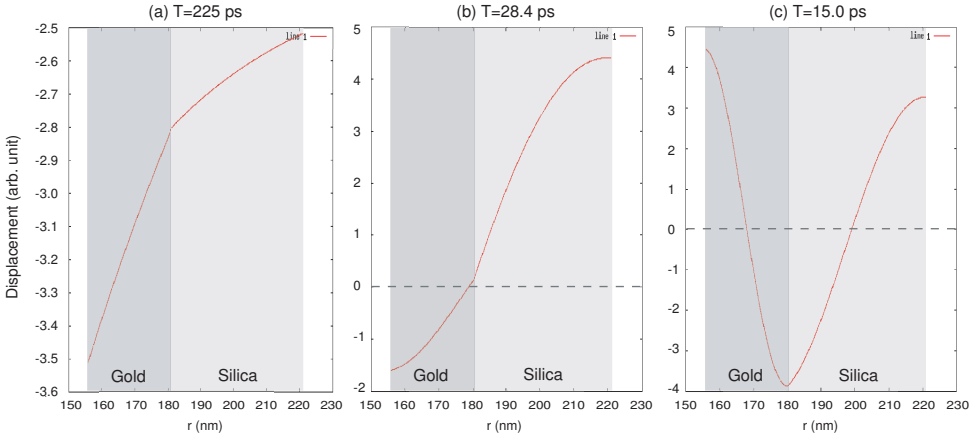

Figure 5.5: Calculated normalized displacement along the two-shell of particle T60. (a) Lowest radial mode (0,0) with eigenfrequency of 4.44 GHz (T=225 ps). (b) The first higher harmonic mode (1,0) with eigenfrequency of 35.2 GHz (T=28.4 ps). (c) The second higher harmonic mode (2,0) with eigenfrequency of 66.7 GHz (T=15.0 ps)

5.3 Observation of coherent vibrations in 1-kHz pump-probe setup

Acoustic vibrations were observed in pump-probe experiments following excitation by a 120-fs pulse extracted from a femtosecond amplified Ti-sapphire laser operating at 1 kHz. The experimental set-up is described in Sec. 4.4. The incident angle of the pump light is 0 and for the probe light is 45°.

5.3.1 Breathing vibrations in the ordered sample T57

In the experiments, we first examine the 3-D photonic crystal ordered sample composed of T57 particles. A typical experimental trace is shown in Fig. 5.6. We use 10-mJ/cm^2, 800-nm pump pulses, detect at 670-nm probe wavelength, and find an oscillation with a period of 400 ps after the sharp electronic peak, already analyzed in detail in Ch. 4. Since the oscillation compares favorably with the calculated period of 388 ps in the two-shell model and 413 ps in the free-shell model, we identify the vibration as the breathing mode of the shell particle.

This breathing mode appears in many probe wavelengths though with

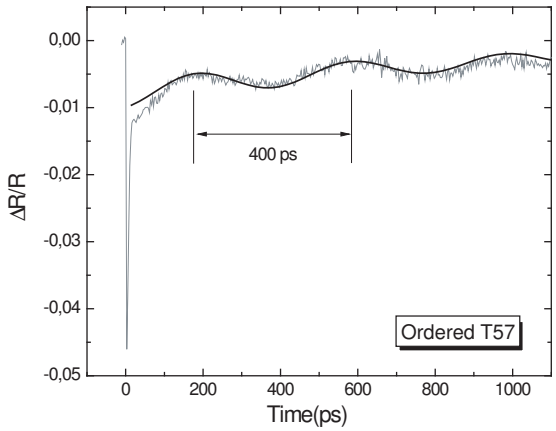

Figure 5.6: Transient reflectivity of a photonic crystal of particle T57 following a pump pulse. Solid line is the experimental result, dashed line is the fitting curve. Probe wavelength is at 670 nm, pump fluency of 10 mJ/cm^2 at 800 nm.

different measured amplitudes. Fig. 5.7 (a) shows the measured transient reflectivity at a probe wavelength of 490 nm (gray line), of 550 nm (dark gray line), and of 700 nm (light gray line). Fig. 5.7 (b) represents the linear reflectivity spectrum taken at an incident angle of 30°, where gray regions are indicated to show the detection bandwidths. In Fig. 5.7 (c) we plot the spectra of measured oscillations for the three wavelengths, 490 nm (gray line), 550 nm (dark gray line), and 700 nm (light gray line), which all show a peak at 2.5 GHz.

The temporal evolution of $\triangle R/R$ can be approximated quite faithfully by the function

$$\frac{\triangle R}{R} = A_1 \exp(-\frac{t}{\tau_1}) + A_2 \exp(-\frac{t}{\tau_2}) \cos\left(\frac{2\pi}{T}t + \varphi\right) , \qquad (5.10)$$

where t is time, and the fitting parameters T and φ are the period and phase of the oscillation. The first part of Eq. (5.10) is an exponential decay term with decay time τ_1 and amplitude A_1. The second part is an exponentially damped oscillation with period T, decay time τ_2, and amplitude A_2. The fitted parameter values are summarized in Table 5.2. We note that the period of oscillation is 394 ps with a standard deviation of 2.5%. The detected phase of the oscillations is $\sim$0.13 π.

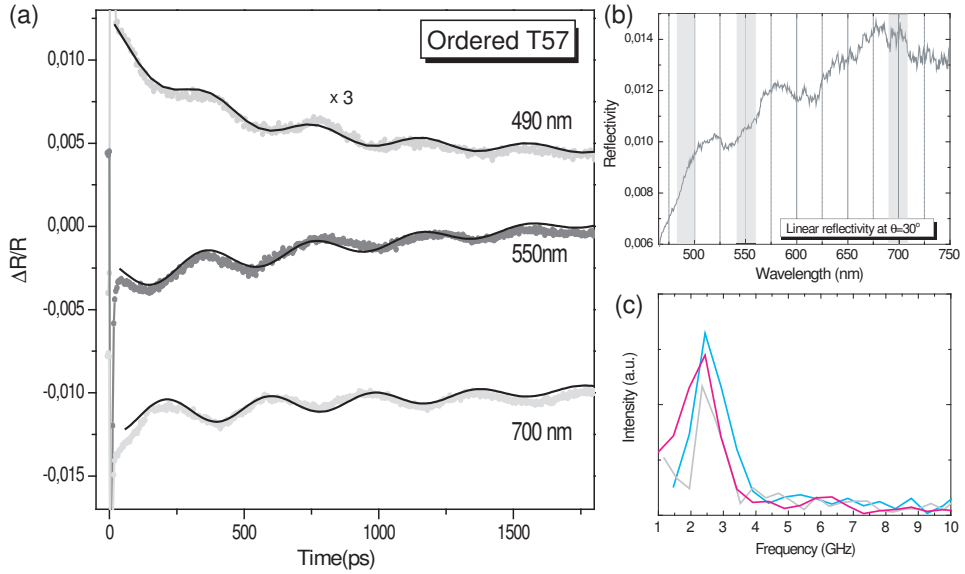

Figure 5.7: (a) Transient reflectivity of a T57 gold-shell photonic crystal at different probe wavelength, gray lines are measured traces and black curves fits. Pump fluency is 4 mJ/cm^2 at 800 nm. (b) Linear reflectivity spectrum at incident angle 30°. (c) Spectra of oscillations taken at 490 nm (gray line), 550 nm (dark gray line), and 700 nm (light gray line).

When comparing these results with the calculations in the previous section, we identify the oscillation as the breathing mode of the shell particle. The average period of 394 ps is nicely in between of the two calculated results, 413 ps of the free-shell model, and 388 ps of the two-shell model with good interface connection ($\kappa = 1$). Therefore, we can conclude that $1 < \kappa < 100$ and that the coupling at the interface of the particle between the gold shell and the outer silica shell is probably not perfect.

The phases of the measured oscillations are $\sim 0.1\pi$ corresponding to virtually impulsive excitation of vibrations after the optical pump pulse. Recalling the dynamics following excitation by a pump pulse (see section 4.2), the lattice gains energy from hot electron gas via electron-phonon coupling, which typically takes a few picoseconds. Therefore the lattice is rapidly heated up and starts to vibrate.

The amplitude of the oscillations in Fig. 5.7 (a) depends on the probe

Particles	λ (nm)	Parameters					
		A_1	A_2	τ_1 (ps)	τ_2 (ps)	T (ps)	φ (rad)
Ordered T57 on a silicon substrate	490	2.4×10^{-3}	2.5×10^{-4}	400	1500	395	0.1 π
	550	-7.6×10^{-3}	1×10^{-3}	3300	1200	400	0.2 π
	700	-4×10^{-3}	-1×10^{-3}	3200	1200	386	-0.1π
	average	-	-	-	1300 ±200	394±10	0.1±0.1 π
Disordered T57 on a glass substrate	560	-1.9×10^{-3}	-2×10^{-4}	2200	600	265	-0.1π
Disordered T60 on a silicon substrate	540	-2.1×10^{-2}	-2.4×10^{-3}	500	700	193	0

Table 5.2: Fitting parameters of measured oscillations in 1-kHz pump-probe experiments.

wavelength. We note that in the first experiments of the breathing mode of this gold-shell photonic crystal by Mazurenko [37], a strong vibration also appeared at 950 nm beyond the range of our present setup with an amplitude $\triangle R/R$=4%. We observe that the oscillations at 550 nm and 700 nm have different polarities, i.e. while the electronic response at 550 nm and 700 nm are both negative, the oscillations have opposite phase (fitting parameter A_2 have different sign). In our experiments, we measured traces of several points on the sample surface for each probe wavelength and took the average. Therefore, the opposite sign of the oscillations is not accidental. We trace this phenomenon back to a modulation of the spectrum caused by the acoustic vibration. The ultrafast electronic response of the dielectric constant of gold (see chapter 4), is not changing sign when going from 550 nm to 700 nm. The periodic movement of the particle surfaces, however, induces a small periodic shift of the spectrum. Therefore the sign of the oscillations will depend on the spectral position of the probe and local derivative. We indeed measured a decrease of reflectivity in the first half oscillation period at 490 nm and 550 nm, both at the left side of a peak (see Fig. 5.7 (b)), and an increase at 700 nm for the first half period, at the right side of a peak. The expansion of particle size apparently leads to a red shift of the spectrum.

The damping time of the vibrations, τ_2, can be explained in terms of inhomogeneous variations of the particle size, which is expressed by τ_2 =

$r_s T/\sqrt{2}\pi\sigma_r$. Here T is the vibrational period, r_s the particle radius, and σ_r the particle size dispersion [36]. Inserting $T = 394$ ps taken from the experimental data and $\sigma_r/r_s = 0.05$ known from the SEM data [17], we obtain τ_2=1.77 ns, which is close to the experimentally observed value $\tau_2 = 1.3 \pm 0.2$ ns. Additional damping may occur through energy transfer to the silica core [36][33][89], which however is difficult to estimate.

5.3.2 Elliptical vibrations in disordered samples

For comparison, similar experiments are performed on disordered samples of T57 ($R_1 = 228$ nm, R_2=266 nm, R_3=276 nm) and particle T60 ($R_1 = 156$ nm, R_2=181 nm, R_3=221 nm) (see Fig. 2.3 in chapter 2). Unfortunately we do not possess an ordered T60 sample. Fig. 5.8 shows the experimental results, measured at 560-nm probe wavelength for T57 particles on a glass substrate and at 540-nm probe wavelength for T60 particles on a silicon substrate. The pump is again at 800 nm and the fluency is 4 mJ/cm^2. Each trace is an average of scans on 5 different sample points, including thick parts and thin parts, which all give reproducible and comparable results. The experimental trace of Fig. 5.8 (a) shows a T57 oscillation of 265-ps period , corresponding to 3.8 GHz (see Fig. 5.8 (c)). For T60 particles an oscillation of 193-ps period is found (see Fig. 5.8 (b)),corresponding to 5.2 GHz in (see Fig. 5.8 (d)).

The oscillation frequency of the disordered T57 sample coincides with fast $l = 2$ branch of elliptical modes in the two-shell model, which yields 261ps-252ps for $\kappa = 1 - 100$. For particle T60, the intermediate branch of $l = 2$ splits into two at $\kappa = 100$ (a loose interface connection), gives 196-ps and 174-ps periods. The slower one is very close to the observed 193-ps period. Therefore, all oscillation frequencies observed in the disordered T60 sample correspond to the $l = 2$ mode and $\kappa \sim 100$.

5.3.3 Discussion

The damped oscillatory signals again can be fitted by Eq. 5.10. The fitted parameter values are summarized in Table. 5.2. The damping time of the 265-ps oscillation of particles T57 is 600 ps (see Table. 5.2), which is a factor of two shorter than the calculated damping due to the 5% of size dispersion $\tau_d = r_s T/\sqrt{2}\pi\sigma_r = 1.2$ ns. For the 193-ps oscillation of particle T60, damping time of 700 ps is measured, close to the calculated value for a size dispersion

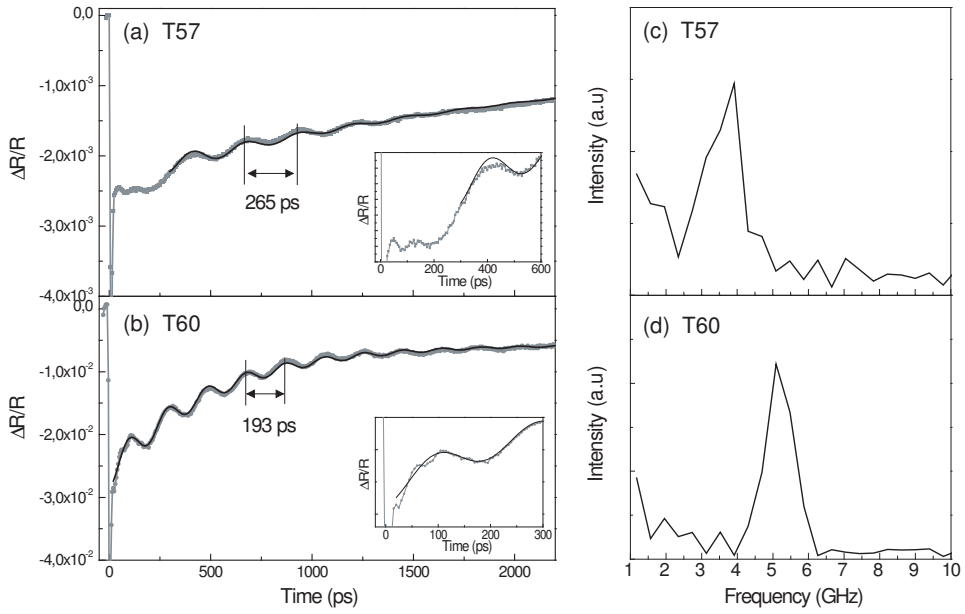

Figure 5.8: Transient reflectivity of disordered samples, (a) T57 on glass measured at 560 nm (gray line) and fit (black curve) , (b) T60 on silicon measured at 540 nm (gray line) and fit (black curve). Insets are zoom-ins at short time scale. Pump fluence is 4 mJ/cm^2 at 800nm. (c) and (d) show the FT of oscillations for T57 and T60.

(870ps). Further, the damping of the background is 2.2 ns for T57 and 0.5 ns for T60. There are a lot of terms that can influence the damping and cooling time, such as the size, the ordering of particles, and the number of layers. In the case of our experiments, we suspect the substrates of the two samples, T57 on glass and T60 on silicon, make the main difference.

The phase of all measured oscillations are always close to 0°, except for one measured trace of T57 in Fig. 5.8 (a). Here, we note a clear delay of the 265-ps mode, which starts vibrating only after 200 ps. We recall that the experimental result is an average over 5 sample points, is reproducible, and thus is not attributable to accidental noise in one measurement. During the 200-ps delay period, a fast oscillation is present directly following the fast electronic response which rapidly damps out as shown in the inset of Fig. 5.8 (a). The period of the fast oscillation is ∼80 ps. Similarly, for particle T60,

a fast oscillation of ∼50-ps period appears on the short time scale, shown in the inset of Fig. 5.8 (b). There is no period calculated by us coinciding with those fast oscillations. The nearest modes are the first higher harmonic vibration of $l = 2$, ∼62-ps for particle T57 at $\kappa = 1 - 100$ and 40-ps for particle T60 at $\kappa = 100$. When the pump laser heats up the lattice via electron-phonon coupling in a few picoseconds, the rapid expansion of the lattice excites a superposition of eigenmodes of the particle, each with their own frequency and damping. The modes with the lowest damping survive, while modes with higher frequencies will quickly interfere down or damp to zero. This process seems to take 200 ps for particle T57.

The damping time of the background, τ_1, refers to the cooling of particles and is observed to vary with the position on the sample. We suspect that the cooling critically depends on the local organization of particles, and the number of layers. Roughly speaking, cooling times are found in the range from several hundreds of picoseconds to few nanoseconds.

In these experiments, we measured the breathing vibrational mode on the ordered sample, and elliptical vibrational modes on the disordered samples. We think the observation of different modes in different sample, is due to the ordering of the particles. The nature of mode selection can depend on (i) the excitation and (ii) the damping, which we will discuss in more detail now.

(i) In a pump-probe experiment, electrons are heated in the metal shell via absorption of pump fluence. The field distribution around shell particles similar to ours excited by incoming light has been calculated by J. Pennikhof [54]. A strongly inhomogeneous field pattern is calculated, that can be amplified by the presence of other particles. The inhomogeneous field pattern leads to inhomogeneous excitation of hot electrons in the shell, which in turn will give rise to an inhomogeneous thermal stress. Therefore, the ordering of neighboring particles may influence the initial stress and displacement of the shell. In case of the ordered sample, the excitation is largely symmetrical because of the close-packed structure, and tends to excite symmetrical vibrations, i.e. breathing modes. However for the disordered sample, the random touching between particles allows inhomogeneous excitation and probably leads to excitation of lower symmetry vibrations, such as the elliptical mode for $l = 2$.

(ii) The second issue is the damping of the modes. As we discussed earlier, the impulsively heating of the pump pulse excites a multitude of acoustic modes. The damping of each mode may depend differently on the symmetry

of the surrounding environment, i.e. the number of touching particles and the mechanic coupling between particles. A symmetric ordering of particles suppresses asymmetric vibrations while an asymmetric ordering suppresses symmetric vibrations. Apparently for the ordered sample composed of close-packed particles, the symmetric breathing mode survives. In the disordered samples, the elliptical modes show up in the evolution.

5.4 Observation of vibrations with ASOPS

We also examined the samples with a novel setup based on the so-called Asynchronous Optical Sampling (ASOPS) technique developed at the University of Konstanz [62] (see Ch. 3). In brief, the setup is relying on two synchronized mode-locked femtosecond Ti-sapphire lasers with repetition rates of f =1.00000 GHz, and 1.00001 GHz, respectively. One acts as pump and the other as probe. As a result, the time delay between the pulse trains is ramped between zero and 1 ns with a scanning rate of 10 kHz. Therefore a 1-ns temporal measurement window opens while keeping femtosecond time resolution. The wavelength of pump and probe light can be independently tuned between 750 nm and 850 nm, and their polarizations are usually chosen to be perpendicular. The pump beam is focused down to a 50-μm spot on the sample surface, with incident angle of $\theta = 0^\circ$ and fluence of 10 μJ/cm^2 per pulse, which is about 100 times lower than that of the 1-kHz setup used in Sec.5.3. The probe beam is focused at the same 50-μm spot in the pumped zone on the sample surface, but with an incident angle of $\theta = 45^\circ$, and of much lower fluence than the pump pulses. The reflected probe light is detected by a photoreciever and the signal is recorded by a computer operating in Labview. The sensitivity of the setup is as good as 10^{-7}, much better than that of the 1-kHz setup ($\sim 10^{-4}$).

5.4.1 $l = 2$ higher mode

In Fig. 5.9, we display the experimental result of the disordered T60 sample (R_1 = 156 nm, R_2 = 181 nm, R_3 = 221 nm). A thick region on the sample surface was selected for the measurement, which contains several layers of particles. The probe is tuned to 780 nm, and the pump to 830 nm with a fluency 40 μJ/cm^2 per pulse. Similar as the results of 1-kHz pump-probe experiments, an oscillation appears in the transient reflectivity trace (gray

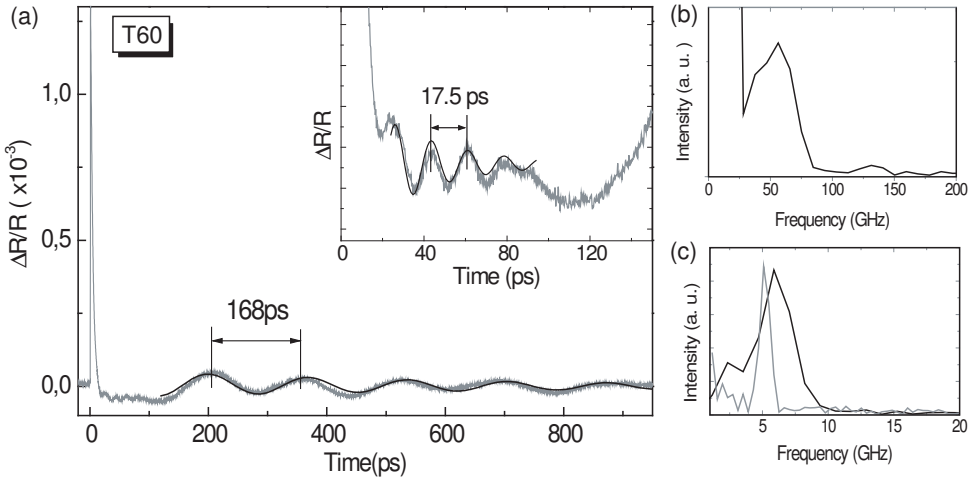

Figure 5.9: (a) Transient reflectivity of disordered sample T60 on a silicon substrate measured by ASOPS (gray line), and fitg for the slow oscillation (black curve). Inset shows a zoom in at short time scale. Probe wavelength is 780 nm, pump fluency 40 μJ/cm^2 at 830 nm. (b) shows the FT of fast oscillation and and (c) is FT of slow oscillation of ASOPS (black line) and of 1-kHz setup (light gray).

line) directly following the ultrafast electronic response, shown in the Fig. 5.9 (a). The oscillation can be fitted by Eq. (5.10) yielding a period of 168 ps (black curve in Fig. 5.9 (a)). In Fig. 5.9 (c), we show the spectrum of the oscillation, peaking at 5.9 GHz, and compare this with the measured peak at 5.2 GHz for 1-kHz setup trace on the same sample. According to the calculations of Sec. 5.2 for the T60 particle, the measured frequency coincides with that of the intermediate $l = 2$ mode of a free-shell (172 ps), and that one of the $l = 2$ branches of two coupled shells for $\kappa = 100$ which gives 174 ps. Therefore, we interpret this mode as the $l = 2$, elliptical vibration of a free shell.

Compared with the observed 195-ps period vibration in the 1-kHz pump-probe experiment, we measured a different period at 168 ps in the ASOPS experiment on the same sample. The reason for the difference my be the different repetition rate and sensitivities of the two experiments. The ASOPS has a slow noise oscillation $\sim$2 GHz, which is difficult to average out and tends to broaden the frequency peak for the lower frequencies.

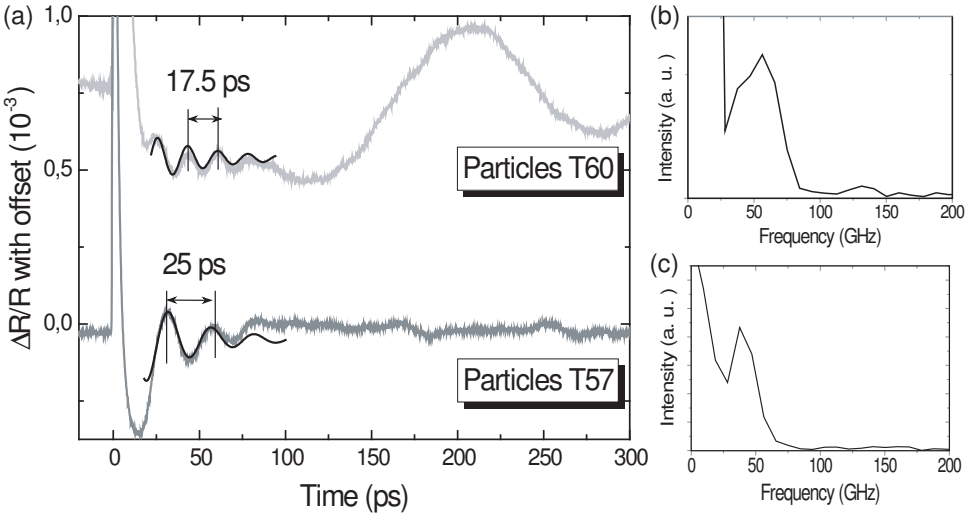

Figure 5.10: (a) Transient reflectivity of disordered sample T60 (light gray) and ordered T57 (gray) on silicon substrates measured by ASOPS, and fits (black curves). (b) and (c) are the FT spectra of the fast oscillation in the two particles.

For the disordered T57 sample on a glass substrate, we did not manage to measure any oscillation by ASOPS. The heat conduction of the glass substrate is much smaller than that of the silicon substrate of T60 sample. This yields a higher temperature in the pumped zone on the sample surface. As a result, we are forced to limit the fluences to $< 2\mu\mathrm{J/cm}^2$ to prevent the melting of particles, which apparently is not enough to generate a sufficiently strong vibrational signal. For the 1-kHz experiment, the lower repetition rate permits much higher fluences and thus signals without damaging the sample.

5.4.2 Observation of thickness vibrations

We note that a fast oscillation appears in Fig. 5.9 (a) on the short time scale, which is shown to better advantage in the inset. The fast oscillation is fitted by Eq. (5.10). The fitted period of 17.5 ps corresponds to 57 GHz in the measured spectrum (Fig. 5.9 (b)). We interpret this oscillation as the second higher harmonic mode of $l = 0$ in the two-shell model, which also coincide with the first higher harmonic mode of $l = 0$ in the free-shell model (see Table 5.1). Both modes correspond to a thickness vibration of the gold shell

Particles	vibration	Parameters					
		A_1	A_2	τ_1 (ps)	τ_2 (ps)	T (ps)	φ (rad)
Ordered T57 on a silicon substrate	fast	-	$1x10^{-4}$	-	35	25	-0.66π
Disordered T60 on a silicon substrate	slow	$1x10^{-5}$	$4x10^{-5}$	300	600	168	-0.4π
	fast	-	$1.2x10^{-5}$	-	33	17.5	$-\pi$

Table 5.3: Fit parameters of measured oscillations in ASOPS experiments.

(see Fig. 5.5 (c)).

On the ordered photonic crystal sample T57 on a silicon substrate, we also observed a fast oscillation, with probe wavelength at 750 nm and pump at 820 nm for 10 μJ/cm^2 fluence. Fig. 5.10 shows the comparison of the fast oscillations detected on the two samples. For particle T57, the period can be fitted as 25 ps, corresponding to a peak at 40 GHz in the spectrum of vibration, shown in Fig. 5.10 (c). The measured period fits very well with the first higher harmonic of the pure radial ($l = 0$) vibrational period of 23-24 ps in the two-shell model for $\kappa = 1 - 100$, and corresponds to a thickness vibration of the gold shell.

5.4.3 Discussion

The fitted parameters of the vibration in ASOPS experiments are shown in Table 5.3. The damping time of the vibrations, expressed by the parameter τ_2, can again be accounted for by inhomogeneous variations of the particle size, $\tau_d = r_s T/\sqrt{2}\pi\sigma_r$, with the particle size dispersion $\sigma_r/r_s = 0.05$ known from the SEM data [17]. For the $l = 2$ vibration $T = 168$ ps, we compute 760 ps, which fairly agrees to the measured damping time of 600 ps. We know the size polydispersity is 3% for the silica core and about 5% for the gold-shell colloids. Assuming the particle to particle variation of shell thickness has a comparable value as the variation of the particle size, we obtain 79 ps and 113 ps for the thickness vibrational modes of particle T60 and T57, which are about three times longer than what we measured, 33 ps and 35 ps, respectively. This suggests a spread in the thickness of the gold shell between particles as much as 12%.

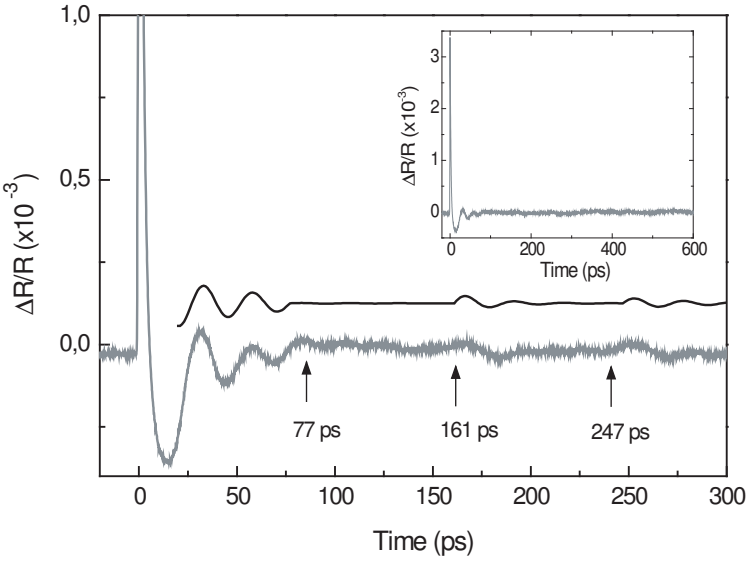

Figure 5.11: Transient reflectivity of disordered T57 sample on a silicon substrate measured by ASOPS (gray line), and a simulation for the echoes (black curve). Inset is the expanded scale of the measurement.

Other damping mechanics of thickness vibrations may occur by energy transport to the silica core. For particle T57, we observed 'echoes' to appear around 160 ps and 250 ps with 25-ps period. We interpret those as the echoes of the longitudinal acoustic waves through the particle core. Fig. 5.11 shows the measured trace (gray line) and a simulation of echoes (black curve), including the 180° jump at the interface reflection. The inset of Fig. 5.11 displays the measurements in an expanded scale. In the simulation, we consider three echoes, arriving at 77 ps, 161 ps, and 247 ps, respectively. Note that the first echo happens to have a destructive phase with the local vibration, explaining the sudden stop of the local thickness vibration at t =77 ps. The computed curve resembles our experimental trace very well. The average time separation between echoes, 82 ps, can be deduced, which is close to the 76 ps for the 556-nm diameter silica core of particle T57.

As we discussed in the previous section, in the excitation process the selection of modes depends on the degree of ordering of the particles. Therefore in the ordered T57 photonic crystal sample, the breathing mode should

Vibration Modes (n,l)	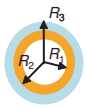	Period of oscillations (ps)				
		Particle: T57			Particle: T60	
		Calculation for κ=1	Calculation for κ=100	Measure ment	Calculation for κ=100	Measure ment
Breathing (0,0)		388	411	394±10	280	-
Thickness (1,0) or (2,0)		24	23	25±3	15.4	17.5±2
Elliptical (0,2)		261	252	265±5	174 196	168±10 195±5
Core echo for longitudinal wave		76		82±5	52	-

Table 5.4: Summary of calculated and measured results.

also have been excited and detected in ASOPS experiments. The missing of the breathing mode (400 ps, 2.5 GHz) can be understood by the destructive interference with the 1-GHz repetition rate and its higher harmonics of the pump fluence. The damping time of breathing mode in particle T57 is measured to be longer than 1 ns (see Table 5.2). Therefore, the vibration excited by the one pump pulse can not decay in the 1-ns temporal window and destructively interferes with the next excitation pulse.

Finally, the phase φ of the fast oscillations (see Table 5.3), -π and -0.66 π, corresponding to 9 ps and 5 ps delays of vibrations. This can be understood as the time the excitation process of phonons takes for the lattice to gain energy from optically excited hot electrons via electron-phonon coupling (see Ch. 4). All results are summarized in Table 5.4

5.5 Conclusions

We demonstrate and discuss acoustic vibrations in spherical gold-shell particles. The vibrational modes are calculated by a double-shell model with a phenomenological interface coupling factor κ. In Table 5.4, we summarize the calculated (numbers without bracket) and experimental results (numbers

in brackets). With all the observed vibrations of particle T60, the fitted κ tends to be 100, corresponding to a loose connection between the gold shell and outer silica shell. For particle T57, the difference between calculated result for $\kappa = 1$ and 100 is very small, and both of them are close to the experimental results. Therefore we conclude that the connection between gold and silica in the gold-shell particle is loose and the gold-shell can be considered as being largely mechanically decoupled.

All measured vibrational periods satisfactorily agree with the calculated results. We have demonstrated excitation and detection of breathing modes, thickness modes, and elliptical modes in gold-shell particles. The period of vibration shows a dependence on the gold-shell size. Further, core echoes of thickness vibrations of gold shell are observed.

Chapter 6

Acoustic vibrations of elliptical particles

Abstract In this chapter, we demonstrate generation and detection of acoustic vibrations in elliptical gold-shell particles, which have been deformed by ion beam irradiation. In pump-probe experiments, the observed long periods of transient reflectivity modulations correspond to longitudinal vibrations along the long and short axis of the particle. From fast oscillations observed on the short time scale, we conclude that the thickness of the gold shells is small at the equator and thick at the pole of the particle.

6.1 Introduction

In the previous chapter, we demonstrated acoustic vibrations of spherical gold-shell particles, caused by rapid heating by optical excitation. The vibrational period appeared to depend on size and ordering of the particles. In this chapter, we examine the geometric shape dependence of acoustic vibrations of gold-shell particles.

In metallic nano-structures, acoustic vibrations have been observed not only in spherical structures, but also in many particles of other geometrical shapes. In the beginning of this century, Perner and his co-workers investi-

gated the vibrational dynamics of ∼40-nm wide and ∼100-nm long ellipsoidal silver nanoparticles, and observed that the period of the modulation depends on the particle axis probed [16]. Hartland and his co-workers investigated vibrational modes of gold nanorods by pulsed laser excitation and found that the period depends linearly on the length of the rod [34][39]. Further, vibrations were measured in a nanostructure consisting of a periodic array of copper wires embedded in a glass matrix on a silicon substrate [97]. Nanoscale gold triangles of different sizes and thicknesses on silicon and glass substrates were analyzed with impulsively excited acoustic dynamics [38]. Acoustic vibrations were observed in yet other nanostructures [39-45]. The acoustic vibrational periods appeared to depend on size, shape, and elastic constants of the material. In all these experiments on nanometer-sized objects, time-resolved spectroscopy was used to examine the material properties.

In this chapter, we focus on elliptical gold-shell particles, deformed from a spherical shape by ion beam irradiation. By performing pump-probe experiments, acoustic vibrations can be excited and observed, providing information on the geometry of the particle and the thickness of the gold shell, that can not be extracted from SEM pictures.

6.2 Deformation of particles

Silica-core/Au-shell spherical particles can be deformed by ion beam irradiation to an elliptical shape. The sample was fabricated by J.Pennikhof [92] [93]. The spherical particles T60 were synthesized using the method described in Ch. 2, with a 156-nm radius silica core, 25-nm think gold shell, and 40-nm thick silica cap shell. After synthesis, a droplet of the colloidal suspension was dried on a Si(100) substrate under nitrogen flow, so that the typical surface coverage was well below one monolayer. The ion beam irradiations were performed by a 6-MV Van de Graaff accelerator. The 6-MeV Au^{3+} ion beam was directed at an angle of 45° to the substrate. During the irradiation, the sample was clamped to a liquid-nitrogen-cooled copper substrate holder. Fig. 6.1 (a) shows a sketch of a deformed particle. As an example, Fig. 6.1 (b) shows a side-view SEM image of deformed particles with the thick silica shells (133 nm) [54].

The irradiation-induced plastic deformation of amorphous materials can be described by a visco-elastic thermal spike model [54][94][96]. An energetic ion penetrates a solid and heats a small cylindrical region along the ion track

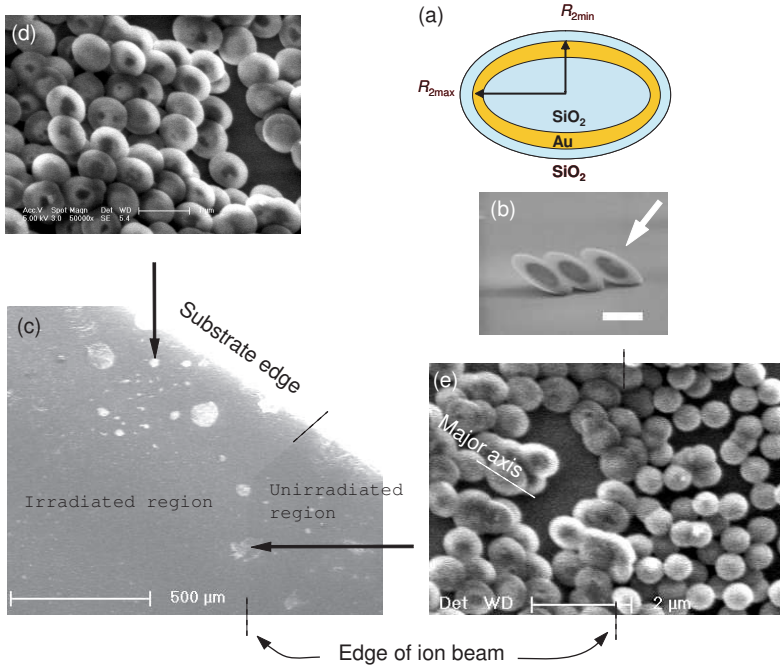

Figure 6.1: (a) Sketch of elliptical particles deformed by iron beam irradiation. (b) Side-view SEM of deformed particles with thick silica shells [54]. (c) Top-view SEM of T60 sample on a silicon substrate, partly irradiated by ion beam with edge of ion beam indicated by dashed line. (d) Top-view SEM image of deformed T60 particles. (e) Top-view of particles on edge (dashed line) of ion beam, particles at left side are deformed, at right side are spherical.

in less than 10^{-12} s. The rapid thermal expansion of this hot track causes shear stresses resulting in a net local anisotropic deformation of the material. In contrast to amorphous materials such as silica, crystalline materials like metals do not show any anisotropic deformation under ion irradiation [95]. The deforming silica core imposes a deformation on the gold-shell so that an elliptical particle with metallic shell is created.

In our T60 sample, deformation by 6 MeV Au^{3+} ions at 1×10^{15}cm^{-2} fluence, yields size aspect ratios (ratio major to minor-axis) of 1.7±0.2, as deduced from SEM images [54]. Fig. 6.1 (c) shows a top-view SEM image of our deformed T60 sample on a silicon substrate, where the edge of ion beam can be distinguished as indicated by dashed lines. A few bright spots can

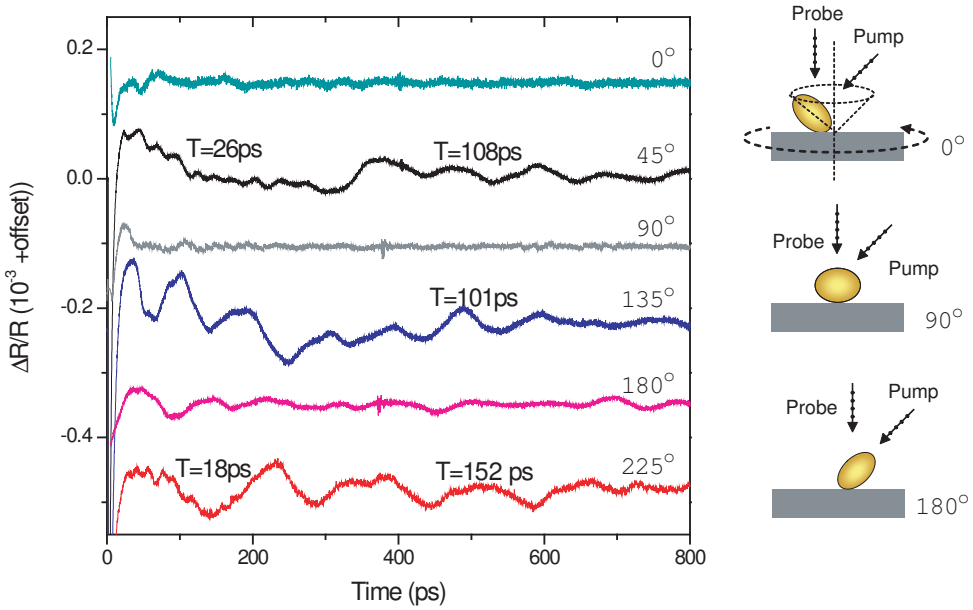

Figure 6.2: Transient reflectivity of deformed T60 samples vs. orientation angle of particles. Pump fluency is 0.02 mJ/cm^2 at 780 nm, probe at 820 nm.

be recognized as thick regions containing more than one layer of particles. Fig. 6.1 (d) is a top-view SEM of a thick deformed region and Fig. 6.1(e) shows particles on the ion beam edge with the left side deformed and the right side the original spherical shape. We note that all the elliptical particles have the same orientation direction on the substrate because they were deformed by one and the same ion beam. From SEM pictures the orientation of the elliptical particles can be extracted. It appears that the major axis of the elliptical particles is directed parallel to the edge of substrate. In the following experiments, we can deduce the orientation of our optical beams relative to the elliptical particles by the sample edge.

6.3 Acoustic vibrations of deformed particles

The deformed T60 sample was examined with the help of the ultrafast ASOPS pump-probe setup, which is described in detail in Ch. 3. In the experiments,

the probe beam was at 820 nm and directed perpendicular to the substrate. The pump has a fluence of 0.02 mJ/cm^2 at 780 nm, and an incident angle of 45° to the substrate. The polarizations of the pump and probe beams are parallel to each other to obtain maximum signal, as sketched in the right panel of Fig. 6.2. The sample is mounted on a holder and can be rotated with the axis parallel to the normal of the sample slab and the probe beam. Therefore, the transient reflectivity can be measured for various orientations of the particles. At each orientation angle, we move the sample to search for a good point that shows clear vibrations. We note that only at thick sample points with densely packed particles, vibrations are detected. For measurements on dilute parts of the sample having isolated particles, far from each other, we never measured any vibrational signal following the electronic response.

Fig. 6.2 shows the measured results of transient reflectivity of deformed T60 sample vs. orientation angle starting from 0° increasing in steps of 45°. We observe clear oscillations at orientation angles of 45°, 135°, and 225°, while no oscillation appears at angle of 0° and 90°. At an angle of 45°, we observe a fast oscillation of 26-ps period at short time scale followed by a slow oscillation of 108-ps period. Similarly, at angle 225°, 18-ps period fast oscillation and 150-ps period slow oscillation are measured.

6.4 Discussion

At 45° and 225° we managed to observe one fast and one slower oscillation in one trace. We note for the orientation angle 225° that the fastest fast oscillation (18-ps period) coincides with the slowest slow oscillation (150-ps period). For 45°, the slowest fast oscillation (26-ps period) shows up in the trace with the faster slow oscillation (108-ps period). Analogous to the analysis of the results on spherical particles, we identify the fast oscillations as the thickness vibrations of the gold shell, and the slow vibrations as the acoustic vibrations of the entire particle. The latter vibrations involve movements along the major and minor axis, respectively. Since our experiment is sensitive to the variation of the outer surface of the gold shell, the particle can be concluded to consist of a gold-shell with a thick polar layer and a thin equator layer, as indicated in Fig. 6.3 (a). The observed fast oscillations of 18-ps 26-ps period, correspond to thickness vibrations of 29-nm and 42-nm thick gold layers, respectively.

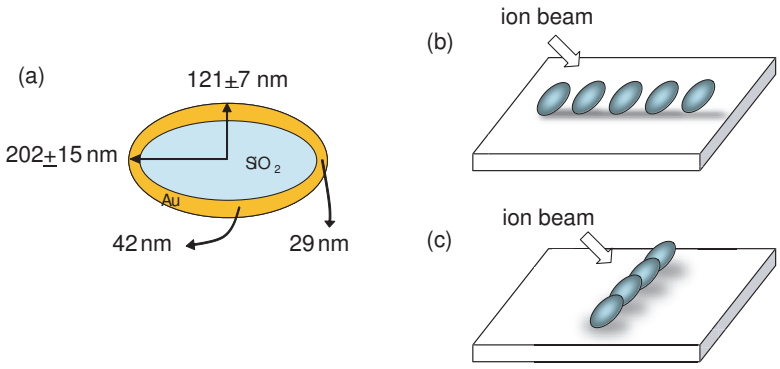

Figure 6.3: (a) Sketch of an elliptical gold-shell particle. (b) Sketch of particles with "line" ordering. (c) Sketch of particles with "row" ordering.

The periods of the slow vibrations could not be calculated using Lamb theory, since no analytical treatment is known for vibrational modes in ellipsoids. Here we approximate the vibrational modes as standing one-dimensional acoustic waves with free boundary conditions at the surface of the gold shell, and take a good connection between the gold shell and silica core. The fundamental modes are the longitudinal vibrations of the major and minor axis of the particle. By taking into account the thickness of gold calculated from the fast oscillations (29 nm at equator and 42 nm at polar), the major and minor radii of the gold shell can be computed from the measured vibrational period knowing the longitudinal sound velocity of gold ($v_{l,Au}$ = 3240 m/s) and silica ($v_{l,silica}$ = 5970 m/s). The observed average period of 105±4 ps, corresponds to R_{2min} = 121±7 nm, and that of 152±7 ps, R_{2max} = 202±15 nm. From the aspect ratio (∼1.7) of the particles, R_{2min} and R_{2max} can be calculated to be 216±9 nm and 127±8 nm, which nicely coincides with our results of the vibrational measurements.

A mysterious observation is the angular dependence of the observed traces of Fig. 6.2. We note that the traces are not taken at one and the same sample point. We always had to search for good points on the sample that show clear vibrational signals. However, clear oscillations never showed up at 0°, 90°, and 180°. It is very difficult to interpret the angular dependence because at least three factors are affected in these experiments: (i) the incident angle and polarization of the pump, (ii) the polarization of probe, and (iii) the local arrangement of particles. We recall that the pump beam excites hot

electrons in the particle and rapidly heats up the lattice, exciting acoustic vibrations. For elliptical particles, the shape may generate a dependence on the orientation of the pump beam with the particles axes. For the probe beam, experiments show that the polarization of the probe influences the sensitivity of detection at certain orientations of anisotropic nanoparticles [16]. For a polarization parallel to the long axis, one is sensitive to vibrations of the long axis, while a polarization parallel to the short axis give sensitivity in detecting vibration of the short axis. In our experiment, the probe beam is directed perpendicular to the substrate while the pump has an incident angle of 45° to the substrate. Both of them are polarized parallel to the substrate. The particles are standing with their principal axes at 45° to the substrate surface. Inspecting the symmetry of the beams relative to the particle axes, we conclude that for the pump and probe orientation angles of 135° and 225° have the same symmetry with respect to a particle for both detection and generation. However, the vibrational signals we managed to find at those angles do have clearly different periods: one has 101 ps and the other of 151 ps (see Fig. 6.2). This observation proves that the third factor of the system, namely the ordering of elliptical particles, must play a role.

In the previous chapter, we concluded that the ordering of particles influences the excitation of vibrational modes of spherical particles. For elliptical particles, we argue that two new types of fundamental ordering should exist in clusters of particles. First, the elliptical particles are standing in a line one after the other (Fig. 6.3(b)). In such a cluster vibrations along the short axis are preferentially excited and detected when the polarizations of pump and probe are along the line. Second, the elliptical particles are standing side by side in a row, and perhaps touching because of the deformation by ion beam (Fig. 6.3(c)). Here, the signal vibrations along the long axis are preferentially excited and detected, when the polarizations of pump and probe are along the row. From the SEM picture of a thick sample point in Fig. 6.1(d), we can see that the particle order varies strongly from point to point. We suspect that in the process to find the vibrational signal, we have selected at 135° a cluster in which particles are predominantly ordered in a line, and at 225° a cluster in which particles are predominantly ordered in a row. The observed two vibrational periods of 101 ps and 151 ps at angles of 135° and 225°, coincide with longitudinal vibrational periods of the short and long axis of our elliptical particle.

In Table 6.1, we summarize the measured acoustic vibrational periods of

Vibration Modes	Deformed T60 R_{2min}=127±14 nm R_{2max}=216±23 nm 	Experiment	
		Period of oscillation	Size of particle
Silica shell thickness (longitudinal)		26 ps, 18 ps	Polar: 42nm Equator: 29nm
Long axes longitudinal mode		152 ps	121±7 nm
Short axes longitudinal mode		101 ps, 108 ps	202±15 nm

Table 6.1: Summary of measured results on deformed T60 particles.

the deformed T60 sample.

6.5 Conclusion

We have demonstrated acoustic vibrations in elliptical gold-shell particles, deformed by an ion beam. In pump-probe experiments, observed periods of transient reflectivity signals include longitudinal vibrations along the long and short axis of the particle. Fast oscillation periods reveal that the thickness of the gold shell is small at the equator and thick at the pole.

Bibliography

[1] M. Born, E. Wolf, *Principles of Optics*, 6th ed. Pergamon Press, Oxford, (1980)

[2] F. Forstmann, R. R. Gerhardts,*Metal Optics Near the Plasma Frequency*, Springer-Verlag, (1986)

[3] D. Pines, *Elementary Excitations in Solids*, (Benjamin, New York 1964)

[4] A. R. Melnyk, M. J. Harrison, Phys. Rev. Lett. **21**, 85 (1968)

[5] I. Lindau, P. O. Nilsson, Phys. Lett. **31**, 352 (1970)

[6] E. Yablonovitch, et al, Phys. Rev. Lett. **58** 2059 (1987)

[7] E. Yablonovitch, T. J. Gmitter, K. M. Leung, Phys. Rev. Lett. **67** 2295 (1991)

[8] A. Imhof, W. L. Vos, R. Spric, and A. Lagendijk, Phys. Rev. Lett. **83**, 2942 (1999)

[9] P. Vukusic, J. R. Sambles, C. R. Lawrence, and R. J. Wootton, Proc. R. Lond. B **266**, 1403 (1999)

[10] S. Kinoshita, S. Yoshioka, and K. Kawagoe, Proc. R. Lond. B **269**, 1417 (2002)

[11] Y. A. Vlasov, et al., Nature, **414** 289 (2001)

[12] T. W. Ebbesen, H. J. Lezec, H. F. Ghaemi, T. Thio, and P. A. Wolff, Nature (London), **391**, 667 (1998)

[13] L. Martín-Moreno, F. J. Garcia-Vidal, H. J. Lezec, A. Degiron, and T. W. Ebbesen, Phys. Rev. Lett. **90**, 167401 (2003)

[14] A. Christ, S. G. Tikhodeev, N. A. Gippius, J. Kuhl, and H. Giessen, Phys. Rev. Lett. **91**, 183901 (2003)

[15] M. van Dijk, *Nonlinear-Optical Studies of Single Gold Nano-particles*, PHD thesis,University Leiden, (2007)

[16] M. Perner, S. Gresillon, Phys. Rev. Lett.**85**, 792(2000)

[17] C. Graf, A. van Blaaderen, Langmuir, **19**,6693 (2003)

[18] E. Prodan, C. Radloff, N. J. Halas, and P. Nordlander, Science **302**, 419 (2003)

[19] J. J. Jackson, *Classical Electrodynamics*, 3^{rd} edition, (1998)

[20] *Optical properties of metals*, vol.2 (Fachinformationszentrum Energie, 1981)

[21] J. Hohlfeld, J. G. Muller, S. S. Wellershoof, E. Matthias, Appl. Phys. B. **64** 386 (1997)

[22] J. Hohlfeld, U. Conrad, J. G. Muller, S. S. Wellershoof, E. Matthias, in:*Nonlinear Optics in Metals*, K. H. Bennemann (Ed.), Clarendon Press, Oxford, (1998)

[23] R. W. Schoenlein, W. Z. Lin, J. G. Fujimoto, and G. L. Eesley, Phys. Rev. Lett. **58**(16), 1680 (1987)

[24] C. Voisin, N. Del Fatti, D. Christofilos, and F. Vallee, J. Phys. Chem. B **105**(12), 2264 (2001)

[25] S. I. Anisimov, B. L. Kapelovich, T. L. Perelman, Sov. Phys. JETP **39**, 375 (1974)

[26] J. H. Hodak, A. Henglein, and G. V. Hartland, J. Phys. Chem. B, **104**, 9954 (2000)

[27] J. Hohlfeld et al. Chem. Phys. **251**, 237 (2000)

[28] E. Doval, A. Boukenter, and B. Champagnon, Phys. Rev. Lett. **56**, 2052 (1986)

[29] M. Fujii, Y. Kanzawa, S. Hayashi, and K. Yamamoto, Phys. Rev. B **54**, R8373 (1996)

[30] H. Portales, L. Saviot, Phys. Rev. B, **65**, 165422 (2002)

[31] J. H. Hodak, A. Henglein, and G. V. Hartland, J. Chem. Phys. **111**, 8613 (1999)

[32] J. H. Hodak, A. Henglein, and G. V. Hartland, Chem. Phys. **6**, 5263 (2004)

[33] Y. Hamanaka, J. Kuwabata, I. Tanahashi, S. Omi, and A. Nakamura, Phys. Rev. B. **63**, 104302 (2004)

[34] G. V. Hartland, J. Chem. Phys. **106**, 8048 (2002)

[35] M. A. van Dijk, M. Lippitz, and M. Orrit, Phys. Rev. Lett. **95**, 267406 (2005)

[36] D. Mazurenko, *Ultrafast Optical Switching in Three-Dimensional Photonic Crystals*, PHD thesis, University Utrecht, (2004).

[37] D. A. Mazurenko, X. Shan, Phys. Rev. B, **75**, 161102(R) (2007)

[38] R. Taubert, F. Hudert, A. Bartels, F. Merkt, A. Habenicht, P. Leiderer and T. Dekorsy, New J. Phys. **9**, 376 (2007)

[39] G. V. Hartland, Annu. Rev. Phys. Chem. **57** 403 (2006)

[40] A. Arbouet, N. Del Fatti and F. Valle, J. Chem. Phys. **124**, 144701 (2006)

[41] W. Huang, W. Qian and M. A. El-Sayed Nano Lett. **4**, 1741 (2004)

[42] W. Huang, W. Qian and M. A. El-Sayed J. Phys. Chem. B **109**, 18881 (2005)

[43] L. Bonacina, A. Callegari, C. Bonati, F. van Mourik and M. Chergui Nano Lett. 6 7 (2006)

[44] A. Plech, R. Cerna, V. Kotaidis, F. Hudert, A. Bartels and T. Dekorsy, Nano Lett. **7** 1026 (2007)

[45] H. Petrova et al, J. Chem. Phys. **126** 094709 (2007)

[46] R. W. Wood, Philos. Mag. **4** 296 (1902)

[47] A. Hessel and A. A. Oliner, Appl. Opt. **4**, 1275 (1965)

[48] L. Rayleigh, Proc. Roy. Soc. London) **A79**,399 (1907)

[49] U. Fano, Phys. Rev. **50**, 573 (1936)

[50] U. Fano, J. Opt. Soc. Am. **31**, 213 (1941)

[51] G. Mie, Ann. Phys. **25**, 377 (1908)

[52] A. Liebsch, Phys. Rev. B **36**, 7378 (1987)

[53] U. Kreibig and M. Vollmer, *Optical properties of metall clusters*, Springer-Verlag, Berlin, (1995)

[54] J. Penninkhof, *Tunable plasmon resonances in anisotropic metal nanostractures*, PHD thesis, University Utrecht, (2007).

[55] C. Graf, A. van Blaaderen, Langmuir, **18**,524 (2002)

[56] A. L. Aden and M. Kerker, J. Appl. Phys. **22**, 1242 (1951)

[57] A. Moroz, Phys. Rev. Lett.**83**, 5274 (1999)

[58] A. Moroz, Phys. Rev. B,**51**, 2068 (1995)

[59] A. Moroz, Phys. Rev. B,**66**, 115109 (2002)

[60] N. Stefanou, V. Yannopapas, and A.'Modinos, Comp. Phy. Commun. **113**, 49 (1998)

[61] H. R. Philipp and H. Ehrenreich, Phys. Rev. **129**, 1550 (1963)

[62] A. Bartels, F. Hudert, T. Dekorsy, Appl. Phys. Lett. **88**, 041117 (2006)

[63] Niles, Bechelor report (2007)

[64] *User's Manual of Model SR844 RF Lock-In Amplifier* Stanford Research Systems, (2003)

[65] S. D. Poisson, Mem. de le Acad. (Paris) **8**, 357 (1829)

[66] P. Jaerish, Creele J. Math. **88**, 131 (1880)

[67] H. Lamb, Proc. Lond. Math. Soc. **14**,50(1882)

[68] X. Shan, X. Zhang, D. A. Mazurenko, A. van Blaaderen, J. I. Dijkhuis, F. Hudert and T. Dekorsy, J. Phys.: Conf. Ser. **92**, 012035 (2007)

[69] M. Perner, P. Bost, U. Lemmer, G. von Plessen, J. Feldmann, U. Becker, M. Mennig, M. Schnitt, and H. Schmidt, Phys. Rev. Lett. **78**, 2192 (1997)

[70] W. S. Fann, R. Storz, H. W. K. Tom, and J. Bockor, Phys. Rev. B **46**, 13592 (1992)

[71] W. S. Fann, R. Storz, H. W. K. Tom, and J. Bockor, Phys. Rev. Lett. **68**, 2834 (1992)

[72] C. Kittel, *Introduction To Solid State Physics*, 6^{th} edition, (1986)

[73] T. Juhasz, H. E. ElsayedAli, G. O. Smith, C. Suarez, and W. E. Bron, Phys. Rev. B **48**, 15488 (1993)

[74] R. H. M. Groeneveld, R. Sprik, and A. Lagendijk, Phys. Rev. B **51**, 11433 (1995)

[75] A. Arbouet, C. Voisin, and et, Phys. Rev. Lett. **90** 177401 (2003)

[76] A. E. Neeves and M. H. Birnboim, Opt. Lett. **13**, 1087 (1988)

[77] N. Kalyaniwalla, J. W. Haus, R. Inguva, and M. H. Birnboim, Phys. Rev. A **42**, 5613 (1990)

[78] J. W. Haus, H. S. Zhou, S. Takami, M. Hirasawa, I. Honma, and H. Komiyama, J. Appl. Phys. **73**, 1043 (1993)

[79] R. D. Averitt, S. L. Westcott, and N. J. Halas, Phys. Rev. B. **58**,10203 (1998)

[80] R. D. Averitt, D. Sarkar, and N. J. Halas, Phys. Rev. Lett. **78**,4271 (1997)

[81] A. Devizis, V. Vaicikauskas, and V. Gulbinas, Appl. Opt. **45**, 2535 (2006)

[82] Y. Ping, D. Hanson, I. Koslow, T. Ogitsu, D. Prendergast, E. Schwegler, G. Collins, and A. Ng, Phys. Rev. Lett. **96**, 255003 (2006)

[83] H. Inouye, K. Tanaka, I. Tanahashi, and K. Hirao, Phys. Rev. B. **57**, 11334 (1998)

[84] L. D. Landau and E. M. Lifshitz, *Electrodynamics of continuous media*, vol. 8, of *Course of Theoretical Physics* (Pergamon, Oxford, 1975)

[85] C. Cadloff and N. J. Halas, Appl. Phys. Lett. **79**, 674 (2001)

[86] C. Guillon, P. Langot, N. Del Fatti and F. Vallee, Nano Lett. **7**(1), 138 (2006)

[87] A. E. H. Love, *A treatise on the mathematical theory of the elasticity,* (New York: Dover, 1944)

[88] A. C. Eringen and E. S. Suhubi, *Elastodynamics*, vol. 2, (Academic press, New York, 1975)

[89] N. D. Fatti, C. Voisin, D. Christofilos, F. Vallee, and C. Flystzanis, J. Phys. Chem. A, **105**, 4321 (2000)

[90] G. Genty, *Supercontinuum generation in microstructured fibers and novel optical measurement techniques*, PHD thesis, Helsinki University of Technology, (2004).

[91] K. M. Hilligsøe, *Wave Propagation in Photonic Crystal Fibers*, PHD thesis, University of Aarhus and NKT Academy, (2003)

[92] J. J. Penninkhof, C. Graf, T. van Dillen, A.M. Vredenberg, A. van Blaaderen, A. Polman, Adv. Mater, **17** 1484 (2005)

[93] J. J. Penninkhof, T. van Dillen, S. Roorda, C. Graf, A. van Blaaderen, A.M. Vredenberg, A. Polman, Nucl. Instr. and Meth. in Phys. Res. B, **242** 523 (2006)

[94] H. Trinkaus and A. I. Ryazanov, Phys. Rev. Lett. **74**, 5072 (1995)

[95] T. van Dillen, M. J. A. de Dood, J. J. Penninkhof, A. Polman, S. Roorda, and A.M. Vredenberg, Appl. Phys. Lett. **81**, 3591 (2004)

[96] T. van Dillen, A. Polman, P. R. Onck, and E. van der Giessen, Phys. Rev. B, **71**, 024103 (2005)

[97] G. A. Antonelli, H. J. Maris, S. G. Malhota and J. M. E. Harper, J. Appl. Phys. **91** 3261 (2002)

[98] S. L. Westcott, J. B. Jackson, C. Radloff and N. J. Halas, Phys. Rev. B **66**, 155431 (2002)

[99] L. D. Landau, *Theory of elasticity* (Pergamon Press) (1970)

Summary

Optical properties of metallic nano-structures have attracted a lot of attention in the past decades. The presence of free electrons in metal nanostructures creates surface plasmons, and gives rise to changes in linear and nonlinear optical properties from bulk materials. One of the ambitions of nano-science is to exploit these differences to tailor the properties of nanostructures through their size, shape, and organization. In this thesis, we focus on nano-sized silica-core gold-shell particles, study the linear optical properties, the ultrafast non-linear responses, and acoustic vibrations excited by optical excitation.

In chapter 2, we start the research of gold-shell particles by analyzing the linear optical properties in the visible range, both in ordered and disordered arrays, and both in reflection and transmission. The observed linear reflection spectra show a very complex multi-peak structure, which can be favorably compared with calculations and identified as surface plasmons and delocalized excitations. Highly directional diffraction patterns, with hexagonal or cubic symmetry, were observed in the photonic crystal structure, corresponding to Fraunhofer diffraction of a collection of small crystallites. The disordered samples on a transparent substrate allowed us to measure the transmission. A transmission window was observed from 500 nm to 650 nm for all samples, which is interpreted as transport of plasmons in the photonic band gap. In addition, some special points were discovered on the ordered sample, which give rise to giant reflectivity at the plasmon resonance peak.

In chapter 3, we describe two ultrafast pump-probe setups relying on femtosecond lasers at different repetition rates. One is a standard pump-probe setup with a mechanical delay line and a lock-in amplifier for data acquisition. The other is a so-called Asynchronous Optical Sampling (ASOPS) setup with high repetition rate that does not need a scanning mechanical delay line.

In chapter 4, we analyze the ultrafast response of the 3-D gold-shell photonic crystal following femtosecond optical excitation. We analyze the decay time and the shape of the response as they depend on both the probe wavelength and pump pulse intensity. The transient reflectivity strongly varies depending on the probe wavelength, which can be accounted for by a pump-induced broadening of the plasmon resonance of the gold-shell particles. The observed dynamics can be analyzed in the framework of the so-called “two-

temperature model". From the pump power dependence measurement, an electron-phonon coupling constant of 1×10^{16} W/(m^3K) is deduced, and an electron temperature up to ∼1800 K can be estimated.

Acoustic vibrations of gold-shell particles following the optically induced ultrafast electronic response are discussed in chapter 5. We introduce a two-shell model developed on basis of Lamb theory to calculate the vibrational mode frequencies. By employing pump-probe experiments, we excite the acoustic vibrations of the gold-shells and detect via modulations of the optical reflectivity. Spherical breathing modes and thickness modes of vibrations were identified in a 3-D ordered array of the particles. For a disordered array, elliptical modes were excited and observed. Finally, we demonstrate a dependence of the vibrational period on the gold-shell size and the thickness of gold-shell, and observe the echoes from the silica core.

Gold-shell particles can be deformed by ion beam irradiation, and form elliptical particles. In chapter 6, we measured the acoustic vibrations of the elliptical gold shells. The observed periods show a dependence on the orientation of particles, corresponding to the longitudinal vibrations along the long and short axis. From fast oscillations observed on the short time scale, we conclude that the thickness of the gold shell is locally changed by ion beam irradiation.

Samenvatting

Optische eigenschappen van metallische nanostructuren hebben veel aandacht getrokken in de afgelopen decennia. De aanwezigheid van vrije elektronen in metallische nanostructuren creëert oppervlakteplasmonen en zorgt voor verschillen in de lineaire en niet-lineaire optische eigenschappen ten opzichte van die van macroscopische materialen. Het is een van de ambities van de nanowetenschap om, door deze verschillen te benutten, de optische eigenschappen van nanostructuren naar wens te kunnen aanpassen door middel van hun omvang, vorm en structuur. In dit proefschrift concentreren we ons op nanodeeltjes met een siliciumdioxide kern en een gouden schil. Van deze deeltjes bestuderen we de lineaire optische eigenschappen, de ultrasnelle niet-lineaire responsies en de door optische excitatie opgewekte akoestische vibraties.

In hoofdstuk 2 beginnen we het onderzoek naar gouden-schildeeltjes door de lineaire optische eigenschappen in het zichtbare gebied te analyseren, zowel voor geordende als voor ongeordende deeltjesconfiguraties en zowel in reflectie als in transmissie. De waargenomen lineaire reflectiespectra laten een zeer complexe structuur met veel pieken en dalen zien, waarvan sommige, door vergelijking met berekeningen, kunnen worden geïdentificeerd als effecten van oppervlakteplasmonen en andere als effecten van gedelokaliseerde excitaties. Bij de reflectie aan het fotonische kristal, de geordende structuur van nanodeeltjes, werden in hoge mate directionele buigingspatronen met zeshoekige of kubische symmetrie waargenomen. Deze patronen corresponderen met de Fraunhofer-diffractie aan een verzameling van kleine kristallieten. Bij de ongeordende proefmonsters op een transparant substraat was het mogelijk om de transmissie te meten. Bij alle proefmonsters werd een transmissievenster van 500 tot 650 nm waargenomen, wat kan worden toegeschreven aan transport van plasmonen. Bovendien werden op het geordende proefmonster enkele speciale punten ontdekt waar er een gigantische reflectie optreedt is op de plasmonresonantie.

In hoofdstuk 3 beschrijven we twee ultrasnelle pomp-probe-opstellingen, die gebaseerd zijn op femtosecondelasers met een verschillende repetitiefrequentie. Een is een standaard pomp-probe-opstelling met een mechanische vertragingslijn en een lock-in-versterker voor dataverwerving. De andere is een opstelling voor zogenaamde “Asynchronous Optical Sampling” (ASOPS) of “asynchrone optische bemonstering”. Deze opstelling heeft een repeti-

tiefrequentie van 1 GHz, terwijl er geen bewegende mechanische vertragingslijn nodig is.

In hoofdstuk 4 analyseren we de ultrasnelle responsie van een driedimensionaal fotonisch kristal, bestaande uit gouden-schildeeltjes, na een 100 fs durende optische excitatie. We analyseren hoe de vervaltijd en de vorm van de responsie afhangen van de golflengte van de probepuls en de intensiteit van de pomppuls. De tijdsafhankelijke reflectiegraad varieert sterk met de golflengte van de probe, wat kan worden verklaard door een pompgeïnduceerde verbreding van de plasmonresonantie van de gouden-schildeeltjes. De waargenomen dynamica kan worden geanalyseerd binnen het raamwerk van het zogenaamde "twee-temperaturenmodel". Uit de meting van de afhankelijkheid van het pompvermogen kan een elektron-fonon-koppelingsconstante worden afgeleid van 1×10^{16} W/(m^3K) en de elektronentemperatuur kan worden geschat op oplopend tot 1800 K.

Akoestische vibraties van gouden-schildeeltjes, volgende op de optisch opgewekte ultrasnelle elektronische responsie, worden beschreven in hoofdstuk 5. We introduceren een twee-schillenmodel, dat is ontwikkeld op grond van de Lambtheorie, en met dat model rekenen we de frequenties van de vibratiemodes uit. In pomp-probe-experimenten wekken we akoestische vibraties van de gouden schillen op, die we detecteren via modulaties in de optische reflectie. Bolvormige zogenaamde "ademhalingsmodes" en "diktemodes" van de vibraties werden geïdentificeerd in de driedimensionale geordende structuur van gouden-schildeeltjes. Bij een ongeordende structuur werden elliptische vibratiemodes opgewekt en waargenomen. Tenslotte tonen we aan dat de periode van de vibraties afhankelijk is van de omvang en de dikte van de gouden schil en we observeren de echo's van de siliciumdioxide kern.

Gouden-schildeeltjes kunnen worden vervormd tot ellipsoïde deeltjes door middel van bestraling met ionenbundels. In hoofdstuk 6 meten we de akoestische vibraties van de ellipsoïde gouden schillen. De waargenomen periodes blijken afhankelijk te zijn van de oriëntatie van de deeltjes en corresponderen met longitudinale vibraties langs de lange en de korte as. Uit snelle oscillaties die op korte tijdsschaal werden waargenomen trekken we de conclusie dat door de bestraling met de ionenbundels de dikte van de gouden schil lokaal wordt veranderd.

List of Publications and Conference Visits

This thesis is partly based on the following publications:

1. D. A. Mazurenko, X. Shan, J. C. P. Stiefelhagen, C. M. Graf, A. van Blaaderen, and J. I. Dijkhuis, *Coherent vibrations of submicron spherical gold shell*, Phys. Rev. B **75**, 161102(R) (2007)

2. X. Shan, X. Zhang, D. A. Mazurenko, A. van Blaaderen, J. I. Dijkhuis, F. Hudert and T. Dekorsy, *Acoustic Vibrations in Nanosized Gold-Shell Particles*, J. Phys.: Conf. Ser. **92**, 012035 (2007)

Parts of the research described in this thesis have been presented in the following international conferences:

1. *Son et Lumière: from microphotonics to nanophononics*, 16th-28th October, 2006, Cargèse, France.

2. *Phonons 2007* 12th Int. Conf. on Phonon Scattering in Condensed Matter, 15th-20th July, 2007, Paris, France.

Further, parts of this work have been presented on local events: annual meetings of the FOM "Wetenschappelijke vergadering voor de Gecondenseerde Materie", Veldhoven (2004-2007); the *Do!-days*, Noordwijkerhout, 23rd March (2007); Photon workshop, University of Twente (2005); and at the Tsinghua University February (2006 and 2007), China.

Acknowledgments

I am grateful to all the people who have helped me in the past four years during my Ph.D research in Utrecht. As a student to go abroad for the first time, to live in a different culture, and to do a difficult research, I could not imagine finishing such a job without the help of many people.

The first, most sincerely thanks I would like to address to my supervisor, Prof. Dr. Jaap Dijkhuis. He introduced me into area of condensed matter and ultrafast dynamics and advised me in the past four years. He gave me support and confidence in final success of the project even in desperate situations. His challenging ideas and questions make the research adventurous. One important ability of Jaap I realized in overviewing the whole work, is to judge in research, what is possible and what is impossible. He made me just in time stop a walk on the wrong road. In addition, his social ability in academic communication allowed me to obtain help from many other groups in the University, and even in Europe. Further, I am greatly indebted to Jaap for the hard job of checking language problems in this thesis. I know how difficult it is to correcting grammar and spelling and thinking about physics at the same time. Jaap impressed me by the word: be not only good in physics, but also good in English. Thank you very much!

I have to give my acknowledgements to the technical support from Cees de Kok, Paul Jurrius, and Frans Wollenberg. My studies would not have been successful without their fantastic work of handling the equipments. And I would like to thank our secretary, Clarien Derks, who helped me to deal with those headachy documents needed for my stay in Holland.

I am greatly indebted to Dmitry Mazurenko, who supervised me at beginning of this project. Although it took me months to understand his speech, I learned the most important ideas and experimental skills from him. Many research in this thesis are following Dima's analysis. It makes the 'Dima' to become an often-heard name in our group even after the four years since he left. And I must also acknowledge my debt to Otto Muskens, who amazed me by two things, he transported me to Michiel's promotion party by bicycle in an awfully rainy winter evening, and it only took him an hour to calculate the dielectric constant of gold for different temperatures that I used in Ch. 4. I also acknowledge Xi Zhang, who calculated the vibrational modes for the "two-shell" model during his short period in Utrecht.

It is my pleasure to thank Johan Penninkhof and Cristina Graf who fabricated the samples for my research. I know how difficult it is to fabricate gold-shell samples and to deform them by the ion beam of the Van der Graaff-accelerator in Utrecht. I would like to thank Prof. Dr. Alfons van Blaaderen for the long-term collaboration and careful reading of manuscripts. I also thank Prof. Dr. Albert Polman for his interest in the experiments on ellipsoidal particles. Further, I would like to thank Dr. A. Moroz who made the KKR calculations of the linear spectrum that I presented in Ch. 2. I also acknowledge Prof. Dr. Andries Meijerink for loaning the CCD, that allowed me to measure linear spectra with high sensitivity, Prof. Dr. J. Kelly and Prof. Dr. R. Schropp, for carefully reading my manuscripts.

I must address my special thank to Prof. Dr. T. Dekorsy of the University of Konstanz in Germany, for offering the fantastic setup ASOPS. And thanks to F. Hudert for offering a guest room and, most importantly, skillful helps on the ASOPS experiments. So many important data I measured in Konstanz, that make the work more complete and have been presented in Ch. 5 and Ch. 6. A lot of thanks to the people who helped me to deal with photonic-crystal fibers for white light generation, Vincent Boer and Jonathan Palero from the group of Soft Condensed Matter and Biophysics, and Dmitry Turchinovich and Matthias Hoffmann in the University of Freiburg. I would thank to Carlos van Kats for making SEM pictures of the sample. Special thanks I would like to address to Marijn Versteegh, who made the beautiful translation of "Samenvatting" in Dutch.

I would like to thank the students who give contributions to this thesis. Johan Stiefelhagen did his "klein onderzoek" about acoustic vibrations, Niels Keizer developed the computer system for controlling the lock-in amplifier, Cornelis Huizinga made the FT calculation to understand the scattering patterns of Ch. 2.

I enjoyed all the time shared with my colleagues, Dima, Otto, Peter, Marijn, Dmitry, Lennart, Jhonny, Louise, Johan, Inge, Erik, Richard. I have had quite interesting discussions with Dmitry Turchinovich, who is always active to generate 'brilliant' ideas. I thank Peter and Lennart for nice discussions and the help with software.

In addition to this, there so many friends that I have met in Utrecht. I like to give my best regards to Yanchao, Hongbo, Djali, Jun, Duo, Ning, and Margri, and special regards to Tanja and Yi who has disclosed Utrecht for me during my first weeks in the Netherlands. Special thanks to Xin and Tanja

for taking care of me when I was sick. Some of them still stay in Utrecht and some have already left, now I am leaving, but we are still friends.

Thanks to Prof. Shiqun Li and Prof. Nianle Wu, my former supervisors during my master research, who had nice discussions with me and let me present my Ph.D works in Tsinghua University.

Thanks to Xuegang, for your support all along the four years.

Finally, I would like to again acknowledge all my colleagues and friends. There are many 4 years in the life of a human being, but I will remember my 4 years in Utrecht.

Curriculum Vitae

The author of this thesis was born on 14 May 1979 in Taian, Shandong, China. She finished her bachelor education in the Department of Physics Tsinghua University in 2000. In the same year, she started her graduat research in the direction of solid-state laser techniques in the "Optics Group" of the Department of Physics in Tsinghua, supervised by Prof. S. Li and Prof. N. Wu. After graduating for her master degree in 2003, she decided to further study optical materials of condensate matter and to go abroad. In January 2004, she went to the Netherlands, started her Ph. D research in the group of "Atom Optics and Ultrafast Dynamics" led by Prof. Dr. J. I. Dijkhuis in the Debye Institute for Nanomaterials of the University of Utrecht. This thesis represents the author's accomplishments during the four-years' research period in Utrecht.